UNIVERSITY OF SOUTHAMPTON

Faculty of Engineering, Science and Mathematics

School of Engineering Sciences

Stress and Damage Assessment in Woven Composite Materials by means of Thermoelastic Stress Analysis

by

Richard Konrad Frühmann

Thesis for the degree of Doctor of Philosophy

September 2009

UNIVERSITY OF SOUTHAMPTON

ABSTRACT

Faculty of Engineering, Science and Mathematics
School of Engineering Sciences

Doctor of Philosophy

Stress and Damage Assessment in Woven Composite Materials by means of Thermoelastic Stress Analysis

by Richard Konrad Frühmann

The work described in this thesis considers the application of thermoelastic stress analysis (TSA) to assess stresses and damage in woven composite materials. Woven composite materials offer high specific strength and stiffness, while being well suited to low cost manufacturing techniques. This makes them a cost effective material for weight critical structural applications. The weave, however, introduces stress concentrations at the meso-scale which are critical to damage initiation. Experimental techniques are therefore required to assess the severity of stress concentrations and damage.

TSA is an infrared (IR) technique which uses the thermoelastic effect to obtain measurements related to the stresses within a material. The non-contacting nature of TSA make it ideal for studying components with non-uniform stress fields. In this work, a new IR detector system for TSA is introduced which provides radiometric calibration, high frame rates and a motion compensation routine, essential for studying the thermoelastic response at small scales. This has enabled TSA to be conducted at the scale of the individual yarns in woven composites.

A simple model has been used to predict the thermoelastic response from individual yarns. This has revealed that careful determination of the material properties is critical for accurate predictions, and that the use of literature values, as has been done in the past, can lead to misleading results. Thus it is shown that the response from a woven composite originates from the yarns, rather than a surface resin layer, and that the non-uniform strain field manifests itself strongly in the TSA data.

The work then investigates the development of fatigue damage in woven composites. This has shown that damage can initiate at stress levels as low as 10% of the ultimate failure stress in single ply composites. Using the high resolution optics and motion compensation it has been possible to follow the development of matrix cracks in individual yarns. A signature pattern in the TSA data is defined that enables the matrix cracks to be clearly identified.

For TSA to be applied as a tool for non-destructive testing of in-service structures, it is essential that simple procedures are developed and that the equipment is portable. To facilitate the more widespread uptake of TSA, the feasibility of using a simplified means of introducing a load into a component was investigated. It was demonstrated that a single transient excitation can be used to obtain a TSA measurement.

The work described in this thesis thereby demonstrates that TSA can be applied to study stresses and damage in inhomogenous materials. The feasibility of using a simplified loading methodology is proven. The study thereby represents a significant step towards an improved understanding of TSA and increasing its application range.

Contents

List of Figures

List of Tables

Declaration of Authorship

I, *Richard Konrad Frühmann*, declare that the thesis entitled:

Stress and Damage Assessment in Woven Composite Materials by means of Thermoelastic Stress Analysis

and the work presented in the thesis are both my own, and have been generated by me as the result of my own original research. I confirm that:

this work was done wholly or mainly while in candidature for a research degree at this University;

where any part of this thesis has been submitted for a degree or any other qualification at this University or any other institution, this has been clearly stated;

where I have consulted the published work of others, this is always clearly attributed;

where I have quoted from the work of others, the source is always given. With the exception of such quotations, this thesis is entierly my own work;

I have acknowledged all main sources of help;

where the thesis is based on work done by myself jointly with others, I have made clear exactly what was done by others and what I contributed myself;

parts of this work have been published (Appendix A).

Signed:.....

Date:.....

Acknowledgements

First and foremost I would like to recognise the support and guidance of my supervisors, Prof. Janice Dulieu-Barton and Dr. Simon Quinn. Not only have their experience and input been invaluable, but their unfaltering dedication to the project and their passion for research have at all times been a real inspiration.

No experimental project would be complete without a dedicated technician, and a special thanks therefore goes to Erik Roszkowiak for his friendly advice and technical assistance. I would also like to acknowledge Dave Beckett, Robert Barnes and Chris Williams for contributing with their practical know-how.

I would like to thank my colleague Shamala who has been a great sounding board for ideas and shared experiences over the course of the past three years.

Finally I would like to thank my parents for their patience, advice, and for providing a sense of security through the toils and troubles of life in general.

To all involved, a big thankyou!

$\ddot{\smile}$

Richard

Notation

Symbol	Meaning	Units
Upper case Roman symbols		
A	thermoelastic parameter	GPa K^{-1}
B	thermoelastic parameter	GPa K^{-1}
C_p	specific heat capacity	J kg^{-1} K^{-1}
E	Young's modulus	GPa
F_0	Fourier number	-
I	second moment of area	mm^4
P	applied force	N
Q	reduced material stiffness	GPa
S	standard deviation	%
T	absolute temperature of a source	K
V	volume fraction	-
Lower case Roman symbols		
c	speed of light	m s^{-1}
d	distance from point measurement to end tab in a tensile specimen	mm
h	Planck's constant	J s
k	conductivity	W m^{-1} K^{-1}
l	length of a cantilever beam	mm
l_t	overall length of a tensile specimen	mm
l_g	gauge length of a tensile specimen	mm
r	radiant emittance	W m^{-3}
s	variability	%
t	time	s
w	width of a tensile specimen	mm
x	distance from the fixed end of a cantilever beam	mm
z_t	total thickness of tensile specimen	mm
z_0	half thickness of a cantilever beam	mm
δz	deflection of a cantilever beam	mm

Symbol	Meaning	Units
Greek symbols		
α	coefficient of thermal expansion	$\times 10^{-6}\mathrm{K}^{-1}$
βmax	maximum out of plane yarn orientation	$^{\circ}$
γ	shear strain	-
Δ	change in	-
ε	direct strain	-
ϵ	emissivity	-
θ	angle between global and material coordinate systems	rad
κ	Boltzmann's constant	J K^{-1}
λ	wavelength	m
ν	Poisson's ratio	-
ρ	density	kg m^{-3}
σ	stress	MPa
Subscripts		
$_{1,\ 2}$	principal material axes	-
$_{L,\ T}$	global coordinate system	-
$_{bb}$	property of a black body	-
$_{r}$	property of the resin	-
$_{f}$	property of the fibre	-
$_{x,\ y}$	principal stress directions	-

List of abreviations

Abreviation	Full version
CLT	classical laminate theory
CSM	chopped strand matt
CTE	coefficient of thermal expansion
DIC	digital image correlation
DL	digital level
DSC	digital scanning calorimetry
FAST	focal-plane array for synchronous thermography
FEA	finite element analysis
FE	finite element
FRP	fibre reinforced polymer
InSb	indium / antimonide
IR	infrared
NASA	national aeronautics and space administration
NDE	non-destructive evaluation
NUC	non-uniformity correction
PPT	pulsed phase thermography
pre-preg	pre-impregnated fabric
RTM	resin transfer moulding
SPATE	stress pattern analysis by thermal emissions
TSA	thermoelastic stress analysis
UD	unidirectional

Chapter 1

Introduction

1.1 Background

Fibre reinforced polymer (FRP) composite materials were invented in the 1940's by the aerospace industry, motivated by the need for materials with higher specific strength and stiffness than were available at the time [1]. Scope for increased use of composite materials still exists, particularly in commercial aircraft, as identified by both Boeing [2] and Airbus [3], the two largest manufacturers of commercial aircraft. While the industry envisages performance benefits from the use of composites, the very high cost associated with current autoclave techniques is seen as the key barrier impeding the introduction of composite materials for large primary structures. Cost effective manufacturing techniques have been developed by the marine and wind turbine industry, enabling large structures to be manufactured as single parts [4, 5]. However, quality control and certification of the resulting components represent major challenges that need to be addressed in a similarly cost effective manner [6, 7].

Since their invention, FRP composites have been adopted across a range of industries including oil and gas, marine, wind energy and civil engineering where they have been used both for the manufacture of new structures and for the repair of existing structures [8, 9, 10]. In many applications, composite materials are still viewed as a new technology and the need remains for a better understanding of their behaviour when subjected to mechanical and environmental fatigue, damage evolution and damage tolerance. Furthermore, the development of suitable measurement techniques will be necessary in the certification of new and existing materials and components, and to provide quality control and defect / damage detection in finished and in-service structures. These requirements form the fundamental motivation for the current study.

The particular type of composite material considered in the current work is an FRP in which the fibre reinforcement has been woven into a textile. Woven textile composites are reputed to offer cost effective manufacturing processes while maintaining good specific mechanical properties and therefore represent a feasible option for many structural challenges in which both weight and cost are important factors [11]. The textile format of the reinforcing fibres provides ease of handling and good drapeability, allowing

the fibres to be laid into complex shaped moulds, thus lowering the labour costs [12] while well developed weaving technology from the textile industry offers high quality and good availability of the dry fibre preform. A second advantageous characteristic reported in the literature is the improved resistance to impact damage, arising from the mechanical interlocking of the fibres - a feature of great interest in many applications in which plate structures may be subject to foreign object impact during service [13]. This mechanical interlocking however also introduces complexity into the stress field within the material at the scale of the yarns. The resulting stress concentrations can be instrumental in the initiation of fatigue damage and hence the failure of a component [14]. An experimental technique is therefore required to provide a means for quantifying the severity of the stress concentrations and to identify the presence of possible defects and the development of damage.

The technique proposed is thermoelastic stress analysis (TSA) [15]. TSA is based on the thermoelastic effect which was first identified by William Thomson in 1853 [16]. When a body is subjected to an elastic change in stress, a corresponding reversible change in temperature occurs that can be directly related to the stress change. It was however not until 1967 that Belgen [17] first proposed the use of an infrared (IR) detector to provide a means of deriving stress from the thermoelastic temperature change. In a linear elastic material, the change in temperature is proportional to the change in stress [18]. The small changes in temperature that occur are measured using a focal plane array IR detector. The high surface emissivity of many plastic and composite materials means that they require no surface preparation at all [19] making TSA a true non-contacting stress analysis technique. This has the advantage that the stress field of the component under observation is not affected by the measuring technique, which is particularly significant when looking for small features in the stress field. Modern IR detector arrays with high spatial and thermal resolutions thereby allow small scale local stresses to be measured. Thus the high resolution and non-contacting nature of TSA renders it as an attractive tool for the study of woven composite materials.

1.2 Aims, objectives and novelty

The overarching aim of the work described in this thesis is to demonstrate that TSA can be applied in a quantitative manner to inhomogenous materials for the purpose of stress analysis and damage evaluation. Woven composites are studied because the heterogeneity in the thermoelastic response has a well defined geometry. This makes them an ideal basis for validating an approach for dealing with material heterogeneity in TSA. Damage identification studies are conducted that address both laboratory testing and the in-service maintenance environment. To achieve the overarching aim, three fundamental objectives are addressed as follows:

1. to understand the thermoelastic response from woven composite materials,

2. to investigate fatigue in woven composite materials,

3. to develop a modified TSA procedure that enables TSA to be applied as a non-destructive evaluation (NDE) tool outside of the laboratory.

TSA has been successfully applied to composite materials, including woven composites [20]. However, no study has considered the specific challenges associated with material heterogeneity and the corresponding heterogeneity of the thermoelastic response. The work described in this thesis uses high resolution optics to investigate the thermoelastic response at the scale of the yarn. This is made possible through the use of a motion compensation routine applied to the raw IR data. The interpretation of the data is based on a simple modelling approach [21] that considers the warp and weft yarns as unidirectional (UD) composite cells. As such it represents the first comprehensive work to investigate the challenges of applying thermoelastic stress analysis to investigate the meso-scale behaviour of woven composite materials. For TSA to be used as a tool for characterising and certifying low cost composite materials, it is paramount that the challenges associated with studying inhomgeneous materials are addressed.

The cyclic load required as a normal part of TSA testing is ideal for growing fatigue damage. In woven composite materials, small scale damage initiates as a result of the weave architecture, even at low load amplitudes [22]. Although damage in composite materials has been studied using TSA [23], the current work is the first to apply high resolution optics to identify damage at small scales. The challenge is to demonstrate that TSA can be used not only to evaluate damage at small scales, but also to provide further information about the mechanics underlying the initiation and development of fatigue in woven composite materials. For TSA to be used as a quality control or damage detection tool, it is vital that the potential of the technique for damage or defect characterisation is demonstrated.

TSA is often viewed as a laboratory based technique, due to the requirement for cyclic loading and the corresponding specialist equipment [24]. In the current work, the feasibility of applying TSA in conjunction with a single transient excitation is investigated. A simpler method of introducing a change in stress within a component will allow the technique to be applied with greater flexibility in a larger range of testing scenarios. For TSA to be applied as a tool for inspection of in-service structures it is essential that the equipment is portable, and that simple robust procedures are developed that can be applied during routine inspection.

1.3 Structure of the thesis

The thesis begins with a general overview of woven composite materials in Chapter 2, in which a definition for woven composite materials is specified. A review of relevant manufacturing processes is provided. The current knowledge pertaining to the mechanical behaviour of woven composite materials and the numerical and experimental approaches used to study them are summarised. The chapter sets out clearly why TSA should be developed as a tool for assessing woven composite materials.

Chapter 3 reviews the theory and application of TSA to composite materials and the study of damage. This shows that little work has been conducted at high resolution and that TSA studies of woven composite materials are few. Since this work introduces a new detector and TSA system, a brief history of IR measurement and its application to TSA is also provided. Together, Chapters 2 and 3 establish a background to justify the current work, and establish a basis of knowledge from which to confront the challenges outlined section 1.2.

Chapter 4 describes the TSA system used in this work. The use of the system in TSA research has not been documented in the open literature, and the system has been presented by the manufacturers largely as a 'black box'. It is the first system to incorporate radiometric calibration and full field motion compensation capability for work at high spatial resolutions. It is therefore essential that a substantial investigation into the mode of operation and reliability of the system is conducted.

Chapters 5, 6 and 7 then address each of the three objectives outlined in section 1.2 in turn. Chapter 5 begins with the definition of a simple modelling approach to form a basis for interpreting the TSA data from a woven composite material. This includes detailed material characterisation and a parametric study considering the influence of material heterogeneity on the thermoelastic response. A series of experiments is then conducted to validate the method.

Fatigue in 2 x 2 twill woven E-glass / epoxy specimens is then investigated in Chapter 6. It is shown that TSA can be used to inform on the mechanics of damage initiation and growth in these materials by using the full spectrum of information available from this data rich technique. The identifaction of a signature pattern is also presented, illustrating how TSA could be used as a simple tool for damage identification and characterisation in a routine engineering situation.

Having established the potential of TSA for damage identification, the next logical step is to investigate how TSA can be applied as an NDE technique for out-of-laboratory inspection of structures. Chapter 7 investigates the feasibility of using a single transient excitation to effect a TSA measurement, thereby establishing a basis for further development in this direction.

The main outcomes of the experimental work are then summarised in Chapter 8 and ideas for further work are presented in Chapter 9.

Chapter 2

Woven Composite Materials

2.1 Textile geometries

A woven composite material is an FRP material in which the fibres have been prefabricated to form a textile. The basic building block of a textile is the yarn in which fibres are either bundled together as rovings, or twisted into threads. Many types of textile exist, classified both by the manufacturing method (eg. weaving, braiding, stitching or knitting), and the pattern in which the yarns have been interlaced [25]. The most basic woven textile consists of two orthogonally orientated sets of yarns, warp and weft yarns. During the manufacturing of the textile, the warp yarns are spanned across a frame, and the weft yarns are passed back and forth through the warp yarns to form the textile. Some examples of typical weave patterns are shown schematically in Figure 2.1. The first two are examples of balanced weaves, i.e. the warp and weft fibres are equally distributed above and below the mid-plane of the fabric. Satin weaves by contrast are unbalanced about the mid-plane of the fabric. The weave pattern influences the performance of the textile during both the manufacturing of the composite and the service life of the composite component. This work will focus on basic 2D woven textiles as described above.

An important concept in the description of textiles is that of yarn or fibre crimp. Crimp refers to the out-of-plane undulations imparted on the yarn by the weave ge-

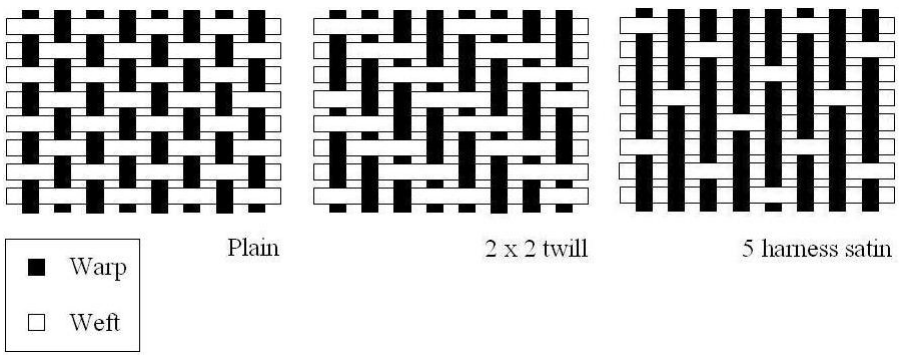

Figure 2.1: Examples of common 2D weave geometries

ometry. This is dependent on the yarn width, yarn thickness and yarn spacing [26] as shown in Figure 2.2, where w is the yarn width, t is the yarn thickness and s is the yarn spacing. The three parameters result in an out-of-plane orientation of the yarn (angle βmax). The crimp is usually not the same in the warp and weft yarns.

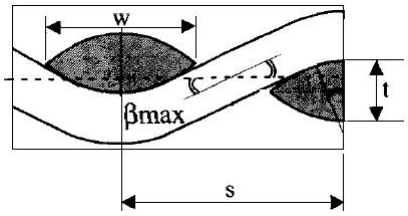

Figure 2.2: Yarn crimp in a woven material [27].

The geometry of the textile is controlled by a number of parameters. Starting with the yarn, the number and arrangement of the fibres in the yarn determines their packing density and the cross-sectional geometry. For example, a typical roving has a lenticular cross-section [28]. This leads to a thinner textile with reduced crimp compared to one made from a thread (fibres are twisted together resulting in a circular cross-section) with the same fibre count and yarn spacing. At the next level is the influence of the weaving pattern. Fabrics with fewer cross-over points such as twill or satin weaves (the yarn spacing and size being the same), tend to permit greater degrees of shear by the process of trellising (or textile shear), allowing the fabric to drape well over surfaces with complex curvature [29]. Shear deformations up to 50° in twill woven textiles have been reported [30]. The number of cross-over points also influences the compressibility of a textile stack through mechanisms such as nesting [31], thereby influencing the overall thickness and fibre volume fraction of textile laminates.

The geometry subsequently influences the mechanical properties of the textile composite. The distribution of stress and strain concentration loci is critical to the failure behaviour and strength of the laminate, while yarn crimp influences the stiffness, both in and out of the plane of the textile [32]. During the weave process, the tension and spacing of the warp yarns are used to control the fibre crimp in both warp and weft yarns. Thus, even nominally symmetric weave geometries, such as plain weave, may be manufactured to have different mechanical properties in the two orthotropic directions.

2.2 Manufacture of composite materials

Woven composite components are most commonly manufactured using a moulding process. The manufacturing processes differ in how the resin and the fibres are brought together. For woven textiles with thermosetting polymer matrix systems there are essentially three approaches: wet lay-up, resin transfer moulding (RTM) and pre-impregnated fabrics (pre-preg) [33]. The processes are shown schematically in Figure 2.3. In the first two, the dry textiles are laid into a mould and the resin is introduced in liquid form. In the third, the textile is pre-impregnated with a resin which is very viscous or solid at

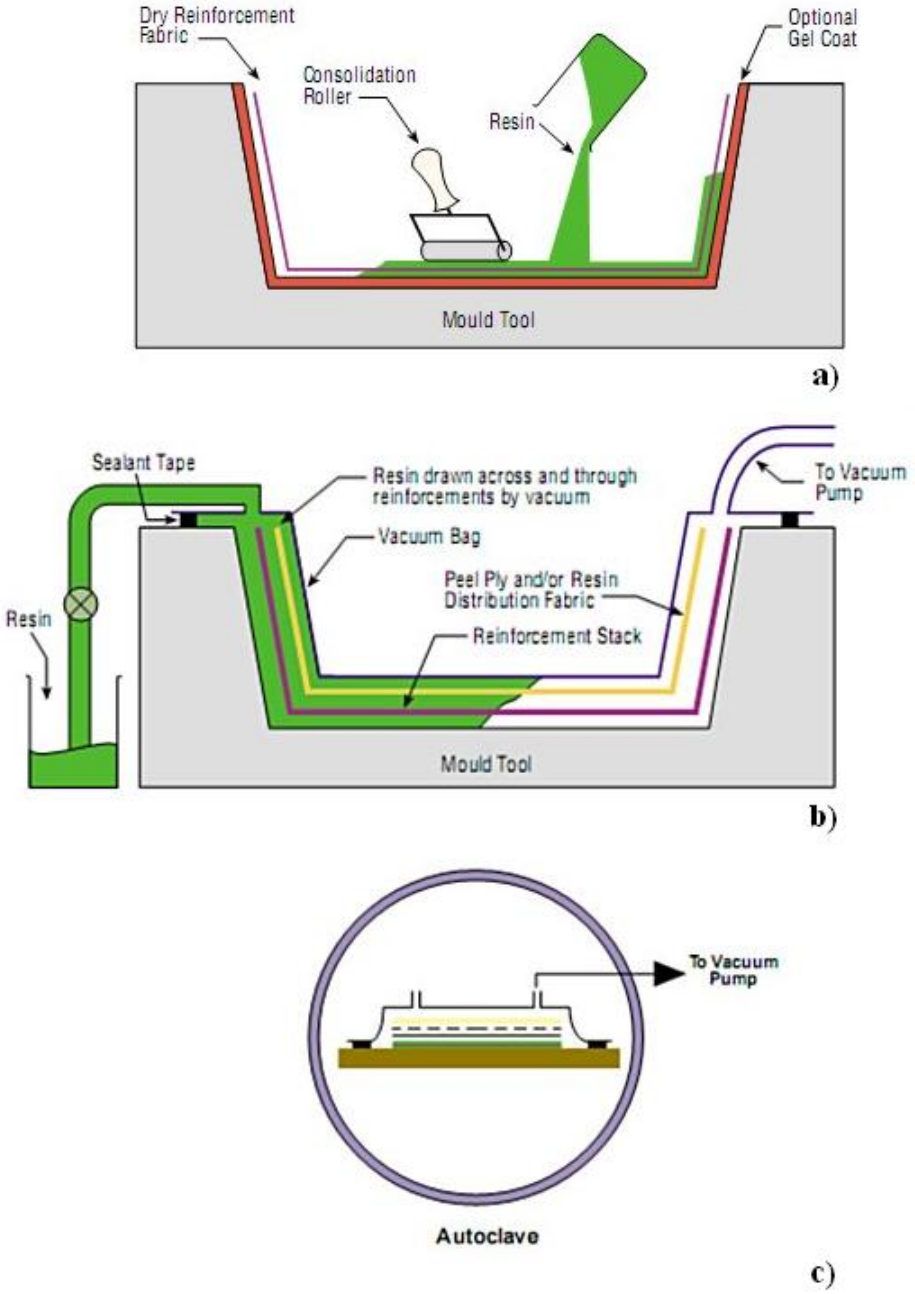

Figure 2.3: Examples of typical manufacturing methods for composite materials, a) wet lay-up, b) resin infusion, c) pre-preg with autoclave consolidation [34]

room temperature. The resin and fibres are then laid into the mould together. Thermoforming polymer matrix systems can be introduced into the fibre preform in liquid form, or in the form of combination yarns (i.e. the yarn consists of a combination of reinforcing and polymer fibres which melt to form the matrix) [33]. The discussion below focuses on manufacturing techniques for use with thermosetting polymer matrix materials.

In the wet lay-up approach, the fibres are laid into an open mould and resin is applied manually to each layer of fibres as it is laid into the mould. A vacuum can be applied after all the layers have been impregnated to improve consolidation, but typically it is left to cure in the open [33]. Good results can be achieved but the process is highly dependent on the skill of the worker and hence the quality of the product varies greatly. Whilst tooling costs are low, the process is labour intensive and hence this technique is only suited to very low production volumes, where mechanical performance is of secondary importance.

RTM encompasses several techniques in which the dry fibres are laid into a mould and the resin is drawn or injected into the part [25]. The mould can be open as shown in Figure 2.3 or closed (i.e. the fibres are sandwiched between two rigid moulds) as in the case of pressure assisted resin injection processes. Closed moulds have the advantage that higher injection pressures can be used, enabling extended resin flow paths and increased consolidation pressure and thus higher fibre volume fractions of the laminate [35]. While the tooling is more expensive, the cost of single use consumables (e.g. vacuum bag material, sealant tape, distribution mesh) is reduced. Semi-rigid, reuseable moulds have also been developed to form a cost / performance compromise between the open and closed mould RTM processes. As the resin needs to flow through the part, special consideration of injection points is necessary for the infusion of large components to ensure complete infiltration [36]. The use of a vacuum minimises the introduction of air bubbles into the part while the use of pressure ensures a high fibre and low void content. This results in improved performance compared with the wet lay-up process and better repeatability. Because the resin infiltration occurs within the confines of an evacuated mould, extraction of potentially harmful volatiles produced during the curing phase is more easily controlled, improving health and safety aspects as well. The cost of tooling and labour is comparable to that of the wet lay-up, and therefore this technique has established itself as the standard for the marine and wind turbine industries.

The impregnation of the textile in the pre-preg manufacturing route allows the resin / fibre manufacturer to accurately control the fibre to resin ratio. The curing process is then arrested so that the material can be delivered or stored, usually requiring refrigeration and a limited shelf life. The uncured resin is highly viscous or solid at room temperatures to facilitate handling during the moulding process. To ensure there is no air trapped between layers, the part is evacuated periodically after a set number of plies have been laid into the mould. The manufacture of thick laminates is therefore time consuming and labour intensive. Finally, the sealed and evacuated mould is placed in an autoclave. This provides increased consolidation pressure. An elevated temperature

is then required to enable the resin to flow, improving consolidation of the fibres and triggering the curing process. The short flow distance, controlled resin content and high consolidation pressure mean that the pre-preg manufacturing route provides the highest repeatability and best quality composite components. The labour and tooling costs are however significantly higher than with the other manufacturing routes.

A variation on the theme, sometimes termed a semi-preg process, has been developed in which the resin is manufactured into a film that is laid between plies of dry fabric [37]. This has the advantage that dry fibres and resin can be stored separately, reducing refrigerator space requirements, while control of the resin to fibre ratio is comparable to that of the pre-preg manufacturing route. The dry fibres in the stack provide channels for entrapped gas between the layers to escape before the resin is cured, reducing the need for intermidiate degassing of the part during the lay-up of thick laminates. Because the resin is pre-distributed throughout the part as a continuous film, infiltration lengths are short, improving fibre wet-out.

The choice of manufacturing process clearly influences the cost and the performance of composite materials. To maximise the performance it is necessary to minimise void content and maximise the fibre volume fraction. Evacuation of the laminate is necessary to remove entrapped air and volatiles produced during the curing process. The application of an external pressure is necessary to increase the fibre volume fraction. In the study of composite materials it is important to be aware of the exact manufacturing process and conditions. In the work described in this thesis, a vacuum assisted resin infusion process is used to enable repeatable quality at an affordable cost. In Chapter 7, some autoclave consolidated prepreg is also used for comparison.

2.3 Mechanical behaviour of woven composites

Weave geometries can be defined at several length scales in a hierarchy, often termed the micro-, meso- and macro-scales [27]. The micro-scale refers to the interaction between the fibre and the matrix, of the order of μm. The meso-scale, of the order of mm, considers the interaction of yarns within the weave, as well as the variations in the fibre volume fraction, the presence of resin rich pockets and the interaction of textile layers within a laminate. The macro-scale, of the order of m, considers the load response at the scale of the component. The mechanical behaviour of a woven composite material will first be considered in terms of how the meso-scale structure influences the macro-scale stress / strain behaviour. The meso-scale stress and strain fields that are responsible for the failure of the woven composite will be considered subsequently.

Woven composite materials show complex stress-strain behaviour. Tabiei and Ivanov [38] compared model predictions with experimentally determined stress-strain curves for a plain woven composite under uniaxial tension and compression. This showed a linear stress-strain behaviour when the warp yarns were aligned parallel to the load direction in both tension and compression. However, with the warp yarns oriented at 45° to the

loading direction, a nonlinear response was found in both the warp and weft directions in both tension and compression. This change from linear to nonlinear stress-strain behaviour due to changes in the textile orientation has also been observed in braided composite tubes [39]. This behaviour is explained through a change in the load bearing mechanism. Consider first a single ply in isolation. Of the constituent materials (i.e. fibre and matrix) the in-plane tensile and compressive stiffness is dominated by the fibre stiffness while the resin stiffness dominates the out-of-plane tensile and compressive stiffness and the in-plane shear stiffness [40]. The fibre typically has a linear mechanical response along the fibre axis, explaining the linear stress-strain response found in [38]. In the case where the fibres are orientated at $45°$ to the loading axis, the textile is subjected to a shear stress and the material behaviour is resin dominated. Failure occurs gradually, beginning with shear failure in the resin. As damage in the matrix accumulates, there is a decrease in the stiffness up to the point where the load is carried by the textile alone (i.e. the matrix failure becomes so severe that the material responds as a dry textile which typically has a low shear stiffness). Hence a nonlinear behaviour in the $45°$ direction is observed [38].

Of the weave parameters, the global fibre volume fraction and the fibre crimp are important to the in-plane tensile and compressive stiffness while fibre volume fraction, but not fibre crimp, are important to the shear stiffness [41]. The fibre volume fraction is governed by two parameters, the yarn spacing and the yarn cross-sectional geometry. A high aspect ratio cross-section (i.e. wide, flat yarns) results in higher fibre volume fractions of the textile up to a maximum of approximately 50% for a single ply of plain weave textile [27]. The increase in the yarn cross-section aspect ratio also leads to a decrease in the fibre crimp, again positively influencing the tensile and compressive in-plane stiffness of the textile.

Macroscopic properties have been used to infer the onset of damage and determine the life expectancy of the woven composites [14, 42]. Tamuzs *et al.* [42] examined the S-N curves and identified that the shape of the curve is the same for a given woven laminate, independent of the magnitude of the applied fatigue load. The tests employed balanced tension / compression sinusoidal loading between 50 and 65% of the failure loads measured in static tension. Osada *et al.* [14] by contrast have shown that failure initiation was already apparent at global stresses as low as 25 to 35% of the failure stress in tension / tension tests, depending on the type of weave and the number of laminae. A kink in the static stress / strain curve, identified using a least squares analysis, which they termed the 'knee point' [14] was used as a measure for 'safe loading'. They identified the onset of fatigue as surface cracks that form in the centre of the transverse running yarns. This was explained by the bending moments applied due to the fibre crimp, as shown schematically in Figure 2.4. This result demonstrates that textile failure cannot be homogenised at the macro-scale in the same way as the stiffness properties. Here careful consideration of the local stress and strain maxima that arise at the meso-scale

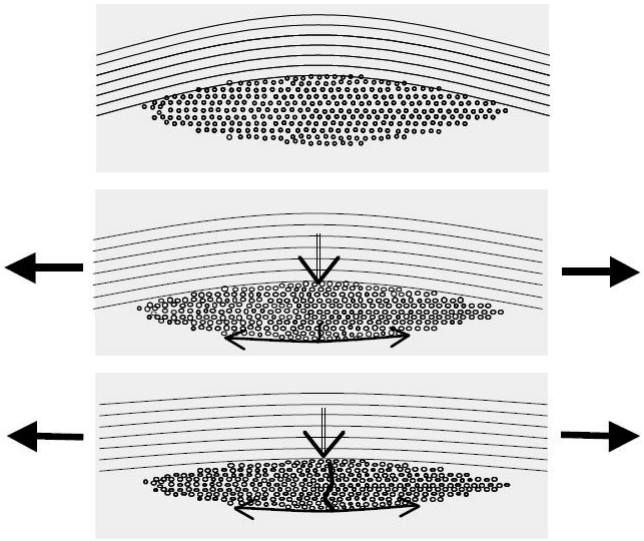

Figure 2.4: Mechanics of crack formation in the transverse running fibres. The arrows indicate the loading direction. (adapted from [14])

is required.

The 1D strain field along a yarn, parallel to the loading direction shows that the highest strain levels are located at the cross-over point, where the out-of-plane orientation of the fibres is greatest [43]. Strain concentrations are also located in narrow bands near the fibre matrix interface and along yarn edges [43, 44]. Under tensile loads, failure has been found to initiate in the resin channels between the yarns running perpendicular to the loading axis [44, 45]. The concentrations in the strain field that lead to failure at the boundaries of transverse running yarns have been shown clearly in shearography measurements of single and two ply plain weave composites by Lee *et al.* [46, 47]. Corresponding compressive transverse strain minima occur at the edges of the yarns oriented parallel to the loading direction. This stands in contrast to the results by Osada *et al.* that show cracks forming along the yarn centre line in single and multiple ply plain and satin weave composites [14]. The explanation that a bending moment on the transverse running yarn, induced by a through thickness force resulting from the crimp in the yarns parallel to the loading direction is corroborated by measurements of a compressive strain in the through thickness direction, between the warp and weft yarns on the textile mid-plane [8]. The discrepancies between the two findings, regarding the location and the cause of damage initiation in textile composites are testament to the complexity of woven composite materials.

To add complication, stress and strain concentrations can be modified by irregularities and discontinuities at the meso-scale, arising during the manufacture of a component [30]. In particular, stacking misalignments and textile deformations due to curvature of the component can lead to nesting of adjacent lamina and changes to the weave geometry due to textile shear. This in turn influences the interaction between adjacent layers and the resulting failure modes. Through thickness stresses resulting from

out-of phase yarn undulations can provide support to internal plies, delaying the onset of inter-yarn delamination and fibre kinking [48] and changing the failure mechanisms. Furthermore, Smith and Swanson [49] demonstrated that the yarn size is critical to the failure strength because thicker yarns with more fibres tend to contain greater variation in the fibre alignment and packing density.

It is clear from the above discussion that stress concentrations arising from the meso-scale complexity of woven composites do not follow the regular pattern of the weave, *per se*. The combination of macro-scale (i.e. component) geometry, number and type of textile lamina and the manufacturing process result in a unique distribution of stress concentrations and material properties. It is clear therefore that non-destructive experimental techniques that can be applied to study whole components at various scales are required, since a 'generic composite' and a generalised theory that incorporates all aspects of the material have not, and perhaps cannot, be defined.

2.4 Experimental investigations of woven composite behaviour

Single point measurements, such as those obtained using strain gauges, and globally averaged measurements, such as those obtained from clip gauge extensometers, are used to study the macro-scale behaviour of woven composite materials. For example, strain gauges have been used to show that differences in the fibre preparation influence the global stiffness of textiles [43]. However, to capture the meso-scale behaviour, the heterogeneous nature of woven composite materials requires full field techniques to be employed. This section considers some of the full field techniques that have been used to study woven materials specifically. Applications of TSA to woven composite materials will be discussed later in Chapter 3.

2.4.1 Raman spectroscopy

Raman spectroscopy uses the scattering of a laser by the molecular structure of a material to investigate modes of interaction between molecules. Peaks in the spectra, known as Raman bands, can be associated with certain vibrational modes [50]. The use of Raman spectroscopy to measure strains requires that the material has one or more strain dependent Raman bands. A number of high strength polymer fibres including poly(*p*-phenylene terephthalamide)(Kevlar 49) and certain crystalline geometries in carbon fibres have been found to display strain dependent Raman bands [51]. A study by Lei and Young [43] has used Raman spectroscopy to investigate the deformations, and the onset of fibre / matrix debonding in plain woven composites. Although it is a single point measurement, because it is non-contacting, the full field strain can be obtained by scanning. High resolution, accurate measurements at well defined points can be obtained at the meso-scale. The study showed variations in the one dimensional strain field along a weft yarn (the weft yarn was orientated parallel to the loading direc-

tion) for three nominally identical fibres with differing surface treatments [43]. However, the reliance on using suitable materials with well defined Raman spectra restricts the range of woven composites to which the technique can be applied.

2.4.2 Interferometric methods

Interferometry encompasses numerous techniques including holography, shearography, and moiré interferometry [52]. The techniques are all based around diffraction patterns obtained when light falls on a structured surface, be it a grid or a speckle pattern [52]. This surface pattern can either be mechanically applied or, as in the case of laser speckle intereferometry, be created by the speckle that results when laser light falls on a textured surface. Deformations in the pattern cause a change in the diffraction pattern and it is possible to correlate the two. The techniques are very sensitive to small deformations, and can be used to measure not only in-plane strains, but also out-of-plane deformations. Shearography techniques have the advantage that they measure the gradient of deformation, i.e. the strains directly as opposed to measuring displacements from which the strains are inferred [52]. Extremely precise measurements can be obtained, as demonstrated by Weissmann and Post [53], but the sensitivity to edge effects, that can be caused by normal fibre missalignment make the technique difficult to use for non-idealised woven composites [54, 55].

2.4.3 Digital image correlation

Digital image correlation (DIC) is fast becoming one of the most popular optical strain measurement techniques, assisted by the rapid increase in computing technology and power and decreasing cost of digital cameras. Applications to woven composite materials are accordingly numerous, for example [22, 44, 56, 57, 58]. The idea behind the technique is simple: if it is possible to identify in an image, two or more points on a specimen surface, it is possible to measure the relative displacements of the points in two different images, and hence compute the strain. The challenges, and hence the differences between the various systems available on the market, lie in developing a suitable algorithm capable of recognising patterns in images. Random speckle patterns are applied to the surface of a component to provide a contrast. The contrast pattern within a defined area in the image provides a unique signature for a point on the surface [59]. The larger this area, the more accurately it can be traced. However, this leads to a reduction in the spatial resolution of the technique. The accuracy and precision of the technique is a pay-off between spatial and strain resolution. The algorithms that correlate the displacements on the surface have also proven to be very sensitive to the size, shape, and distribution of the speckle pattern [60]. The ability to use standard digital cameras and the availability of off-the-shelf systems makes it a very attractive technique to industry as a low cost, black-box solution to strain measurement.

2.4.4 Summary

The above listed techniques are a brief summary of the types of full-field experimental techniques that have been applied to woven composite materials. For optical techniques, the spatial and strain resolution are dependent primarily on the optics used and this can be very high, in particular for the interferometric techniques. However, with the exception of Raman spectroscopy, the above techniques have in common the requirement for a recognisable pattern on the material surface, be it a grating or a speckle pattern. The quality of the measurements is highly dependent on the quality of the pattern. This requirement not only limits the area of study, to the area of the applied pattern, but the techniques are limited to the measurement of the surface strain field. Through thickness effects can only be inferred by their effect on the surface strain field, or obtained by studying cross-sections, in which case specific edge effects need to be considered. Finally, the techniques suffer, as do all optical techniques, from the lack of a standard reference material or reference specimen for calibration [61]. While this last point remains an issue to be addressed by standards organisations, a truly non-contacting technique able to obtain measurements over a large range of scales, directly related to the material strains, would form a useful addition to the experimental mechanics toolbox.

2.5 Modelling the behaviour of woven composites

The multiscale nature of textile materials (micro-, meso-, macro- as described in section 2.3) is utilised in modelling woven composite materials to study different aspects of the material response. At each consecutive scale in the hierarchy, the behaviour of the smaller scale is homogenised [27]. The motivation behind many modelling studies lies in the implementation of the model as part of a finite element analysis (FEA) of a component. Woven composites differ from traditional laminates through their complex geometry at the meso-scale. Many studies considering the mechanical and thermal behaviour of woven composite materials therefore focus on obtaining homogenised material properties for application to structural analysis at the macro-scale.

The near infinite variations in weave geometry and the large number of parameters that are difficult to control, pose a problem for physical test programs. Modelling allows the definition of a finite number of parameters whose influence can be tested in a 'controlled environment'. Numerical models make use of the repetitive nature of the meso-scale structure through the concept of a 'unit cell' model. The unit cell is defined as the smallest repeating unit of the weave geometry. This is then modelled in detail, using suitable boundary conditions, to obtain a set of homogenised material constants for the next level in the hierarchy. Validation of the model against the macro-scopic properties is common because these can readily be obtained from a tensile test and strain gauges. The simplifying assumptions at the micro- and meso-scale are however not validated by this type of approach. For studies of the failure mechanics which are

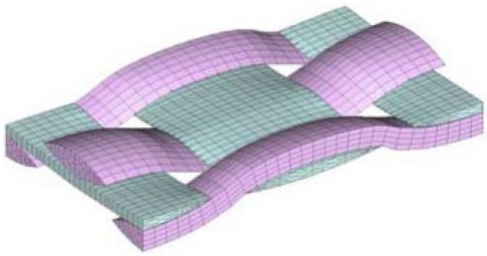

Figure 2.5: Example of a 3D unit cell of a plain weave textile for FEA [32]

controlled by the micro- and meso-scale behaviour, it is therefore important to validate the model against full-field data at an appropriate resolution.

An example of a typical unit cell for a plain weave is shown in Figure 2.5. For simple weave geometries such as the plain weave, the unit cell is relatively small and easily modelled. However, for more complex weave patterns such as satin weaves, the unit cell quickly becomes significantly larger. Careful consideration of how to define the unit cell boundary conditions enables the use of smaller repeat units as demonstrated in [62].

Among the significant milestones in the modelling of textile composites are the work by Ishikawa and Chou in the 1980's [21], Naik and Ganesh in the early 1990's [63] and a project begun by Vandeurzen et al. in the mid 1990's [27, 40]. The early models developed by Ishikawa and Chou involved very simple approximations of the textile geometry, to a large extent limited by the computing power at the time. These included, (i) the mosaic model in which the unit cell was broken into 'tiles' or 'bricks' of two ply, asymmetric laminates, disregarding the continuity of the fibres, (ii) the undulation model, which took into consideration the continuity of the fibres at the cross-over points and was aimed at the modelling of plain woven composites, and (iii) the bridging model, which combined the mosaic and the undulation models to better represent satin weave composites. The models were based on classical laminate theory (CLT) [64] and were found to give good approximations of the in-plane stiffness of a range of common textile composites. The bridging model is shown schematically in Figure 2.6.

Naik and Ganesh [63] developed a closed form analytic solution that incorporated improved geometric detail. The yarn centreline was represented as a smooth curve and the yarn cross-section was modelled as an ellipsoid. The resulting unit cell then consisted of warp and weft yarns and pure resin regions. The effects of varying the yarn shape on the woven geometry and the resulting mechanical properties could thereby be modelled with improved accuracy.

Large improvements in the available computing power have lead to an increase in modelling efforts, in particular with the use of finite element (FE) methods. Developments in mesh generation techniques, together with the increase in memory and processing power, have enabled the advantages of FE models, such as the inclusion of random defects without the need to make assumptions about the stress or strain state within the unit cell [40], to be increasingly exploited. Nevertheless, attempts to reduce the high computational cost (and associated time) through the developments of simplified

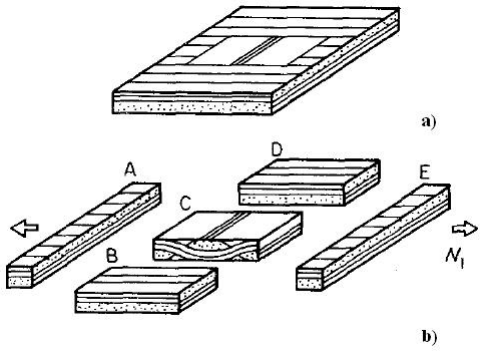

Figure 2.6: Schematic of the bridging model showing a) part of a unit cell and b) how it is divided [21].

models [65], special elements [66, 67] or by means of post-processing stages applied to simple models [68] are still very much current.

One of the drawbacks of many of the modelling approaches, in particular regarding FE models, is their limitation to only a small number of different scenarios, i.e. weave geometry or laminate configurations. Examples are found throughout the literature in which a series of individual models are developed to account for something as specific as an increase in the number of plies within a textile laminate [69]. This motivated the development of software packages that could be used easily to provide a large variety of geometric models including the corresponding FE meshes. Two such software packages are known to the author: WiseTex developed at the Katholieke Universiteit Leuven [70] and TexGen developed at the University of Nottingham [71]. WiseTex is a commercially available software package (WiseTex) based on an object orientated modelling approach, beginning with a library of basic building blocks from which higher order elements in the micro-, meso-, macro-scale hierarchy are assembled [70, 72]. TexGen utilises a general vector path description to define virtually any weave geometry [71]. The availability of generic modelling software and the modular approach taken by both developments provides flexibility for a wide range of characteristic textile composite behaviour to be investigated, thereby facilitating the exploitation of FEA for evaluating increasingly complex textile composites.

2.6 Scope for the development of a full-field stress analysis tool

Woven composite materials display a complex mechanical behaviour due to the complex and varied structure at the meso-scale. Macro-scopic averaging of the meso-scale heterogeneity is often sufficient for stiffness, but not for failure predictions. Much work is ongoing in developing numerical models to improve understanding and facilitate the design of woven composite structures. Validation of new models will therefore remain an important thrust in the development of experimental techniques. The random distribution of inhomogeneities and discontinuities within composite components means that

local defects may not be captured by modelling efforts in the design of even fairly simple structures. The use of non-contacting, full field techniques is therefore paramount to improving both the understanding of the behaviour of woven composite materials, and the inspection of existing structures for damage, manufacturing defects and design flaws.

The dependence of current optical techniques such as interferometry and DIC on the existance of surface patterns limits the range of scales at which they can be effectively applied. It also poses important concerns regarding the ability of a suitable pattern to be applied, which can be influenced by both the skill of the operator and the test environment. What is currently missing is a technique that can be employed to examine components manufactured from generic woven composites that is both easy to use, requires minimal surface preparation and has the capability of identifying variations in the strain field over a large range of spatial scales.

TSA provides both full field and non-contacting measurement of the strain induced temperature change, thereby addressing the current technology needs. Spatial resolution is purely a factor of the optics employed and therefore the technique provides flexibility to be employed over a large range of scales. It is therefore an attractive technique for the study of woven composite materials.

Chapter 3

Application of TSA to Composite Materials

3.1 Infrared thermography

TSA relies on the use of an IR detector to measure the small change in temperature in a material as it undergoes a change in stress. Electromagnetic radiation is emitted across a wide spectral range by all matter at temperatures above absolute zero. IR refers to the spectrum of electromagnetic radiation with wavelengths in the range from 770 nm to 1 mm [73]. The nature of this radiation depends above all on the temperature of the source. In 1900 Planck established an analytical equation describing how the radiated energy from a source varies as a function of temperature and wavelength. This can be written in the form [74]:

$$r(\lambda, T) = \frac{2\pi c^2}{h\lambda^5} \left(e^{\frac{ch}{\kappa \lambda T}} - 1 \right)^{-1} \tag{3.1}$$

where r is the radiant emittance, λ is the wavelength, T is the temperature of the source, c is the speed of light, h is Planck's constant and κ is Boltzmann's constant.

The above treatment assumes an idealised source known as a 'black body', which is defined as a source that absorbs equally and completely all incident radiation, regardless of the angle of incidence, spectral composition and polarisation [74]. Real materials differ from black bodies in that they also reflect and transmit incident radiation. Absorptance, transmittance and reflectance are defined as the respective proportions of the incident radiaton that are absorbed, transmitted and reflected. Kirchhoff showed that the absorption properties of a material are congruous to the emission properties; good absorbers are good emitters [75]. In IR thermography it is therefore common to refer to the emissivity of a material. The emissivity is the ratio between the emitted radiation of a material at a particular temperature compared to the emitted radiation of a black body at the same temperature and is a function of both λ and T as follows:

$$\epsilon(\lambda, T) = \frac{r(\lambda, T)}{r_{bb}(\lambda, T)} \tag{3.2}$$

where ϵ is the emissivity and the subscript bb refers to the black body [73]. Real sources can be either grey bodies, i.e. the emissivity is constant over all wavelengths, or selective, i.e. the material emits only within certain wavelength bands. The emissivity is not only specific to a material but also depends on the surface preparation. For instance, a rough surface typically has a higher emissivity than a polished surface. When using the IR emissions to measure the temperature of a source it is therefore important to know the emissivity of the particular object under study [76].

By setting either λ or T constant, equation 3.1 can be used to produce two families of curves: isothermal (T constant) and isochromatic (λ constant). Figure 3.1 shows a set of isothermal curves showing the radiated energy across a spectrum of wavelengths from a source at room temperature. It can be seen from Figure 3.1 that at room temperature the maximum radiant emittance comes from the band of wavelengths lying in the IR spectrum. It is for this reason that IR radiation is commonly used for temperature measurement.

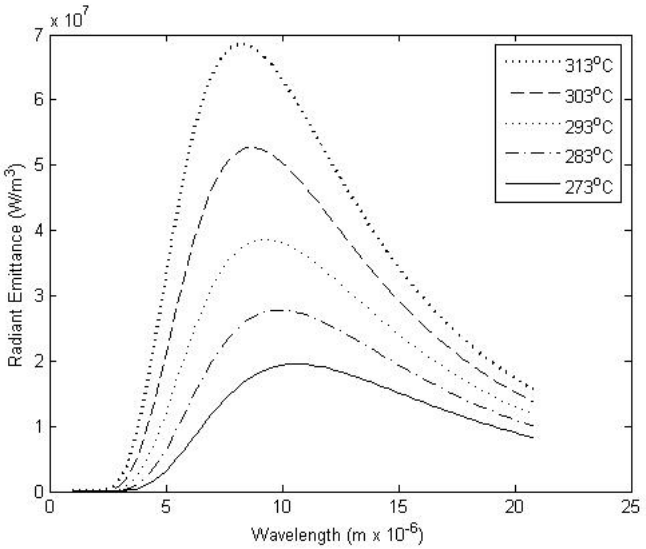

Figure 3.1: Isothermal curves obtained using Planck's relationship.

Modern IR detectors can be classified in two groups: thermal detectors and photo detectors. Thermal detectors respond to incident radiation by changing temperature. A temperature related effect is then used to measure the change in temperature from which the absorbed energy and thereby the incident radiated energy can be obtained. Photo detectors by contrast respond directly to the incident radiation; an electron in a semiconductor material is excited by an incoming photon and raised from a low to a high energy state, thereby changing the electric properties of the semiconductor. The types of photo detector are classified based on the effect that is measured, i.e.: in a photovoltaic detector the free electron is excited on a potential barrier such as a p-n junction, creating a voltage across the junction [77]. Photo detectors offer the highest sensitivity combined with fast response rates in comparison to thermal detectors. It is for this reason that photo detectors are used for TSA.

Since Belgen [17], in the late 1960's, first demonstrated the feasibility of using IR thermography for TSA there have been several systems developed specifically for this purpose. These can be divided into two categories: single detector scanning systems and staring focal plane detector array systems. In the single detector scanning systems a set of mirrors is used to direct the detector at a point on the surface of the component under observation. An image is created by adjusting the mirrors to scan the entire region of interest, pausing at each point to take a measurement. Each point at which the mirrors pause forms one pixel in the image. The staring focal plane array detectors comprise many detector elements arranged on a grid. A set of lenses focuses an image onto the grid and each detector output forms one pixel in the image. This reduces the data acquisition time from hours to seconds, thereby enabling quasi-real-time full field stress data to be obtained.

The original TSA system, the SPATE (Stress Pattern Analysis by Thermal Emissions) is an example of a single detector scanning system. This was developed by SIRA in the early 1980's [15]. The first commercial systems became available in the mid 1980's and have been used in TSA work as recently as 2005 [78]. One of the challenges faced in TSA is the measurement of very small changes in temperature. It is frequently quoted that the temperature change associated with a stress change of 1 MPa in steel is of the order of 1 mK [24], approximately one order of magnitude smaller than the signal noise. To accurately measure the small changes in temperature, the system employed a lock-in amplifier. The system relied upon a cyclic (typically sinusoidal) load. The temperature signal was then filtered using a reference signal from the load cell to extract only the temperature fluctuations occurring at the loading frequency. The use of a reference signal enables a phase angle between the load and the temperature changes to be obtained. This process is standard practice in almost all TSA systems to date. In Japan, JEOL have also developed an IR detector system capable of TSA measurements. Of the several versions of the system referred to in the literature, two versions with application to TSA are known to the author, the JTG-8010 [79, 80] and the JTG-7200 [81]. Both are single detector scanning systems that operate in a similar manner to the SPATE system.

In the early 1990's the first TSA systems to use staring array detectors were developed. In Australia Wong and Ryall developed a system called FAST (Focal-plane Array for Synchronous Thermography) [82, 83]. At the same time Stress Photonics, together with NASA developed the DeltaTherm system which is probably the second most frequently cited system in the literature after SPATE. The DeltaTherm system was essentially a further development from the SPATE system, employing the same algorithms but using digital instead of analogue processing.

Other efforts include work by Pitarresi *et al.* [84] and Galietti *et al.* [24] to develop a generic software for processing IR images into thermoelastic stress maps. In the case of Pitarresi *et al.* [84] the intention was to enable the use of off-the-shelf IR detectors, the aim being to reduce the cost of TSA equipment, thereby making it more widely available. The work by Galietti *et al.* [24] aimed to enable TSA of components under

random loading conditions in the absence of a reference signal.

The system used in this work has been developed by Cedip Infrared systems. It differs from earlier systems in that it has not been developed for the sole purpose of TSA, but is designed from the start to encompass other thermography techniques as well. This system is described in greater detail in Chapter 4.

To obtain stresses from the thermoelastic temperature change it is necessary to calibrate the TSA system in terms of stress. Reference [85] summarises different stress calibration procedures as applied to the SPATE system. Three methods are identified as listed below:

1. direct calibration using known detector and material properties,
2. calibration against a measured strain (i.e. from a strain gauge rossette),
3. calibration against a calculated stress.

The first technique requires the detector to be radiometrically calibrated to establish the relationship between the detector output and the temperature. In the single detector SPATE system, the detector responsivity could be used for this purpose. However, the technique is not regarded as very accurate as errors in each of the material properties combine to produce significant total errors [86]. The more common approach in experimental work is to use calibration procedures 2 or 3, for example in [87] and [88]. Procedure 2 can be applied either using a calibration specimen or a region of known uniform strain on the component of interest. It is important that the point at which the thermoelastic measurement is made must experience the same strain conditions as the point where the strain is measured. Procedure 3 has the advantage that knowledge of the material and detector properties is not required. Instead, a representative calibration specimen with a well known stress distribution is required. In [87] for instance a separate calibration specimen was required for the foam core and face sheet materials. In the case of orthotropic materials the orientation of the test specimen is also important [89].

Work in other fields includes the SPOTS (Standards Project for Optical Techniques of Strain Measurement) project, in which the requirement for a global standard for the calibration of optical measurement techniques is highlighted [61, 90, 91].

3.2 TSA theory for orthotropic materials

Fibre reinforced composite materials are orthotropic materials [64] in which the primary axes of the material are defined by the orientation of the fibres. To study the behaviour of such materials it is useful to define three sets of coordinates, shown in Figure 3.2. The first set (1 and 2) are the orthogonal axes of symmetry of the material (principal material directions). The second set (x and y) are the directions of the principal stresses. The third set (L and T) are an arbitrary set of axes of interest. Because TSA is a surface

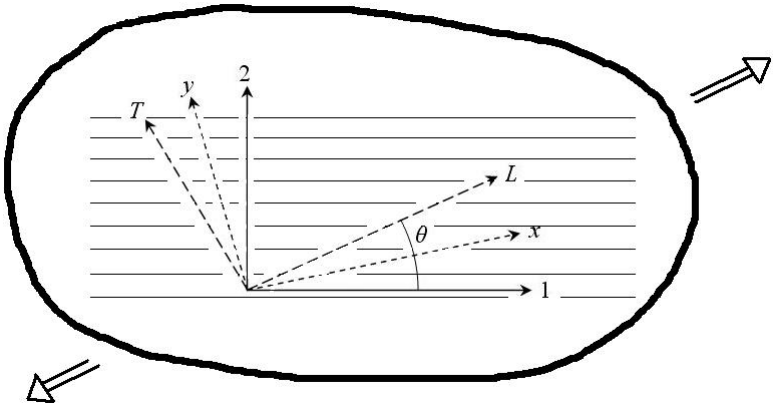

Figure 3.2: Coordinate frames of reference: x, y principal stresses; 1, 2 principal material axes; L,T directions of interest (e.g. the loading axis in a tensile test coupon)

sensing technique, it is the angles relative to the material coordinates (1 and 2) of the surface ply that are normally of interest.

Early in the development of the technique TSA found application to composite materials. In 1986 Stanley and Chan [92] were using TSA to investigate the stresses in a composite cylinder. An expression of the thermoelastic response in terms of stress for a homogeneous orthotropic material was subsequently presented in [93]:

$$\Delta T = -\frac{T}{\rho C_p}\left(\alpha_1 \Delta\sigma_1 + \alpha_2 \Delta\sigma_2 + \alpha_6 \Delta\sigma_6\right) \tag{3.3}$$

where ΔT is the change in temperature, T is the absolute temperature, ρ is the density, C_p is the specific heat at constant pressure, α is the coefficient of thermal expansion (CTE) and $\Delta\sigma$ is the change in stress with subscripts 1, 2 and 6 referring to the material coordinates in contracted tensor notation with 6 referring to the 1-2 shear term.

It is apparent from equation 3.3 that the individual stress components in an orthotropic material are linked to their corresponding CTE. This has the effect that the thermoelastic response from an orthotropic material is sensitive to the relative magnitudes of the orthogonal stresses applied. Equation 3.3 also implies that the thermoelastic response from an orthotropic material is influenced by the shear stress, contrary to isotropic materials. However, Potter [94] highlights that there is no material property α_6 that couples the change in temperature with a shear deformation. It is noted that in more recent work, for example [95], which provides a general review of TSA, this shear term does not appear.

In woven materials where the fibre orientation varies across the surface, the variation in the local orientation of the fibres needs to be considered when applying TSA. Instead of relating the thermoelastic response to the stresses, another approach is to consider the thermoelastic response in terms of strains. This has been done explicitly in [94] and

again more recently with identical result in [96] giving the expression:

$$\rho C_p \frac{\Delta T}{T} = -\Big\{[(\alpha_1 Q_{11} + \alpha_2 Q_{12})m^2 + (\alpha_1 Q_{12} + \alpha_2 Q_{22})n^2]\Delta\varepsilon_L + [(\alpha_1 Q_{11} + \alpha_2 Q_{12})n^2 + (\alpha_1 Q_{12} + \alpha_2 Q_{22})m^2]\Delta\varepsilon_T + [(\alpha_1 Q_{11} + \alpha_2 Q_{12})mn - (\alpha_1 Q_{12} + \alpha_2 Q_{22})mn]\Delta\gamma_{LT}\Big\} \tag{3.4}$$

where $m = cos\theta$, $n = sin\theta$ and θ is the angle between the material axes (1, 2) and the directions of interest (L, T) as shown in figure 3.2, $\Delta\varepsilon_L$ and $\Delta\varepsilon_T$ are the change in direct strains, $\Delta\gamma$ is the change in shear strain and Q_{11}, Q_{22} and Q_{12} are the principal material stiffness terms [64] defined as:

$$\begin{aligned} Q_{11} &= \frac{E_1}{(1 - \nu_{12}\nu_{21})} \\ Q_{22} &= \frac{E_2}{(1 - \nu_{12}\nu_{21})} \\ Q_{12} &= \frac{\nu_{21}E_1}{(1 - \nu_{12}\nu_{21})} \end{aligned} \tag{3.5}$$

where E_1 and E_2 are the Young's moduli and ν_{12} and ν_{21} are the Poisson's ratios in the principal material directions of the lamina.

This strain based approach is useful when studying laminates [94]. For example, in a simple tensile strip, while the stress varies in the through-thickness direction, the strain is uniform. Hence a single measurement of the longitudinal and transverse strains in a tensile strip specimen can be used to calibrate the response from a given laminate in conjunction with equation 3.4 [96]. For this reason the TSA data obtained from woven composite components will be explored in relation to the strain field in this work.

3.3 Heat transfer in inhomogeneous materials

When considering the mechanical behaviour of composite laminates, the material is typically treated as being homogeneous. At smaller scales however, this treatment may not necessarily apply. As described in section 2.5 a composite material can be defined with reference to a hierarchy of different length scales. At the micro-scale, fibre reinforced composites consist of two distinct components, the individual fibres (typically 20 μm diameter for E-glass) and the resin. In standard laminates, the fibres are aligned in plies, typically of the order of 0.1 to 0.3 mm thick. In woven textiles, the fibres are bundled into tows or yarns (typically of the order of 0.1 to 0.3 mm thick and 1 or 2 mm wide). At the top of the hierarchy, the macro-scale, are laminates and components with length scales ranging from tens of milimetres to numbers of metres. As discussed in Chapter 2, the validity of the homogeneous assumption depends on the scale at which the composite is being viewed. At the macro-scale, the composite can generally be considered homogeneous and the mechanical properties are averaged

across the laminate. When viewed at the micro-scale, differences in the mechanical properties of the fibre and the resin become significant and the composite cannot be treated as homogeneous. Therefore, when considering the general stress distributions of a component, global laminate properties can be applied. However, when studying for example, localised failure within a component, it may be necessary to consider the interface between individual plies within the laminate.

The same idea applies when considering the thermoelastic response from a composite material. When adjacent components (i.e. the fibre and the matrix) have a different thermoelastic response, this leads to temperature gradients as the component is excited and hence the possibility of non-adiabatic conditions. The steepness of the temperature gradient depends on, a) the length scale across the interface and b) the difference in the stress induced temperature change between the adjacent regions. The question of non-adiabatic behaviour then depends on, a) the time scale over which the temperature difference occurs and b) the conductivity of the materials. A more complete formulation of the thermoelastic relationship for an isotropic material can be written to include the heat transfer as follows [97]:

$$\frac{\partial T}{\partial t} = \frac{1}{\rho C_p}\left[k\nabla^2 T - T\alpha\frac{\partial(\sigma_1+\sigma_2+\sigma_3)}{\partial t}\right] \tag{3.6}$$

where k is the conductivity and t is time.

The formulation given in equation 3.6 includes two distinct terms in the brackets on the right hand side of the equation; the first term, $k\nabla^2 T$, describes the spatial heat transfer due to a temperature gradient, the second term, $\frac{\partial(\sigma_1+\sigma_2+\sigma_3)}{\partial t}$, describes the adiabatic temperature change due to the change in stress. True adiabatic conditions can only be achieved if either $k = 0$ or $\nabla^2 T = 0$. In a real material k is never exactly zero, although in some materials, for example glass reinforced epoxy, k is very small. $\nabla^2 T$ can equal zero under certain load conditions, for example in a tensile specimen manufactured from a homogenous material and subjected to a uniaxial load, in which case the adiabatic temperature change is uniform throughout the material and does not lead to temperature gradients. In experimental work, it is however more common to approximate adiabatic conditions. At this point it is useful to clarify some terminology. The time scale (∂t) is associated with the rate of change in stress and is controlled by the user. There is also a time scale associated with the heat transfer. This is controlled by the conductivity of the material and the length scale, which control the temperature gradient. In the following, 'time scale' will refer to the scales associated with the rate of change in stress and 'length scale' will refer to scales associated with the heat transfer rate. Note also that in this case the through-thickness stress (σ_3) cannot be neglected. This is because thermal conduction occurs both in-plane and through the thickness of the specimen. Whilst it is standard practice, for example in CLT, to assume that σ_3 is zero in thin laminates, in a woven material, σ_3 can be non-zero below the surface and must therefore be considered.

Non-adiabatic conditions manifest themselves in a change in the magnitude of the thermoelastic response, and in a shift in the phase angle of the IR signal relative to the loading cycle. This latter effect can be used to determine if the thermoelastic response is influenced by an adiabatic effect. Under ideal adiabatic conditions the phase angle should be uniform across the whole specimen, with only a 180° phase shift between regions of tension and compression. Local deviations in the phase angle can therefore be used to identify non-adiabatic behaviour.

To approximate adiabatic conditions the time scale (∂t) is made small (by increasing the loading frequency) so that the second term dominates equation 3.6 and the heat transfer term can be ignored. However, when considering very small length scales such as the individual tows in a woven material, the thermal gradients become large, and so heat transfer cannot be ignored. Solving the heat transfer equation for a cylinder of infinite length inside a continuous medium (representing the fibre embedded in the matrix), Wong [98] demonstrated, using the example of carbon-fibre reinforced epoxy laminates, that at the micro-scale, the heat transfer between the fibres and the matrix occurs so quickly, that a uniform temperature throughout the composite is reached almost instantaneously. This implies that a single lamina, in which the fibres are all aligned, can be considered as a homogeneous material, with a thermoelastic response based on the properties of the composite as a whole. This justifies at the scale of a single ply or for a unidirectional composite, the treatment of the composite as a homogeneous material.

At the meso-scale however, heat transfer between adjacent plies of differing orientation occurs over greater length scales. Quasi-instantaneous heat exchange between the adjacent plies does not occur and hence a homogeneous treatment of the composite at this scale is not possible. If it is not possible to set the time scale sufficiently small, then non-adiabatic behaviour can be important [99]. In order to approximate adiabatic conditions it is necessary to select a loading rate such that the time scale of the load cycle is less than that associated with the heat transfer between plies. Solving the heat transfer equation between adjacent plies, Wong [98] arrives at a non-dimensional quantity:

$$F_0 = \frac{kt}{\rho C_p \left(\frac{l}{2}\right)^2} \tag{3.7}$$

where l is the thickness of a single ply in the laminate. Wong shows that for values of $F_0 > 2$ thermal diffusion is completed within the time scale and the material can be treated as homogenous; for $F_0 < 5 \times 10^{-3}$ heat transfer is negligible within the time scale and the adiabatic condition applies as well. For a woven composite made of glass fibre / epoxy in which the thickness of a single tow of fibres is of the order of 0.2 mm this analysis shows that a loading frequency of 30 Hz is required to achieve the quasi-adiabatic condition with regard to adjacent tows orientated perpendicular to one another. This loading rate is close to the maximum rate achievable with standard laboratory equipment and represents a minimum condition for the adiabatic assumption.

Also, a small decrease in the length scale (e.g. the use of a finer yarn) would raise the minimum loading frequency requirement. When studying the thermoelastic response at the scale of individual fibre tows in a woven glass / epoxy material, it must therefore be considered that the adiabatic assumption may not be valid in all cases.

3.4 Application of TSA to composite structures

TSA has been successfully applied to many stress analysis problems involving composite materials. Among the early work is a study that considers a woven carbon / epoxy composite material [20]. The thermoelastic data clearly shows a pattern that corresponds to the pattern of the weave. The author does not consider this in any great detail, and simply attributes the peak signals to stress concentrations resulting from the weave geometry. Instead he focuses on confirming a linear relationship between the applied load amplitude and the measured change in temperature and a practical application to a honeycomb sandwich material. However, an interesting finding made in reference [20] is that the orientation of the weave does not influence the magnitude of the thermoelastic response. This stands in contrast to what might be expected based on the theory presented in section 3.2 and suggests that an isotropic strain witness on the surface may have affected the data.

Strain witness behaviour has been a topic of discussion that has appeared repeatedly in the literature, for example [78, 100, 101]. The argument is that a thin layer of resin on the surface of the composite material can mask the thermoelastic response from the composite substrate below. This surface resin layer commonly exists as a result of the manufacturing process. The thickness of this layer varies depending on the manufacturing process and type of fibre reinforcement. Early work [102] picks up on the effect of a surface resin layer where it is referred to as 'heat leakage' rather than strain witness behaviour. In the as manufactured state, the specimens used in reference [102] had a resin layer thickness of 20 μm. By varying the thickness of the surface resin layer, a significant effect on the thermoelastic response was identified, which was dependent on both the thickness of the surface resin layer and the loading frequency. Strain witness behaviour is explicitly studied in reference [100] in which a polycarbonate coating is applied to an aluminium substrate. Here it was found that the coating acts as a strain witness as of a thickness of 0.5 mm and a loading frequency of 5 Hz. Recent studies [78, 96] have further confirmed the strain witness behaviour of surface resin layers as thin as 25 μm and loading frequencies around 10 Hz on glass / epoxy composites. A similar effect has been used in the study of pultruded composites where, instead of a pure resin layer on the surface, a 'veil' layer acts as an isotropic strain witness [103]. The reason that strain witness behaviour in composite materials is important is that it simplifies the interpretation of the TSA data. While the thermoelastic response from an orthotropic material is also orthotropic, the presence of a thin isotropic strain witness results in an isotropic thermoelastic response. In the application to woven composite materials this would serve to eliminate the problem of local variations in the orientation of the fibres

in the surface ply. However, there has always been a degree of doubt associated with the reliability of using the surface resin layer as a strain witness, and recent work [101] has highlighted the potential pitfalls of this assumption.

TSA has been applied as a tool for design optimisation. Examples of this include work conducted on T-joints in both laminated FRP [88] and foam sandwich [87] structures. In both studies the T-joints were studied from their cross-sectional views. Viewed from this angle, several different materials are presented to the detector. In the case of the sandwich structure, these included the composite in the face sheet, the foam of the core material and the resin in the bonded joint. In the lead up to the study of the joints, the thermoelastic response from each material had to be calibrated. These studies demonstrate that TSA can be applied in a quantitative manner in situations in which several different material responses are present. In the study of woven materials, the challenge is further complicated because the variations in the material response are spread across the whole structure, and although they follow a predictable pattern, the exact location of different regions on the surface of the structure may not be known *a priori*. In a study of bonded joints in pultruded composite components [104, 105] TSA was used as a tool for validation of a finite element model. As in the studies of the T-joints, a significant step in the process was the thermoelastic characterisation of the different materials within the joint. In this case, material properties that could not be directly measured were established by fitting the model data to the experimental results.

Another area in which TSA has been used is the study of damage in composite materials. Failure mechanisms in notched ceramic matrix composites were studied in reference [106] and [107]. Using TSA it was possible to measure the stress redistribution with sufficient precision to distinguish between different failure mechanisms. In a study of notched E-glass / epoxy material [108] the same idea was used to investigate the effect of interfacial properties on damage evolution. In both experiments, failure of the composite occurred in the surface ply. Reference [89] studies two types of subsurface damage in carbon / epoxy and E-glass / epoxy specimens - fibre breakage and delamination. The study shows that subsurface damage can be detected only if the effect on the stress in the surface ply is sufficiently large. Hence, under uniaxial tension, the location and extent of the fibre breakage could be detected but not the delamination.

The development and growth of damage is often combined with the generation of heat at the damage site [109, 110]. Equation 3.3 states that the change in temperature ΔT is dependent on the absolute temperature of the surface. Equation 3.1 further shows that the radiated energy increases also with temperature, hence making the detector more sensitive to small changes in temperature. A local increase in temperature will offset the thermoelastic change in temperature, leading to over estimation of the measured stress near the damage. Hence, local changes in the absolute temperature must be corrected for when acquiring quantitative data. A methodology for correcting for such changes in temperature is presented in reference [110]. In an application to damage evolution around a circular hole in a composite tensile specimen, Emery and Dulieu-

Barton [23] successfully decouple the heating effect from the thermoelastic response and calibrate the thermoelastic response in terms of strain. Thus they are able to monitor the strain field as damage progresses and provide insight into the way in which combined damage mechanisms lead to final failure in laminated composite materials. In the current work, the detector has been radiometrically calibrated, hence ΔT and T are measured directly by the TSA system. Compensation for variations in the absolute temperature of the material can therefore be accounted for by means of normalising the thermoelastic response in the form of $\Delta T/T$.

In a study on wind turbine blades, Paynter and Dutton [111] monitored the development of subsurface damage in the form of a delamination and a disbond between the internal structure and the skin laminate. At the damage sites, a thermoelastic response with a frequency of twice the loading frequency was observed. By using a reference signal at twice the loading frequency it was possible to identify damaged regions clearly in the resulting TSA data. The authors explain this as being due to local buckling of the laminate, leading to a complex load pattern in the vicinity of the damage site. In woven materials it is not inconceivable that local buckling of the fibre tows (particularly transverse tows which are in compression during a standard tensile test) may occur as fatigue damage propagates within the material.

The main outcomes of previous applications of TSA to composite materials with relevance to the current work can be sumarised as follows:

- If known, variations in the thermoelastic response from different regions on a component do not prevent the acquisition of quantitative TSA data. In a woven material these variations are expected due to the change in fibre orientation resulting from the weave.

- A resin surface layer, resulting from standard manufacturing procedures, can act as a strain witness. The thermoelastic response is then of an isotropic nature and uniform across the whole surface of the component, permitting a straight forward interpretation of the data in terms of the strain sum.

- Subsurface stress raisers can be detected using TSA provided they influence the surface stress field. The subsurface structure of the material must therefore be taken into consideration when evaluating the surface stress field.

- Heating at local damage sites needs to be accounted for by normalising the ΔT value against the mean specimen temperature T.

- Non-adiabatic conditions must be considered when applying TSA at small scales, for example, at the scale of individual yarns in the woven composite material.

3.5 Summary and motivation for current work

In Chapter 2 the need for a full field, non-contacting experimental technique to study woven composite materials was identified. The lack of a requirement or dependence on an applied surface coating, and the suitability to a large range of engineering materials make TSA an attractive candidate for this type of application.

The field of IR detection and the use of IR detectors for TSA are well established. However, to date TSA has not been used to study woven materials specifically. It has been demonstrated that TSA can be applied to composite materials, either by treating them as homogeneous orthotropic materials or by considering the response from an isotropic strain witness. This will form the basis for the investigation of woven composite materials. In applications to components comprising several materials with different thermoelastic responses, careful calibration of the individual materials has been key in obtaining quantitative data. This gives confidence that a similar strategy may be applied in the study of woven materials. However, in woven composite materials, the locations at which a different thermoelastic response is expected are not necessarily known *a priori*. A strategy for coping with this is therefore required.

The use of high resolution optics to enable damage evolution at the meso-scale to be investigated using TSA adds a new dimension to previous applications of TSA to damage in composite materials. Whether the assumption of adiabatic conditions can be applied to woven composite materials at small scales remains an open question. Opportunity exists to define a set of parameters designed to facilitate the evaluation of adiabatic conditions in woven materials.

Finally, industrial relevance may be added to the study by considering the limitations imposed by current TSA practice in which the reliance on a lock-in amplifier tether the technique to laboratory based testing. To broaden the range of applications where TSA can be used as a tool for assessing in-service components it is necessary to develop a strategy for working without either a lock-in signal, a cyclic load or both. Galietti *et al.* [24] have made some progress in this direction and there is opportunity for further work.

The work described in this thesis aims to address the challenges of using TSA to study the mechanical behaviour of woven materials. A new detector system that provides the necessary high resolution and motion compensation is investigated in Chapter 4. A strain based approach as described in section 3.2 will be used to obtain quantitative TSA data. Chapter 5 considers the inhomogenous nature of the woven materials. Characterisation of the material thermoelastic response and correlation of the TSA data to the local variations in the material response due to the weave structure form the major component of this part of the work. The high resolution capability of the IR detector used in this work is fundamental to evaluating the meso-scale thermoelastic response from the woven composite. The knowledge gained is then applied to the study of damage in woven composite materials in Chapter 6. The ability to study components under cyclic loads will be utilised to investigate the evolution of fatigue damage. Finally, in Chapter 7, a

methodology for obtaining a TSA measurement from a single transient load is assessed in terms of accuracy, precision and repeatability. The application of the new methodology to the study of damage in composite components is investigated, demonstrating the feasibility of using simplified excitations for TSA measurement. Thus the work addresses key issues associated with the need for improving the understanding of woven composite materials and the further development of TSA as an NDE tool.

Chapter 4

Evaluation of a New System for TSA

4.1 Introduction

The equipment used in this work was supplied by Cedip Infrared Systems (now FLIR). The use of this system for TSA has not been documented in the open literature. Hence it was felt that a thorough examination of the operation of the system was required. The system comprises an IR camera unit, computer system and three software packages: Altair (for viewing and processing thermal image data), Altair LI (for lock-in thermography processing, i.e. TSA) and Random Motion (for motion compensation) which run on a standard desktop PC in the Microsoft Windows environment. The detector used in this work is the Silver 480M; it comprises an array of indium / antimonide (InSb) detectors, cooled by a Stirling pump to 77 K. A high frame rate is achieved by overlaying two detector arrays which operate sequentially, allowing in theory seamless data capture. A purpose designed Cam LINK cable and frame grabber card in the PC offer data transfer rates up to 383 fames per second at full frame. The frame rate can be increased by subwindowing (i.e. using only a subset of the full array) but this has not been used in this work.

One of the draw backs of the system is that it does not have a standard interface to allow the use of a variety of lenses. An inbuilt 27 mm lens allows objects to be studied from a range of distances from approximately 150 mm to infinity. For investigating small specimens, a magnifying lens (known as the G1 lens) can be added which reduces the distance to the object to approximately 10 mm. Between 10 and 150 mm there is a gap for which no optical configuration was provided with the system used in this work.

An external trigger allows data collection to be initiated by an external event. The detector also has a number of features arising from the manufacturers wide ranging operations in thermal imaging. For instance, it is also possible to output the image to a monitor via a standard video connection.

4.2 Data acquisition

At the heart of the camera system is the detector which comprises two overlaid 320 x 256 element InSb IR detector arrays and two corresponding sets of internal buffers that enable sequential data storage; the arrays are used alternately, one capturing data while the other transfers data to its internal buffer. (The process is depicted schematically in Figure 4.1.) Each detector element voltage output is digitised independently by a designated processor housed in the camera unit and then sent to the computer as a digital signal in units of 'digital level' (DL), an uncalibrated machine specific output. The data is output in a CCIR-PAL standard video format and sent to a designated frame grabber card in the PC.

The detector is supplied with a radiometric calibration for four different temperature ranges from 5 to 200°C (5 - 40, 35 - 90, 85 - 150, 125 - 200). These are stored as eight separate files on the PC, one for each temperature range and lens configuration. IR data is always stored or streamed live in DL units. A thermal calibration file can be associated with each data set, allowing the data to be converted to temperature or radiance. It is important to note that the data is never modified by the temperature calibration file. When storing data it is necessary also to store the relevant temperature calibration file and re-associate the two at their respective locations if radiometrically calibrated data is desired. The upper limit of each temperature calibration range is determined by the saturation point of the detector elements. Increasing the exposure time increases the sensitivity of the detector at lower temperatures, but lowers the maximum measurable temperature. The exposure time is controlled by electronic shutter switches separating the detectors from the capacitors (buffers), as shown in Figure 4.1. For the system used in this work the detector has a sensitivity of 4.2 mK between 25 and 26°C with an electronic noise equivalent to 15.75 mK.

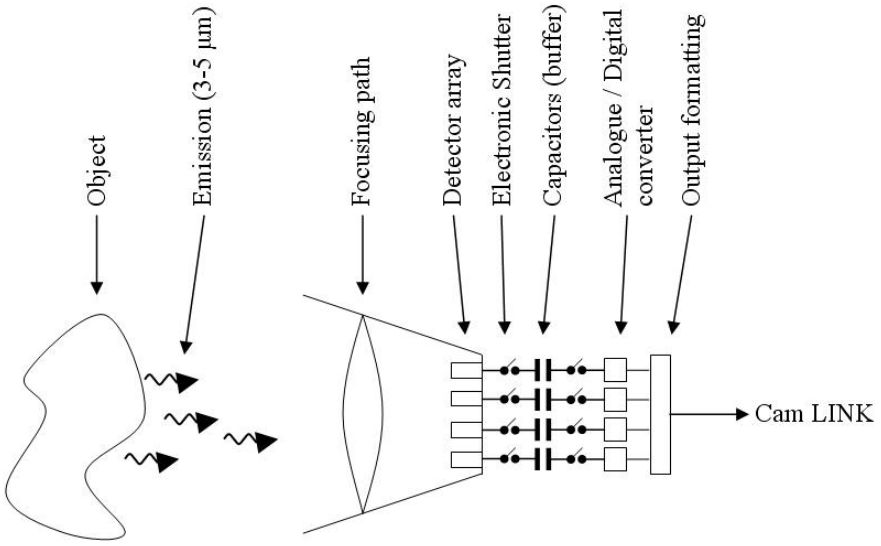

Figure 4.1: Schematic representation of the data acquisition process

As with any array based system, before taking measurements a non-uniformity correction (NUC) must be performed to correct for any irregularities in the response of the individual detector elements. This is done by presenting a black body at uniform temperature to the detector (typically a flat plate of high emissivity) held immediately in front of the lens. This NUC is applied directly at the analogue to digital conversion stage in the camera unit and a copy of the 'digitiser' settings is stored as two files in the PC, one for each array.

Erroneous measurements can occur due to an effect known as the Narcissus effect when observing a surface with relatively 'high' reflectivity. In this case, particularly when using the G1 lens, the detector can see its own reflection, which results in a systematic thermal gradient superimposed on the measured thermal data. It has been found that the NUC can be used to correct for this effect by performing the NUC using the surface to be studied in place of the black body, thereby counteracting the systematic thermal gradient by introducing an inverse gradient during the analogue to digital conversion. Since TSA deals with the temperature change rather than the absolute temperature, this correction only becomes important when motion is apparent.

4.3 TSA processing

The routine used by the Cedip system for processing the DL thermal data into ΔDL TSA data is not disclosed by the manufacturer. As with previous systems such as the DeltaTherm and the SPATE systems a lock-in amplifier is used as a band pass filter to keep only that component of the signal which occurs at the loading frequency and thereby reduce the noise content. The reference signal used for the lock-in amplifier (typically obtained from the test machine load cell signal generator) is input by one of three analogue ± 5 V input channels on the camera unit, converted to a digital signal and stored together with the thermal data for each frame.

A fast Fourier transform is used in conjunction with the reference signal to obtain the magnitude (i.e. the ΔDL TSA data) and phase angle of the DL output with respect to the reference signal. The average DL value over the whole time series is also measured. All the processing is done for each pixel / detector element individually.

To convert the ΔDL value into ΔT measurements, the system first correlates the average DL value to a temperature using the calibration curve, and subsequently uses the local gradient of the curve at that particular temperature to convert from ΔDL to ΔT as depicted schematically in Figure 4.2. This is necessary to compensate for the change in sensitivity of the detector as the temperature of the measured surface changes. One of the shortcomings of the system is that the calibration curves are sampled every ten degrees with a linear fit between sampling points and hence the gradient used to calculate the ΔT value changes abruptly either side of the sampling points. Hence, if the surface temperature of the specimen is close to such a point, surface points whose average temperatures lie either side of the change in gradient will be multiplied by a significantly

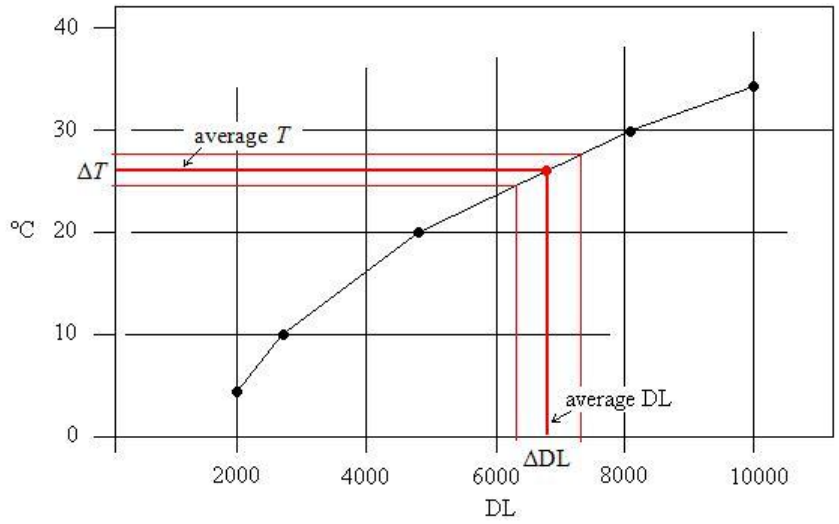

Figure 4.2: Schematic representation of the ΔDL to ΔT calibration process

different calibration constant. The consequence of this is shown in Figure 4.3 which shows the change in the thermoelastic response of a temperature controlled aluminium cylinder under a constant amplitude cyclic stress. A reduction in the measured ΔT value occurs every time the surface temperature crosses a sampling temperature.

One solution is to sample the calibration file more finely so that the changes in gradient between sampling points are small. The alternative is to ensure that the temperature of the surface being studied lies well away from the calibration temperatures. These are at 5, 10, 20, 30 and 40°C for the calibration used in this work. Since the surface temperature of test specimens typically only varies by $\pm$0.5°C, temperature ranges from 11 to 19°C and 21 to 29°C should provide adequate range. Difficulties may arise as specimens damage and localised increases in temperature occur. Here it may be more appropriate to use uncalibrated DL units and correct for the temperature change as described in [110].

If the material thermoelastic constant is known, the system is able to output the stress field directly. In this case, the phase angle is used to distinguish between compression and tension. Due to the characteristics of the load machine, the response of the load cell (or other source of the reference signal) and IR detector, there is typically a constant phase offset between the thermal signal and the reference signal. In contrast to other TSA systems, the exact phase offset is not tuned in at the start of a measurement. Instead an approximate phase difference is set to the nearest 90° so that a known region of tension in the specimen correlates to a positive stress measurement. Since under adiabatic conditions the phase difference will only be either 0° or 180° it is sufficient to place the phase offset in the correct quadrant in order to distinguish between tension and compression. However, under non-adiabatic conditions more precise phase tuning may be necessary. Such processing must be done independently of the Cedip system. Data can be exported in a suitable format for further manipulation in, for example, Matlab. In the current software there is an error which causes a constant time offset between the

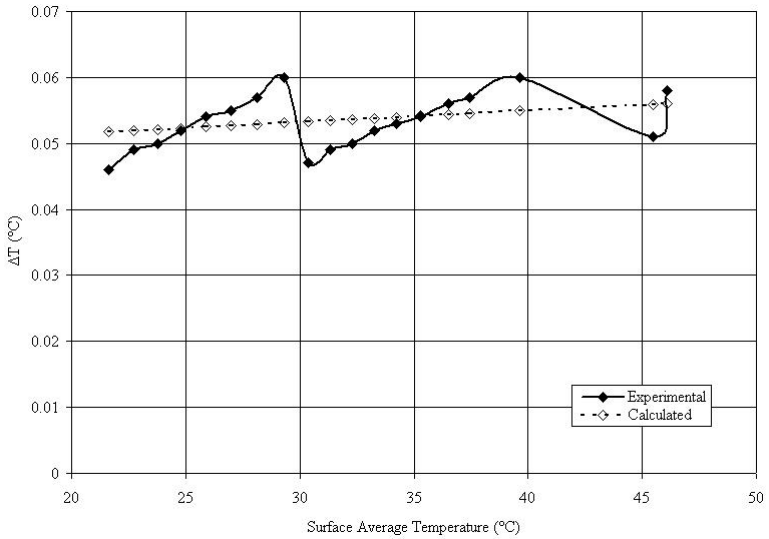

Figure 4.3: Change in thermoelastic response with increase in surface temperature of specimen - experiment versus theory

DL and the reference signals. This has the effect that the phase offset varies with the loading frequency. Hence, when evaluating the phase data, the absolute values of the phase data are not comparable between data sets taken at different loading frequencies. These therefore need to be normalised externally to the Cedip system.

4.4 Motion compensation

As a material is loaded it undergoes a strain. This means that motion will be present in any dynamically loaded specimen. Motion is particularly noticeable at specimen edges [112], but can also have a significant effect where there are surface irregularities that cause variations in the surface emissivity or at sharp stress gradients. The effect of motion will only be apparent if the magnification of the optical system is sufficiently large to resolve the motion. In the current work this means that motion only needs to be considered when using the G1 lens.

The primary need for motion compensation in the current work results from small irregularities on the surface of the specimen, which cause variations in the emissivity. These surface features are typically fractions of a millimetre across and therefore only become apparent when using the high resolution G1 lens, which gives a pixel resolution of 0.026 to 0.029 mm, depending on the focal setting of the underlying 27 mm optics. The change in emissivity produces a change in the measured temperature and gives a spread of 0.1 to 0.5°C, as can be seen in Figure 4.4. This is large in comparison to the thermoelastic temperature change, which is of the order of 0.1°C. Hence, the effect of motion is to completely obscure the thermoelastic temperature change.

The Cedip system includes motion compensation software that is able to deal with translation, rotation, deformation and combinations thereof. The software works by

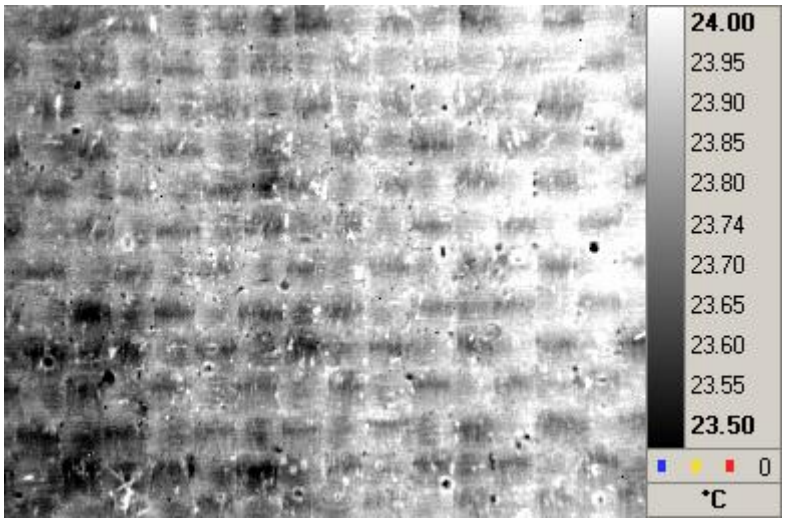

Figure 4.4: IR image of the surface of a typical specimen showing the peel ply imprint and other surface irregularities

means of pattern recognition and requires two operations. Two 'features' with strong contrast are identified by the operator on the surface of the component in the first thermal image of a video recording. These can be small defects or marks made by the user (e.g. pencil marks). The two features are joined by a vector that is defined by the two coordinate points in the first image of the video.

The first processing step is termed 'vector tracking'. The software recognises the features and searches for the same features in all subsequent images. The vector end points are relocated to follow the features. It is important to note that the endpoints of the vector are independent of each other so that all forms of distortion can be accounted for. In the second step the displacement, rotation and distortion of the vector is calculated from frame to frame, and each image is moved and distorted accordingly so that in the video data the moving component appears stationary.

The quality of the motion compensation is dependent on the sharpness of the contrast of the selected features and the size of the motion. Noise can be introduced into the image due to the need to interpolate sub-pixel motion and it should be noted that in applying the motion compensation, noisy data will become more noisy. It is therefore essential that the thermoelastic response is large compared with the noise threshold of the detector.

The following two examples demonstrate the effect of motion on thermoelastic data. Figure 4.5 shows the cross-section of a glass/epoxy laminate. The laminate consists of two single layers of woven roving on the surface, separated from three layers of woven roving in the centre by two layers of chopped strand matt. In the first image of Figure 4.5 a loose fibre can be seen protruding from the side of the specimen. In the non-motion compensated TSA data (second image) this filament appears twice as two regions of high thermoelastic response. From this second image it is possible to ascertain how far the specimen moves between the top of the loading cycle (i.e. as the specimen is fixed at

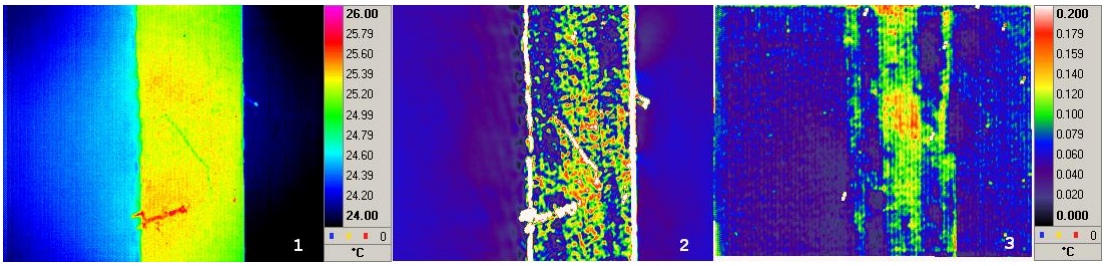

Figure 4.5: IR image of the cross-section of a laminate (1) and corresponding TSA data, with out (2) and with (3) motion compensation applied.

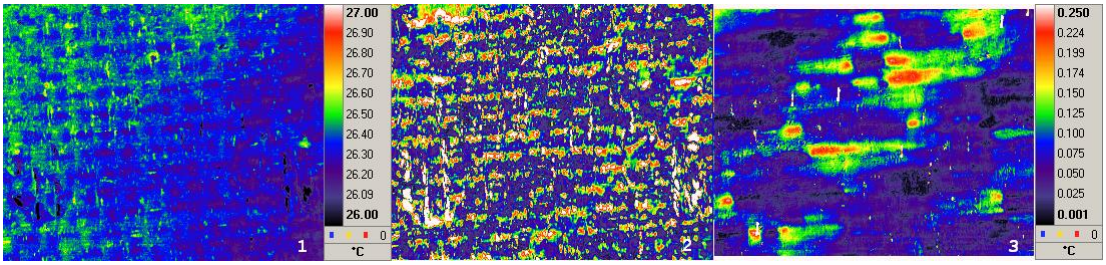

Figure 4.6: Front view of a woven composite (1) and corresponding TSA data, with out (2) and with (3) motion compensation applied.

the top this corresponds to the minimum load) and the bottom of the loading cycle. The detector is actually measuring the temperature difference between the fibre and the background as the fibre moves against the background. The third image shows the motion compensated TSA data. The protruding fibre has disappeared from the data as have the bright regions along the specimen edge. Instead, it is possible to identify approximately the individual plies in the laminate. Note that the Narcissus effect, seen in the raw IR data in image 1, is not apparent in the TSA data because it is a differential measurement and the background effect represents a constant offset.

Figure 4.6 shows the surface of a single ply of 2 x 2 twill woven glass / epoxy. The imprint of the peel ply used in manufacturing the specimen can be seen in the IR image (first image) as well as other features resulting from the surface roughness that cause slight variations in the emissivity. The motion of the specimen is of the same order as in the previous example and the result is that the thermoelastic temperature change is completely masked by the motion in the non-motion compensated TSA data shown in the second image. Compensating for the noise in the recorded data and repeating the analysis reveals a strong effect of the weave pattern on the thermoelastic response from this type of material.

Hence it can be seen that the motion compensation process as used in this work is able to remove edge type effects (as shown in the first example) and compensate for local variations in the surface emissivity (as shown in the second example) simply by removing the motion from the IR data.

4.5 Summary

The Cedip system provides two important facets that distinguish it from previous full field TSA systems. The first is the motion compensation routine. This is indispensable for obtaining data at high resolution and has been made use of extensively in the work studying the behaviour of woven materials in Chapters 5 and 6. The second feature is that the system is also able to provide thermal images and video data. This enables raw data to be captured and processed in a variety of ways. This feature has been used to study components under transient loads.

A third feature of the system is the radiometric calibration. This enables direct values ΔT to be obtained, simplifying the acquisition of quantitative data. In addition to the ΔT measurement, the detector also outputs an image of the mean surface temperature allowing localised heating to be identified, and the effect quantified immediately. The Cedip system therefore provides an ideal platform for the work described in this thesis.

Chapter 5

TSA of Woven Materials

5.1 Introduction

Since TSA is a surface sensing technique, it is the orientation of the surface fibres that will determine the thermoelastic response. For a woven material, the surface fibres alternate between two orthogonal orientations. Following the mosaic model of Ishikawa and Chou [21], the surface of the composite can be divided into a patchwork of cells, each responding as a UD composite. The thermoelastic response from the woven composite can then be considered in terms of the response from individual UD cells, each with a local material orientation relative to a global strain field. The work in this chapter investigates the thermoelastic response from woven composites under uniaxial tensile loading. The load has been applied parallel to the warp yarns, and hence the cells in the model are referred to as longitudinal cells (i.e. parallel to the loading direction) and transverse cells (i.e. at right angles to the loading direction). The corresponding coordinate axes are labelled L and T (global coordinates of the strain field) and 1 and 2 (local material coordinates) as shown in Figure 5.1. The red cells are longitudinal cells (1 is parallel to L and 2 is parallel to T) and the blue cells are transverse cells (1 is parallel to T and 2 is parallel to L). In using this model, a number of assumptions are made.

1. A uniform strain field is assumed, such that the global specimen strains can be applied locally to individual cells.

2. The weave must be balanced so that an in-plane load does not produce extension / bend coupling of the laminate.

3. Where the fibres bend away from the surface to cross under a transverse tow, a significant out-of-plane component is introduced into the strain field [113]. For the mosaic model to apply, this region of high crimp at the ends of each cell must be small compared with the length of the cell so that the majority of the cell can be assumed to be under plane-stress conditions.

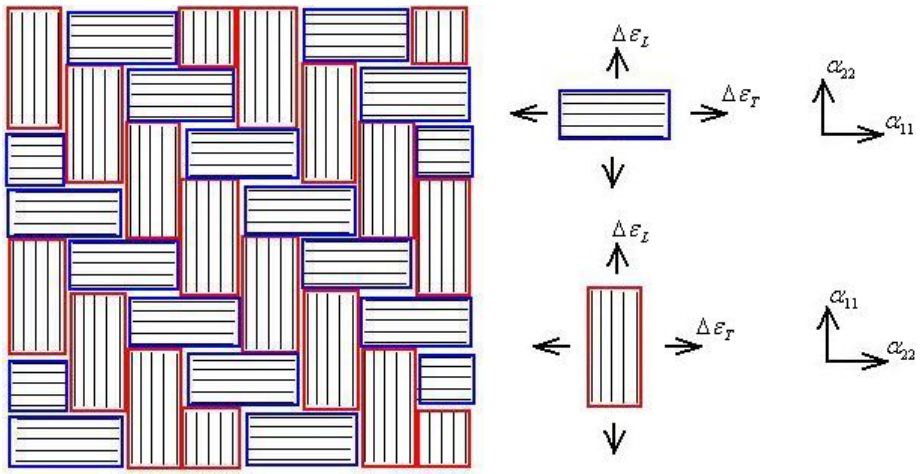

Figure 5.1: Mosaic model of a 2 x 2 twill woven composite

4. The thickness of the tows must be sufficiently large so that any heat transfer effects at the subsurface interface between warp and weft tows do not influence the thermoelastic response on the surface. This may alternatively be interpreted as a limitation on the minimum loading frequency to achieve adiabatic conditions at the surface.

The chapter starts out by defining the test specimens in section 5.2. These include a set of specimens to obtain the material properties required to predict the thermoelastic response. The material properties are crucial to obtaining accurate predictions of the thermoelastic response. In many cases in the literature, generic values have been taken from other sources. It is shown in section 5.3 that this type of approach can produce misleading results. The exact loading conditions for the test are described in section 5.4, allowing a prediction of the thermoelastic response to be made. Predictions from a 3D FE model are also included which take into account the non-uniformity of the strain field. In section 5.5, the results from the experimental work are presented, including first, data obtained using the standard 27 mm lens and secondly, data from the high resolution G1 lens. These are then discussed in relation to the predictions in section 5.6. The chapter ends with a summary of the conclusions in section 5.7.

5.2 Test specimens

Three types of woven glass fibre reinforced epoxy specimens are used in this work to verify the model predictions, and two uni-directional specimens are used for obtaining the material properties. The first two specimen types were manufactured from single plies of woven roving textile: one plain weave (specimen X1) and one 2 x 2 twill (specimen X2). In these specimens the weave is not constrained by any additional plies so that any stress concentrations are purely due to the weave geometry. Being balanced and symmetric, the plain weave specimen represents the simplest possible woven composite material. The 2 x 2 twill introduces a degree of complexity due to the asymmetry of

the weave. A third specimen type (specimen X3) consists of a mixture of 2 x 2 twill woven roving plies on the surfaces, separated from three central plies of 2 x 2 twill woven roving by two chopped strand mat (CSM) layers. The combination with CSM was intended to isolate the surface plies from the effects of stacking woven fabrics, in particular yarn nesting, while the underlying plies still serve to constrain out-of-plane deformations, thereby better approximating the model. Two 'calibration' specimens were manufactured with the fibres orientated at 0° (specimen X4) and 90° (specimen X5) to the loading direction. These were made from the weft fibres of the twill material. The purpose of these specimens was to provide representative measured values of the elastic constants (E_1, E_2, ν_{12} and ν_{21}), coefficient of thermal expansion (α_1 and α_2) and specific heat capacity (C_p) of the longitudinal and transverse cells for the exact material combination used. These specimens are also used to obtain an 'ideal' response to compare with the response obtained from the longitudinal and transverse cells of specimens X1 - X3, thereby enabling the validity of the simple patchwork approach to be assessed. The materials are shown schematically in Figure 5.2.

The laminated materials for the test specimens were produced in-house by manufacturing flat plates using a vacuum assisted resin infusion process, as described in section 2.2. In all cases the resin used was Prime 20 LV epoxy with a fast hardener from Gurit. Two surface finishes are produced by this process. On the mould side a 'smooth' finish is produced with the resin filling any unevenness of the reinforcing fibres. The thickness of this surface resin layer is irregular; in the current work this varied between 0 μm at the centre of a cell, and 100 μm at the resin pockets between cells. The range of the variation in thickness was dependent on the coarseness of the weave of the two textiles. The smooth surface also produces reflections which impair the TSA; to minimise these, the smooth surface was lightly abraided using 3M Scotchbrite. On the opposite side to the mould a layer of peel ply was used in the manufacturing process to allow excess resin to flow out of the fibre stack evenly during the infusion process. This produces a 'rough' surface with a thin uniform resin layer that follows the contours of the fibres below. The use of the peel ply reduces the surface reflections in the IR image, but introduces a small systematic pattern due to the surface imprint it leaves behind, which influences the measured thermoelastic data.

The panels produced by the infusion were cut into tensile test specimens of the type shown in Figure 5.2. Strips of material approximately 26 mm wide were cut and metal end tabs were bonded to both ends. The inserts in Figure 5.2 show the weave pattern and lay-up of the 5 types of specimen used. The fibre tows of the plain weave (specimen X1) were approximately 1 mm wide and 0.15 mm thick; the warp fibres were separated by gaps of 0.2 mm and the weft fibres by gaps of 0.8 mm. Hence the longitudinal cells were approximately 2.6 mm long by 1 mm wide and the transverse cells 1.4 mm long by 1 mm wide. The fibre tows in the twill weave (specimen X2) were approximately 2 mm wide and approximately 0.25 mm thick; the weave was very dense so that the gap between fibre tows could not be measured. This gave longitudinal and transverse

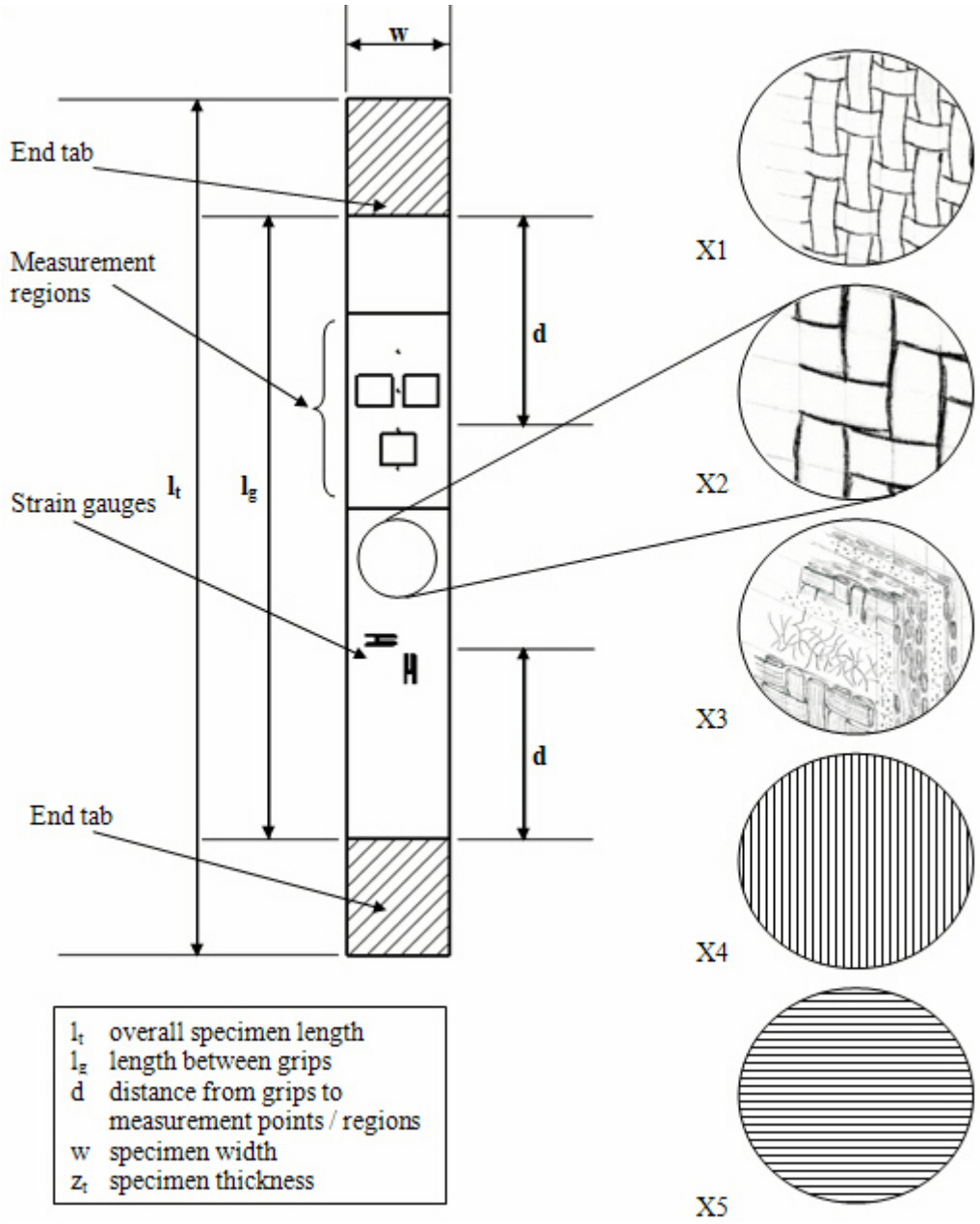

Figure 5.2: Specimen design and weave / lay-up types used in this chapter

cells of the same dimensions, i.e. 4 mm long by 2 mm wide. The stacking sequence of the laminate (specimen X3) was $[WR_1, CSM_2, WR_{1.5}]_S$, where WR refers to the twill weave fabric (woven roving) and CSM refers to the chopped strand mat. This produced a laminate 3.6 mm thick. The UD specimens were produced from 10 layers of fibre tows from the twill weave fabric, which produced a laminate approximately 1.7 mm thick. The exact dimensions of the five specimens used in the TSA are listed in Table 5.1.

Table 5.1: Specimen dimensions

	l_t (mm)	l_g (mm)	w (mm)	z_t (mm)	d (mm)
Specimen X1	314	255	26.5	0.30	75
Specimen X2	295	235	26.0	0.52	65
Specimen X3	375	275	40.0	3.60	95
Specimen X4	210	160	26.7	1.67	50
Specimen X5	210	160	25.6	1.85	50

After the specimens had been prepared a region 50 mm long was marked for study by TSA on one half of the specimen (see Figure 5.2). Within this region, three sub-regions were defined for detailed study with the G1 lens. An orthogonal two gauge strain rosette was bonded to each specimen to quantify the average strain sum applied to the specimens during testing, as shown in Figure 5.2. The strain gauges had a gauge length of 5 mm (to ensure that they crossed more than one cell) and a resistance of 120 Ω.

5.3 Study of the material properties

5.3.1 Thermoelastic response

In the proposed methodology the test specimens were subjected to a uni-axial tensile load. It was assumed that the strain field was uniform throughout the specimen and therefore equation 3.4 could be applied using the measured strains from the strain gauges directly. Since the warp and weft tows of the woven textiles were of the same type, the material properties of the longitudinal and transverse cells were also the same. Hence only the orientation of the fibres varied from cell to cell. Substituting the appropriate values of θ (0° for the longitudinal and 90° for the transverse cells) in equation 3.4 results in the following two expressions:

$$\Delta T_L = \frac{-T}{\rho C_p}\left[\left(\alpha_1 Q_{11} + \alpha_2 Q_{12}\right)\Delta\varepsilon_L + \left(\alpha_1 Q_{12} + \alpha_2 Q_{22}\right)\Delta\varepsilon_T\right] \tag{5.1}$$

$$\Delta T_T = \frac{-T}{\rho C_p}\left[\left(\alpha_1 Q_{11} + \alpha_2 Q_{12}\right)\Delta\varepsilon_T + \left(\alpha_1 Q_{12} + \alpha_2 Q_{22}\right)\Delta\varepsilon_L\right] \tag{5.2}$$

where ΔT_L and ΔT_T are the temperature change in the longitudinal and transverse cells respectively.

The warp and weft fibres in the plain weave composite were separated by a small gap that was filled with resin, and in both weaves at the cell boundaries, small resin rich

pockets were formed. A third equation can be written to describe the response of these isotropic resin interspersions [96]:

$$\Delta T = \frac{-T}{\rho_r C_{pr}} \frac{\alpha_r E_r}{1-\nu_r} \left[\Delta\varepsilon_T + \Delta\varepsilon_L\right] \tag{5.3}$$

where the subscript r refers to a property of the resin. The elements on the right hand side of equations 5.1, 5.2 and 5.3 can be split into two types: variables that describe the test conditions (T, $\Delta\varepsilon_L$ and $\Delta\varepsilon_T$) and constants that refer to the material properties (ρ, C_p, etc.). The purpose of the above equations was to predict the thermoelastic response from the longitudinal and transverse cells and the resin interspersions for any given test conditions to provide a basis for the interpretation of the measured data. It is clear that for this purpose a complete and accurate set of material properties is required. These were obtained by three methods:

1. calculation of the composite properties based on the constituent material properties obtained from literature sources and the manufacturer,
2. literature sources quoting material properties for UD E-glass / epoxy composite,
3. measured values obtained from specimens X4 and X5.

The three methods are described in the following section.

5.3.2 Determination of material properties

Method 1

It is known that a large variability exists in the properties of composite materials. Assuming that the same resin system and fibre type are used, this variability is related primarily to the fibre volume fraction (V_f). Varying the fibre volume fraction, it is possible to obtain a spread of realistic combinations of composite material properties for predicting the thermoelastic response from the two cell orientations.

The derivation of the mechanical properties from the constituent properties and the fibre volume fraction is well documented (for instance in [114]). Accordingly, the Young's moduli (E_1 and E_2) can be obtained from:

$$E_1 = E_f V_f + E_r \left(1 - V_f\right) \tag{5.4}$$

and

$$E_2 = \frac{E_f E_r}{E_r V_f + E_f \left(1 - V_f\right)} \tag{5.5}$$

where the subscripts f and r denote the properties of the fibre and the resin respectively. Equation 5.5 is known to under predict the value of E_2, particularly for higher fibre volume fractions, and it has been suggested in reference [114] to use a correction factor of the form $E'_r = \frac{E_r}{1-\nu_r^2}$.

The major Poisson's ratio ν_{12} can be obtained from:

$$\nu_{12} = \nu_f V_f + \nu_r (1 - V_f) \tag{5.6}$$

and the minor Poisson's ratio ν_{21} is given by:

$$\nu_{21} = \frac{\nu_{12} E_2}{E_1} \tag{5.7}$$

The Schapery equations [88, 115] can be used to obtain the CTE in the longitudinal and transverse directions:

$$\alpha_1 = \frac{\alpha_f E_f V_f + \alpha_r E_r (1 - V_f)}{E_f V_f + E_r (1 - V_f)} \tag{5.8}$$

and

$$\alpha_2 = \alpha_f (1 - \nu_f) V_f + \alpha_r (1 - \nu_f)(1 - V_f) - \alpha_1 \nu_{12} \tag{5.9}$$

The density and specific heat capacity can be obtained by the rule of mixtures:

$$\rho = \rho_f V_f + \rho_r (1 - V_f) \tag{5.10}$$

and

$$C_p = C_{pf} V_f + C_{pr} (1 - V_f) \tag{5.11}$$

The above equations for determining the Young's moduli, Poisson's ratios and CTEs assume that both the matrix and the fibres are isotropic. This is true for both epoxy resins and glass fibres. Hence a complete set of material properties as contained in equations 5.1 and 5.2 can be calculated for any combination of constituent properties and fibre volume fractions.

The constituent material properties of the composite used in this work were obtained from the manufacturer [116, 117] in the case of the resin (except C_p which was not available from the manufacturer and was therefore measured in-house) and from [118] for the fibre. The values are listed in Table 5.2. How the resulting composite material properties vary with the fibre volume fraction is shown graphically by the solid and dashed lines in Figures 5.3 and 5.4 for the Young's moduli and the CTE's respectively. The points on the graphs were obtained by methods 2 and 3 described in the following sections. The difference between E_1 and E_2 increases with V_f to a maximum at approximately 80%. By contrast, the difference between α_1 and α_2 has a maximum at around a V_f of 20%. At a typical fibre volume fraction of 50 to 60% for a UD FRP, the ratio between the Young's moduli and the CTEs is approximately the same, with a factor of six between the two orientations. For comparison with methods 2 and 3, a V_f of 55% has been used. The values obtained using method 1 are listed as 'Theory' in Table 5.3. E_2 and ν_{21} have been calculated using equation 5.5 with and without the corrected resin stiffness E_r'.

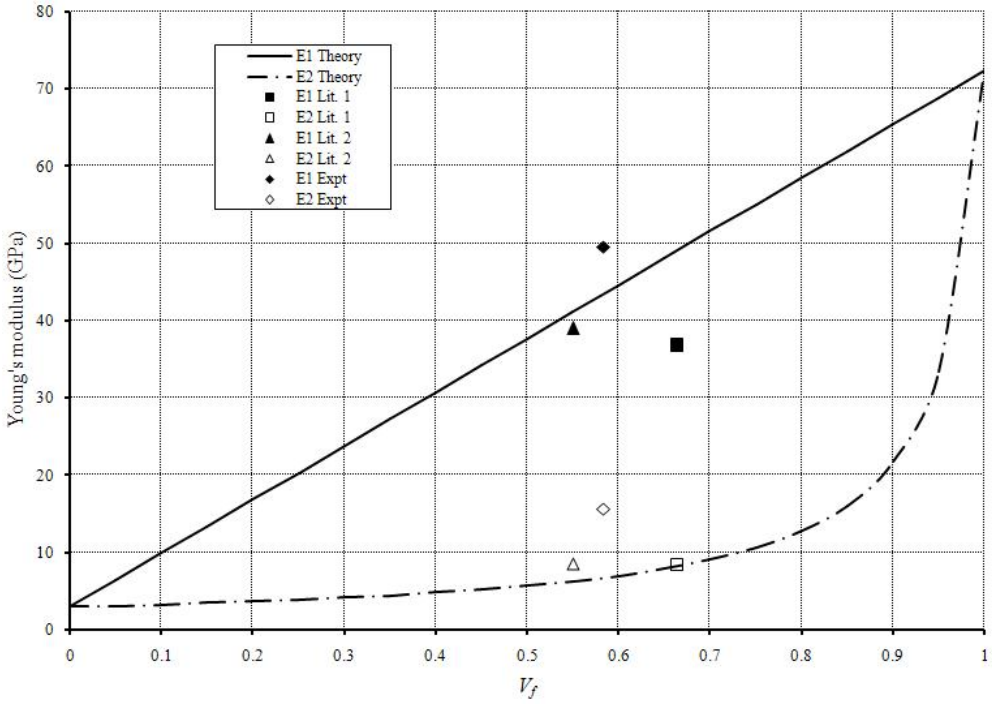

Figure 5.3: Variation of the Young's modulus with V_f

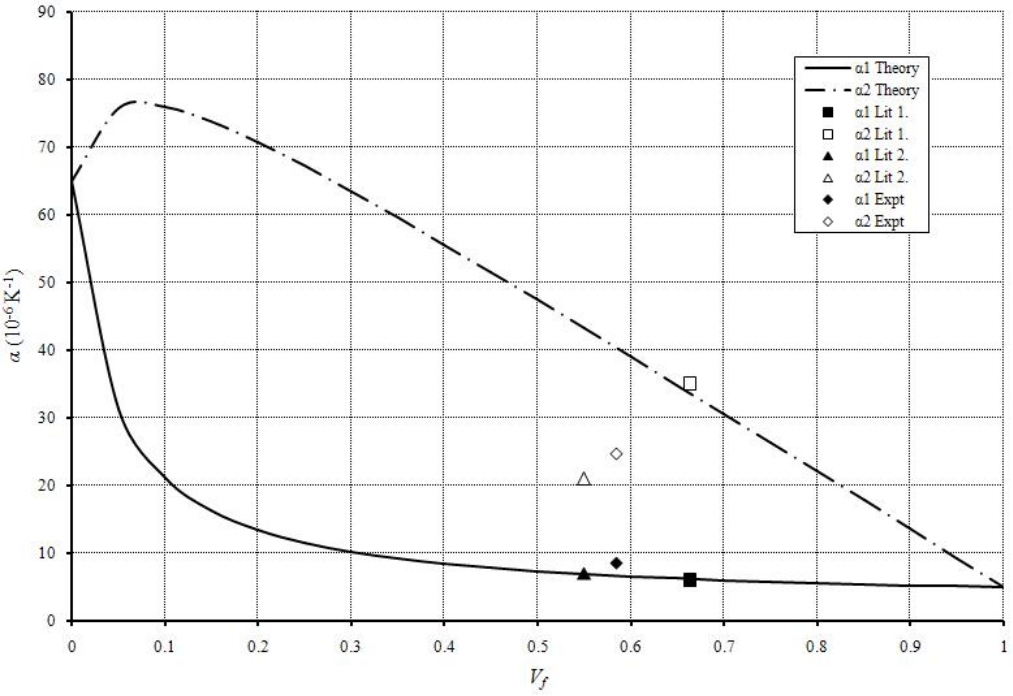

Figure 5.4: Variation of the CTE with V_f

Table 5.2: Constituent material properties

	Density (kg m^{-3})	Specific Heat Capacity (J $kg^{-1}K^{-1}$)	Young's Modulus (GPa)	Poisson's Ratio	CTE ($\times 10^{-6}$ K^{-1})
Fibre	2570 [118]	810 [118]	72.4 [118]	0.20 [118]	5 [118]
Resin	1153 [116]	1225 *	2.97 [117]	0.44 [117]	65 [117]

* Obtained experimentally

Table 5.3: Composite material properties

	V_f (%)	ρ (kg m^{-3})	C_p (J kg^{-1} K^{-1})	E_1 (GPa)	E_2 (GPa)	ν_{12}	ν_{21}	α_1 ($\times 10^{-6}$ K^{-1})	α_2 ($\times 10^{-6}$ K^{-1})
Theory	55	1930	997	41.2	6.28 (7.71)*	0.308	0.047 (0.060)*	6.95	33.3
Lit. 1	66.4 [96]	2090**	951**	36.8 [96]	8.4 [96]	0.250 [96]	0.050 [96]	6.00 [15]	35.0 [15]
Lit. 2	55.0 [114]	2100 [114]	997**	39.0 [114]	8.6 [114]	0.280 [114]	0.060 [114]	7.00 [114]	21.0 [114]
Expt	58.4	1980**	828	49.6	15.7	0.285	0.107	8.54	24.8

* Calculated using the corrected value E_r'

** Calculated from the constituent material properties and the fibre volume fraction

Method 2

The first difficulty encountered was that no single literature source provided a complete set of all eight required material properties. Therefore three sources were combined to provide two complete sets. For the first set the mechanical properties were obtained from [96] and the CTE's were obtained from [15]. The set was supplemented with values of ρ and C_p calculated by method 1. The volume fraction was based on the material described in [96]. Since [15] does not quote either a volume fraction or a glass fibre type it is not known if the values from the two sources correspond.

The second set was obtained almost completely from [114]. Only the value of C_p had to be supplemented using method 1. The values are listed in Table 5.3 as 'Lit. 1' and 'Lit. 2'.

Method 3

Specimens X4, X5 and five smaller offcuts from the UD panel were used to measure the material properties of the composite used in this work. The fibre volume fraction was obtained using micrographs of the cross-section from 5 regions on the UD panel. An optical method was chosen in favour of burn-off tests so that the void content could be assessed. The density was calculated on the basis of the measured fibre volume fraction and method 1. The specific heat was measured using a calorimeter on small off-cuts (approximately 3 x 3 x 1.7 mm) from the UD panel over a temperature range from 20 to 40 °C. The Young's moduli and Poisson's ratios were obtained from quasi static tensile tests of specimens X4 and X5, over a strain range from 0 to 0.002. Strain data was obtained from the strain gauge rosette and the global stress in the laminate was calculated using data from the test machine load cell and the measured cross-sectional

area. Only one specimen of each X4 and X5 were tested due to difficulties in the manufacture of the UD material. The CTE's were obtained by heating the specimens from 20 to 40 °C and comparing the strain gauge output with that from a gauge mounted on a reference material of known CTE. The details of the method are described in [119]. The material properties are listed as 'Expt' in Table 5.3.

A variation of several percent in each property is to be expected and can be attributed to differences in the fibre volume fraction, the manufacturing process and conditions, the epoxy resin used, the fibre preparation and type (not specified in [15]) and measurement errors. However, E_2, ν_{21} and α_2 in Table 5.3, stand out as they vary over a large range, with standard deviations of 30 to 40%. In the case of E_2 and ν_{21} it is the measured data (Expt.) that stands out, a factor of two larger than the mean of the others. The large value of ν_{21} can be linked to the large value of E_2. It is noted that the measured values of both E_1 and E_2 are significantly higher than the theoretical values and those from the literature sources. The fact that the measured values exceed the calculated values is particularly remarkable since inevitably any real material will include manufacturing defects (e.g. voids, dry fibres, fibre misalignment) while the theory assumes zero defects. But, while the 20% larger than average value of E_1 might credibly be explained by variability resulting from the manufacturing technique, no satisfactory explanation has been found for E_2.

Some of the manufacturing anomalies include:

- To ensure good alignment of the fibres, the yarns extracted from the textile were spanned across a flat plate, with a small tensile load applied.
- The resin was infused at sub-optimal temperatures of 10 to 15°C (optimal being 20 to 25°C [117]) due to the uncontrolled laboratory environment.
- To raise the temperature during the cure, a tent was errected over the mould and the job was heated using a hot air blower. In this way a temperature of 20 to 25°C was achieved. However, the temperature of the job was found to vary significantly, and it is estimated that the temperature locally, near the hot air inlet, may have been as high as 50°C.

Pre-tensioning of the fibres was minimal. However, the fibres will not have been gripped evenly and this may therefore have lead to residual stresses within the cured composite. Local heating of the job during cure is another source of residual stress in the cured composite. This is however more likely to influence the failure stress than the stiffness.

The low temperature of the resin during the infusion means that the viscosity of the resin was high. This would be expected to lead to increased void content and reduced fibre wet-out within the yarns, lowering the stiffness, particularly in the transverse direction. However, the low void content (2.25%) and the high value of E_2 suggest that fibre wet-out was good.

The explanation for the exceptionally high transverse properties must therefore lie with the heating during the cure. Raising the temperature would lead to a very low viscosity for a resin system that has been optimised to have a low viscosity for infusion processing. The thin laminate and metal mould will have served to dissipate heat, thereby averting possible problems with the exothermic nature of the cure. The lowering of the viscosity after the infusion process was completed will have lead to a second period of consolidation during which entrapped gases could escape and intra-yarn fibre wet-out could have ocurred. This would help to explain the low void content. It is speculated that the raised temprature may have led to an improved fibre / matrix interfacial bond, or a larger area of influence of the fibre / matrix interfacial region due to CTE mismatch between the fibre and the resin and the associated residual stress at the micro-scale. However, the chemistry of the reaction and the bond are not well understood by the author and hence this explanation for the high value of E_2 is not considered well founded.

It is notable in the data that the larger variability in the material properties is in the transverse rather than the longitudinal direction. This suggests that these are either more difficult to predict or subject to greater variability or both. Particular care must therefore be taken when selecting the transverse material properties for making predictions of the thermoelastic response.

5.3.3 Parametric study

In equations 5.1 and 5.2 it is possible to identify three sets of material properties. The first, $\frac{1}{\rho C_p}$, influences the magnitude of the thermoelastic response of both longitudinal and transverse cells equally in a simple inverse proportionality. The second two, $(\alpha_1 Q_{11} + \alpha_2 Q_{12})$ and $(\alpha_1 Q_{12} + \alpha_2 Q_{22})$ influence the response from the two cell orientations differently since the strains $\Delta\varepsilon_L$ and $\Delta\varepsilon_T$ are not equal. Therefore, the relative magnitudes of the latter two terms determine the ratio between the response from the longitudinal and transverse cells. For the purpose of discussion the latter two terms will be referred to as A and B, such that:

$$A = \alpha_1 Q_{11} + \alpha_2 Q_{12} \tag{5.12}$$

$$B = \alpha_1 Q_{12} + \alpha_2 Q_{22} \tag{5.13}$$

If A and B are equal, then the thermoelastic response from both the longitudinal and transverse cells will be equal. If A is larger than B, then the response from the longitudinal cells will be larger than that from the transverse cells, and vice versa if B is larger than A. To determine which material properties dominate each of the two terms, equations 5.12 and 5.13 can be rewritten as shown below, and typical orders of magnitude can then be substituted for the material properties:

$$A = \frac{E_1}{1-\nu_{12}\nu_{21}}\left(\alpha_1 + \nu_{21}\alpha_2\right) = \frac{10^{10}}{1}\left(10^{-6} + 10^{-2}10^{-5}\right) \tag{5.14}$$

$$B = \frac{E_2}{1-\nu_{12}\nu_{21}}\left(\nu_{12}\alpha_1 + \alpha_2\right) = \frac{10^9}{1}\left(10^{-1}10^{-6} + 10^{-5}\right) \tag{5.15}$$

This simple investigation shows that A depends on E_1 and α_1 and is therefore dominated by the fibre properties, while B, dependent on E_2 and α_2, is dominated by the properties of the resin. In the previous discussion it was shown that the properties in the transverse (resin dominated) direction are more susceptible to variability and error. Using the standard deviation of each of the values in Table 5.3 as an indication of the variability expected in A and B gives:

$$s_A \approx S_{E_1} + S_{\alpha_1} \approx 28.20\% \tag{5.16}$$

$$s_B \approx S_{E_2} + S_{\alpha_2} \approx 71.85\% \tag{5.17}$$

where s is the variability and S is the standard deviation. For an E-glass / epoxy composite A and B are of similar order of magnitude; however they may be up to a factor of 2 different. Therefore the ratio between the thermoelastic response from the longitudinal and transverse cells is expected to lie somewhere between 1 and 2. Moreover, a discrepancy between the calculated and the measured values of ΔT is most likely to be due to an error in the transverse material properties.

For comparison, values of A and B calculated from the material properties in Table 5.3 have been plotted in Figure 5.5. The bold line $A = B$ highlights the transition between $\Delta T_L < \Delta T_T$ to $\Delta T_L > \Delta T_T$. Method 1 was used to obtain a spread of values of A and B for volume fractions from 0 to 1. These are plotted as the solid line 'Theory'. The values for a volume fraction of 55% have been plotted as solid squares and open squares, the latter obtained using the corrected value E_r'. The values calculated using Methods 2 and 3 are also plotted. Figure 5.5 shows that in general A is expected to be larger than B and hence also the thermoelastic response from a longitudinal cell will be larger than that from the transverse cell.

The large spread of material properties reflects the complexity of composite materials and demonstrates the need for experimental determination of the exact properties of any

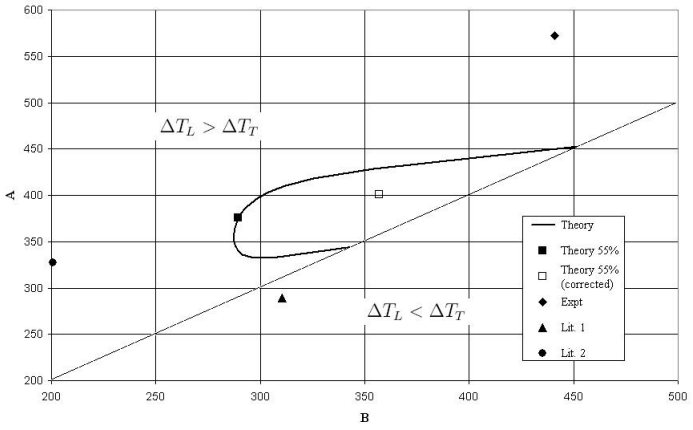

Figure 5.5: Variation of thermoelastic parameters A and B

particular combination of materials if quantitative measurements are required. In the following work it would be ideal to be able to cut samples of the individual cells from the woven material for determining the exact material properties. Unfortunately this is not a practical solution and therefore a comprise had to be made. In the current work this took the form of manufacturing 'calibration' specimens from an infused UD panel (X4 and X5) using fibre tows from the same textile as used for the woven composite specimens. The resulting material had an unexpectedly high stiffness, in particular in the transverse direction. This may be expected to result in an overprediction of both ΔT_L and ΔT_T.

5.4 Test setup

Five specimens (one of each type X1 to X5) were loaded in an Instron 8802 servo-hydraulic test machine. The specimens were loaded to a mean strain of 0.0014 in the longitudinal direction. For comparison purposes, a cyclic displacement was applied such that the strain sum ($\Delta\varepsilon_1 + \Delta\varepsilon_2$) was approximately 0.0016 for all specimens; Table 5.4 lists the exact values for each test.

Table 5.4: Test strains

Specimen	$\Delta\varepsilon_L$	$\Delta\varepsilon_T$	$\Delta\varepsilon_L + \Delta\varepsilon_T$	Mean Strain
X1	0.002026	-0.000437	0.001589	0.001406
X2	0.001822	-0.000236	0.001586	0.001483
X3	0.001949	-0.000337	0.001612	0.001139
X4	0.002312	-0.000665	0.001647	0.001355
X5	0.001777	-0.000170	0.001607	0.001436

In this work the specimens were not coated with a high emissivity paint and the emissivity of the material was unknown. A comparison between an unpainted specimen and a specimen coated with RS matt black paint (with an emissivity of 0.92) showed a practically identical temperature measurement. Since the measurement of temperature depends on the emissivity it was decided to use an emissivity of 0.92, i.e. that of the matt black paint.

Using the material properties in Table 5.3, the average of the test strains for specimens X1 to X3 in Table 5.4 and a temperature (T) of 295 K, equations 5.1, 5.2 and 5.3 were used to predict the thermoelastic response from the longitudinal and transverse cells and the resin interspersions. These are listed in Table 5.5. Because of the difference in the Poisson's ratio, the ratio of $\Delta\varepsilon_L$ to $\Delta\varepsilon_T$ for the UD specimens X4 and X5 was different from that imposed on the UD cells in the woven composite, as shown in Table 5.4. The corresponding response from specimens X4 and X5 was therefore also included in Table 5.5, using the experimentally derived material properties (Expt.). This shows that the predicted response from specimens X4 and X5 is very similar to that from the longitudinal and transverse cells in the woven material (calculated using Expt.).

Table 5.5: Predicted thermoelastic response (ΔT)

	Longitudinal	Transverse	Resin
Theory (55%)	0.098	0.068	-
Lit. 1	0.072	0.077	-
Lit. 2	0.084	0.039	-
Expt	0.172	0.122	-
X4, X5	0.177	0.127	0.117
FEA (yarn)	0.030	0.127	-
FEA (res.)	0.010	0.140	-

It is known that the local strain in the woven composite will differ from the global strain. Therefore, in addition to the patchwork model, a 3D unit cell FE model was created using the WiseTex software described in Chapter 2.5. The geometry was measured from the 2 x 2 twill textile used in specimen X2. The yarns were divided into 12 elements in the width, and 4 in the thickness. A small resin gap was introduced between the yarns and a surface resin layer thickness of 0.56 mm was added in order to produce a good quality mesh. The resin regions were meshed with two elements through the thickness. The mesh is shown in Figure 5.6, with the resin elements hidden for clarity. The resulting yarn fibre volume fraction was calculated as 69.6% and the corresponding material properties were calculated from the constituent properties. The model was then imported into Ansys using SOLID185 elements. Periodic boundary conditions were applied as described in [62]. The A strain of 0.001822 was applied in the warp direction to obtain the strain field (comparable to specimen X2, see Table 5.4) and the adiabatic temperature change was calculated from the element strains, taking into account the local material properties and fibre orientation. These have also been added to Table 5.5 as FEA (yarn) and FEA (res.) for the predicted response from the yarns and the resin surface layer respectively.

To provide a comparison with the experimental data, the predictions from the twill woven material X2 have also been represented graphically in Figure 5.7, imposed on the

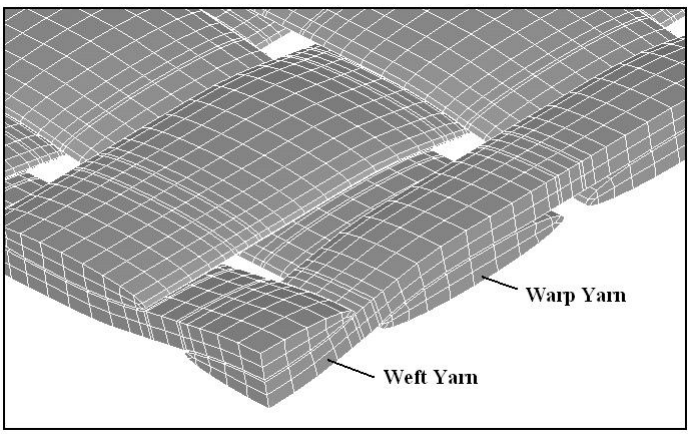

Figure 5.6: FE mesh of the yarns without resin

geometry used for the FEA model. The predictions using the material properties Lit. 2 and Expt. are shown in images 5.7(a) and 5.7(b), with the value for the pure resin used in the gaps between the yarns. Figure 5.7(c) shows the FEA model prediction for the resin surface layer. Removing the surface elements to reveal the response from the yarns below gives the image in Figure 5.7(d). It can be seen that the non-uniform strain field is expected to result in a higher thermoelastic response from the transverse rather than the longitudinal cells. It should also be noted that the thermoelastic response from the resin surface layer on the longitudinal cells is predicted to be 180° out of phase from the rest of the specimen in the central region of the cell, implying a net compressive strain in the surface resin layer. Note that the thickness of the surface resin layer in the FE model is exaggerated to produce a good FE mesh, and that bending due to out of plane deformation of the yarns under load will therefore also be exaggerated.

The predictions show that steep gradients are to be expected in the thermoelastic response from the woven composite. Therefore establishing a loading regime to achieve an adiabatic response was considered to be an essential first step. Specimen types X1, X2 and X3 were subjected to a strain change over a frequency range from 2 to 30 Hz. The phase data was used to indicate non-adiabatic conditions, as described in section 3.3. A frequency of 30 Hz was identified as being the most suitable as the data from specimens X2 and X3 showed a nearly uniform phase angle across the surface as of this loading frequency. The phase data from specimen X1 was not quite uniform at the cell boundaries, indicating some non-adiabatic response in the resin gap between the cells. At higher loading frequencies the desired strain change could not be achieved by the test machine, so a loading frequency of 30 Hz was considered acceptable for the current work.

5.5 Results

The discussion of the results is split into two sections, in each section, the data is described in detail before the interpretation. The findings using the 27 mm lens are discussed first in section 5.5.1, as these give an overview of the global thermoelastic behaviour of the specimens. The use of the G1 lens permitted closer study of how the thermoelastic response is linked to the geometry of the weave, and this is discussed subsequently in section 5.5.2. With the exception of specimen X3 it was possible in all cases to superimpose the position of longitudinal and transverse cells over the thermoelastic data from the G1 lens.

5.5.1 27 mm Data

Figure 5.8 shows data from specimens X1 to X3, taken using the 27 mm lens. Images a) and b) are of the plain weave (specimen X1), c) and d) are of the 2 x 2 twill weave (specimen X2) and e) and f) are of the mixed laminate (specimen X3) with a 2 x 2 twill woven ply on the surface. Images in the left column are from the rough surface, the

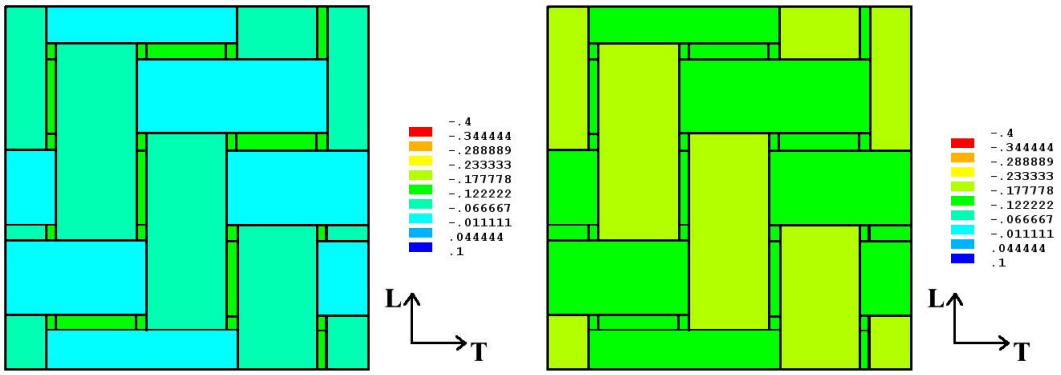

(a) Mosaic model (Expt.)

(b) Mosaic model (Lit.1)

(c) FE model: resin surface layer

(d) FE model: yarn response

Figure 5.7: Predicted thermoelastic response from a 2 x 2 twill woven composite

right column from the smooth. The anomaly in the upper left part of image b) is due to an inclusion from the manufacturing process.

An area of data, as indicated in Figure 5.2, was selected for each data set in such a way as to exclude the edges of the specimen and large anomalies in the stress field. Looking at the average thermoelastic response from each specimen, it is surprising to note that there is a general increase in the thermoelastic response from specimens X1 through to X3 despite the applied strain sum being the same for all cases. The data is spread across a range from 0.065°C for specimen X1, 0.089°C for specimen X2 to 0.128°C for specimen X3. This will be discussed in greater detail in light of the G1 data.

By examining the pattern in the thermoelastic response, although an influence of the weave pattern is distinctly present, most notable is the lack of a patchwork of cells with high and low response, as would be expected based on both the mosaic and FEA model predictions in section 5.4. In the plain weave, the response is very uniform across the whole of the specimen (0.04 to 0.07°C). Regions of increased response (approximately 0.10°C) form horizontal zig-zag lines across the specimen. At the resolution provided by the 27 mm optics, these regions are only a few pixels across. The data from specimen X2 shows very distinct diagonal bands. These alternate between uniform blue bands (0.05 to 0.07°C) and ones with blue squares, 'framed' on all sides by orange regions (0.13 to 0.17°C). The same weave pattern however produces a different stress pattern in specimen X3. Again, diagonal banding can be identified, but in this case the thermoelastic response is generally high (0.13 to 0.15°C) with rectangular regions of lower response (0.06 to 0.08°C).

In general the patterns are clearer in the data from the smooth side than the rough. The dither effect visible in this data can be attributed to the peel ply imprint which produces a structured surface roughness on the rough side. In the case of specimen X3 this almost completely masks any pattern in the data due to the weave.

Specimens X4 and X5 were also tested using TSA. Unfortunately only data from the rough side of specimen X5 could be obtained as the specimen broke in the grips during the first test series. Figure 5.9 shows the thermoelastic response from the rough sides of the longitudinal and transverse specimens. (The heat generated from the strain gauge on the smooth side is visible in the lower portion of both images in Figure 5.9.) While the response from the longitudinal specimen ($0.135 \pm 3\%$ on the smooth side, $0.122 \pm 9\%$ on the rough side) is very uniform with only some noise that is attributable to the surface roughness, the response from the transverse specimen ($0.124 \pm 16\%$) shows the fibre orientation clearly. Due to the manufacturing process, the thickness and fibre density varies more strongly transverse to the fibres than parallel to the fibres. Variations in the thickness of 0.1 mm make a difference of approximately 5 % in the cross-sectional area of the transverse specimen on the longitudinal specimen. This would account for the horizontal banding in the thermoelastic response from specimen X5 but not for the magnitude (16% see Table 5.6). However, variations in the thickness may combine locally with variations in the fibre volume fraction to cause the large variation observed

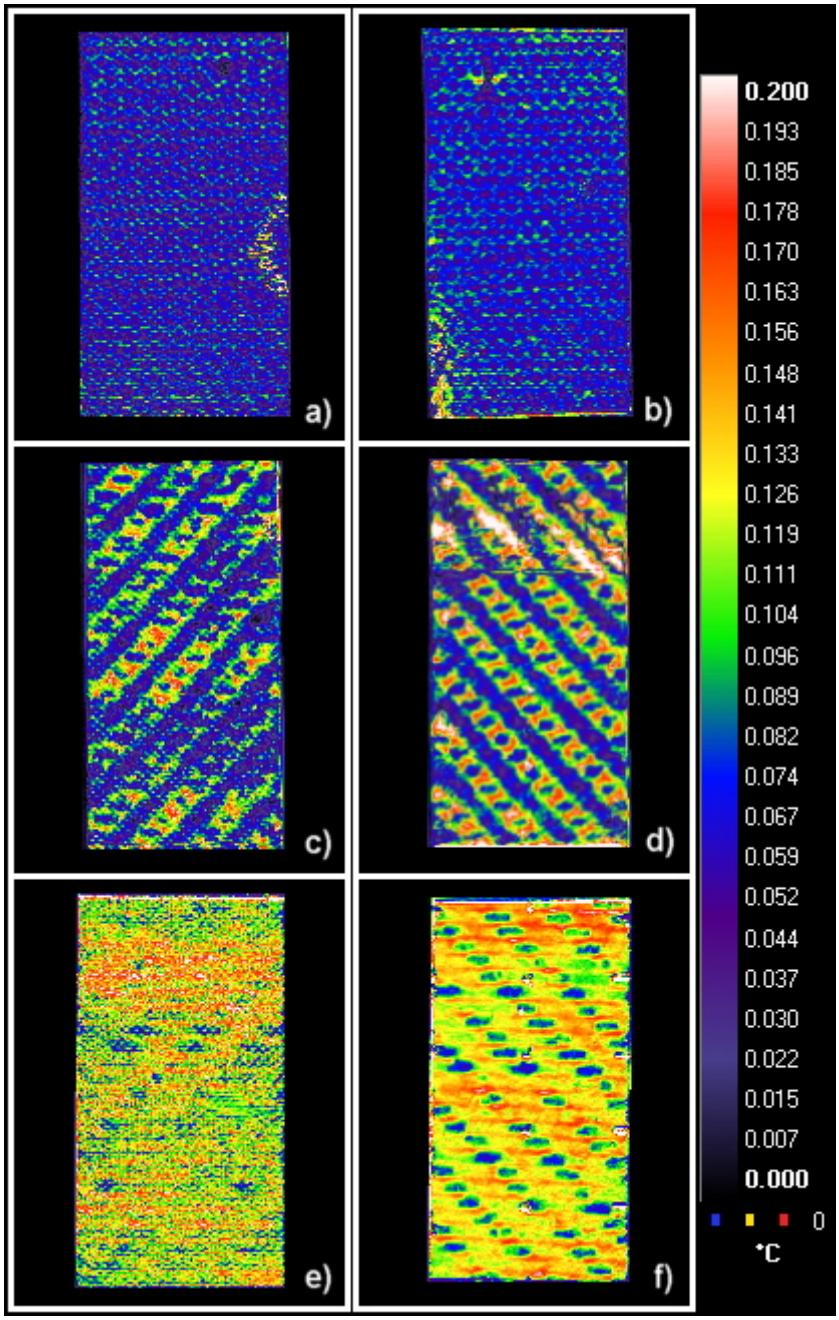

Figure 5.8: TSA data from specimens X1, a) and b) , X2, c) and d) and X3, e) and f). Images on the left are from the rough surface. Images on the right are from the smooth surface.

in the thermoelastic response.

The results from the transverse specimen lie very close to the prediction based on the measured material properties ('Expt') shown in Table 5.5. The results from the longitudinal specimen are very much lower than the predictions. However, both the results lie close to the predicted response from the resin. This points very strongly to the resin acting as a strain witness which corresponds with observations made in [96]. Based on the results from specimen X4, this strain witness behaviour is true of the surface resin layer on both the rough and the smooth surfaces.

5.5.2 G1 data

Measurements of ΔT from the longitudinal and transverse cells and the cell boundaries were obtained from two locations in each of the three sub-regions (see Figure 5.2) and the values quoted in Table 5.6 are averages obtained from the six data sets. The data from the single ply specimens X1 and X2 will be considered first.

Table 5.6: Measured thermoelastic response

Specimen	ΔT (C) (± % variation)					
	Rough			Smooth		
	Long	Trans	Boundary	Long	Trans	Boundary
X1	0.047 (30)	0.064 (20)	0.101 (14)	0.060 (23)	0.072 (17)	0.115 (15)
X2	0.056 (38)	0.070 (49)	0.144 (31)	0.071 (31)	0.067 (31)	0.158 (21)
X3	*	*	*	0.139 (14)	0.073 (29)	0.165 (15)
X4	0.122 (9)	-	-	0.135 (3)	-	-
X5	-	0.124 (16)	-	-	**	-

* Longitudinal and transverse cells could not be identified.

** Specimen broke in the grips during test.

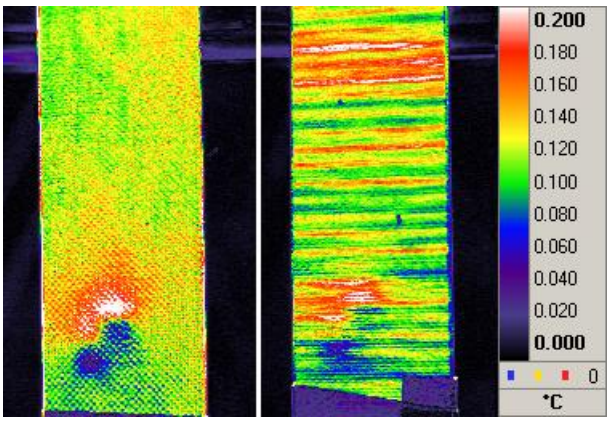

Figure 5.9: TSA data from specimens X4 (left) and X5 (right)

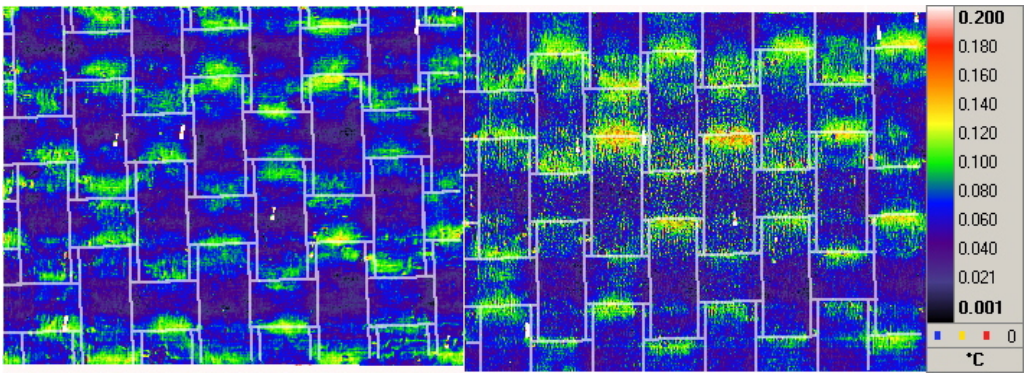

Figure 5.10: TSA data from Specimen X1, sub-region 3, (left) rough side, (right) smooth side. The weave pattern is overlaid.

It was possible in both cases (specimens X1 and X2) to overlay the weave pattern onto the TSA data. In the case of the plain weave specimen this was done by correlating the known geometry of the weave to the patterns in the TSA data. The weave pattern for this material is overlaid on the thermoelastic images shown in Figure 5.10. It is clear that at the cell boundaries above and below the cells the thermoelastic response is consistently larger than that from the central region of the cell. This increase in thermoelastic response is not noted at the lateral cell boundaries. At all cell boundaries there are resin rich pockets which could explain the increased signal by virtue of the larger thermoelastic response of the resin compared with the composite. At the lateral boundaries the resin rich pockets occur due to the gaps in the weave, as described in section 5.2 whilst at the upper and lower boundaries the resin rich pockets arise due to the crimp in the fibres as the tows bend to cross under the transverse running weave. Particularly in the longitudinal running fibres the out-of-plane deformation due to the crimp would be expected to produce an additional tensile strain which would contribute towards an increased thermoelastic response. Since this out-of-plane deformation is not present at the lateral boundaries, it is likely that the increase in response is due to the crimp, and hence a strain related effect, rather than the resin rich pockets, and a material heterogeneity related effect.

The thermoelastic response from the longitudinal and transverse cells is approximately equal, (corresponding to the prediction using material properties (Lit.1)). However, based on the data from specimens X4 and X5, this might point towards the response coming from a surface resin layer acting as a strain witness. In this case the above argument used to explain the increased thermoelastic response at the cell boundaries would still apply as the out-of-plane strain due to the fibre crimp would be transmitted into the surface resin layer and influence the thermoelastic response locally, as shown in the FEA predictions in Figure 5.7(c). However, it can be seen from the results summarised in Table 5.6 that the response is much lower than the 0.117°C predicted using the resin properties.

The high resolution data for the twill weave (specimen X2) is shown in Figure 5.11,

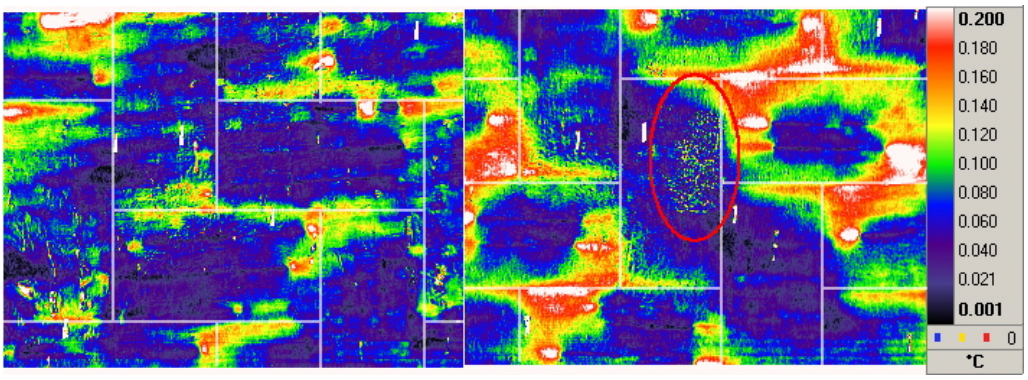

Figure 5.11: TSA data from Specimen X2, sub-region 3, (left) rough side, (right) smooth side. The weave pattern is overlaid.

again for both surface finishes and with the weave pattern overlaid. The correlation with the weave pattern is less obvious than for the plain weave specimen. However, it was possible to identify a longitudinal fibre by visual inspection. This was marked on the specimen (indicated by the red ellipse in Figure 5.11) and enabled the weave pattern to be overlaid correctly. Similar to specimen X1 there is a higher thermoelastic response at the cell boundaries. In contrast to specimen X1, this increased response is present on all four edges of the transverse cells and of much greater magnitude. The increased weave density of the twill fabric compared with the plain woven fabric results in a greater fibre crimp. This increase in crimp could explain the greater thermoelastic response at the cell boundaries compared with that from specimen X1. A speculative explanation for the increase in thermoelastic response at the lateral cell boundaries of the transverse cells might be that there is some extension / shear coupling due to the asymmetry in the weave pattern, causing the yarns to twist and introduce additional strains in the resin rich cell boundary. This is distinctly different from the plain weave.

The average ΔT values were measured from small areas at the centre of the cells, away from the regions strongly influenced by the cell boundaries. Hence the average ΔT values from the longitudinal and transverse cells of specimens X1 and X2 are more similar than first inspection of Figures 5.10 and 5.11 might suggest. The scatter in the results from specimen X2 is much greater than from X1, but is less on the smooth surface than on the rough.

It is evident from Figures 5.10 and 5.11 and Table 5.6 that the regions corresponding to the longitudinal and transverse fibres give practically identical ΔT values. The results from specimen X3 are very different in this respect. In Figure 5.12 the weave pattern has only been overlaid onto the TSA data from the smooth side. This is a best estimate based on a geometric correlation between the data and the weave pattern. For the data from the rough side it was neither possible to identify a clear geometric correlation between the thermoelastic response and the weave pattern as for specimen X1, nor was it possible to identify a distinct cell by visual inspection as for specimen X2, and therefore the weave pattern could not be overlaid. In a qualitative sense, the thermoelastic response

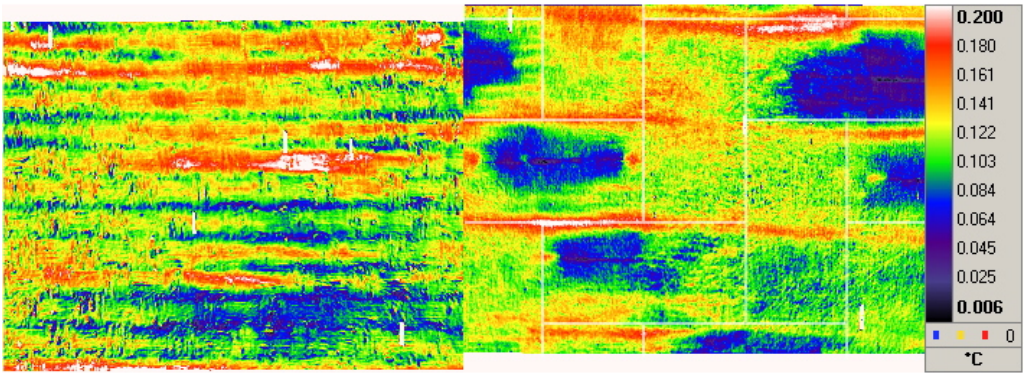

Figure 5.12: TSA data from Specimen X3, sub-region 3, (left) rough side, (right) smooth side. The weave pattern is overlaid.

from the smooth side matches the predictions from the patchwork model. The response from the longitudinal cells is greater than that from the transverse cells and at the boundaries between transverse cells where a reduction in the fibre volume fraction is expected there is a narrow region of increased response as from a resin pocket. However, the magnitude of the thermoelastic response does not match the predictions given in Table 5.5. The response from the transverse cells matches fairly well, but the values from the longitudinal cells and the cell boundaries are both approximately 40% larger than the predictions.

5.6 Discussion

In the following discussion, the experimental data are compared with the predicted thermoelastic response. Figure 5.13 presents the predictions and experimental results together in a single plot. Data points for the longitudinal cells are given open symbols; the data points for the transverse cells are given full symbols. The nomenclature is summarised in Table 5.7. The calculated data are designated C1 to C9 and have been obtained using the averaged test strains. The dashed-dot and solid lines (C1 and C2) represent the predicted response from the longitudinal and transverse cells for varying fibre volume fractions, applying the equations and material properties described in method 1. The dotted line (C3) represents the response from the resin only. Points C4 to C13 have been calculated using the material properties from Lit. 1 (C4 and C9), Lit. 2 (C5 and C10), the measured properties (Expt.)(C6 and C11), the FEA model yarn response (C7 and C12) and the FEA model surface resin layer response (C8 and C13). The experimental data are designated X1 to X5 according to the specimen from which the measurement was taken, and a following L or T is used to denote a longitudinal or transverse cell.

Of the mosaic model predictions, the most significance must be given to the predictions based on the measured material properties (C6 and C11) and those calculated using method 1 (C1, C2 and C3) since these are representative of the actual fibre / resin

combination used. The two sets both predict the response from the transverse cells to be approximately 20 to 30% lower than from the longitudinal cells for fibre volume fractions between 0.4 and 0.6. Although the magnitudes of C6 and C11 are much greater, the ratio is approximately the same. This can be attributed to the exceptionally high measured stiffness values E_1 and E_2.

The thermoelastic response from the transverse direction (X5) corresponds well with the predicted value C11. The longitudinal values X4 and C6 do not agree. However, both X4 and X5 agree well with thermoelastic prediction for the resin (C3). This suggests that the surface resin layer is acting as a strain witness.

Considering the single ply specimens it is noted that the thermoelastic response from the longitudinal and transverse cells is similar. By contrast, the response from the longitudinal and transverse cells of specimen X3 is different. Specimens X2 and X3 have the greatest similarity in terms of the material properties of the cells and the Poisson's ratio of the composite as a whole. This suggests that the local strain fields must differ between the two specimens, since the observed difference in the thermoelastic response cannot be explained by differences in either the material properties or the global strains. Assuming that the surface resin layer is acting as a strain witness, this implies that the strain field in the single ply specimens (X1 and X2) is uniform, except at the cell boundaries, while in the laminate (X3) the longitudinal and transverse cells experience a different strain. This is counter intuitive.

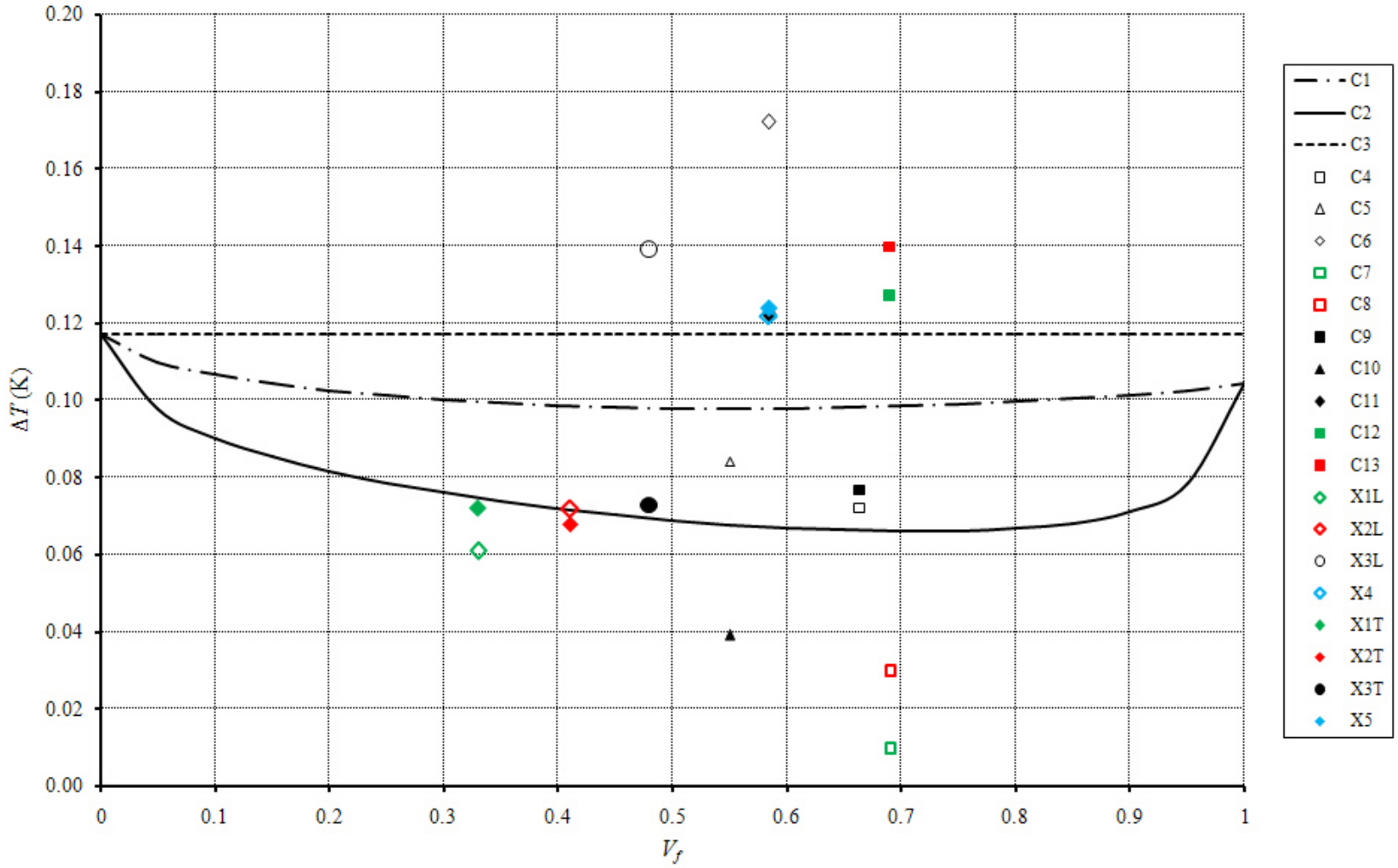

Figure 5.13: Comparison between the calculated and measured thermoelastic response using material properties from a variety of sources

Table 5.7: Nomenclature for thermoelastic data

Notation	Material Type		Orientation		Origin of Material Properties							ΔT			
	UD	Woven	L	T	Table 5.2	Theory	Lit. 1 [96, 15]	Lit. 2 [114]	Expt	FEA (yarn)	FEA (res.)	Equation 5.1	Equation 5.2	Equation 5.3	Measured
C1	x		x		x	x						x			
C2	x			x	x	x							x		
C3	-	-	-	-	x	-								x	
C4	x		x				x					x			
C5	x		x					x				x			
C6	x		x						x			x			
C7		x	x			x				x		-			
C8		x	x			x					x	-			
C9	x			x			x						x		
C10	x			x				x					x		
C11	x			x					x				x		
C12		x		x		x				x			-		
C13		x		x		x					x		-		
X1L		x	x		-	-	-	-	-						x
X2L		x	x		-	-	-	-	-						x
X3L		x	x		-	-	-	-	-						x
X4	x		x		-	-	-	-	-						x
X1T		x		x	-	-	-	-	-						x
X2T		x		x	-	-	-	-	-						x
X3T		x		x	-	-	-	-	-						x
X5	x			x	-	-	-	-	-						x

Comparing the response from specimens X1 to X3 with X4, X5 and C3 does not support the strain witness theory since none of the six values in either the longitudinal or transverse directions agree with either the predicted resin response or X4 and X5. Due to the weave pattern, the thickness of the surface resin layer varies considerably in the woven specimens. Hence it is possible that while the resin layer on the UD specimen is sufficiently thick to act as as strain witness the same is not the case for the woven specimens.

An alternative explanation of the data from specimens X1 to X3 can be made based on the mechanics of the weave. At first let it be assumed that the predictions C1 and C2 are accurate. Then the response from specimens X1 and X2 should present a pattern in which the longitudinal cells produce a response 20 to 30% greater than the transverse cells. However, the weave introduces an out-of-plane deformation of the tows. Taking a single tow in isolation it can be seen that the tensile extension will introduce a bending moment, serving to reduce the strain on the upper surface of longitudinal cell. This is shown schematically in Figure 5.14. The opposite compressive deformation will add a positive component to the strain in upper surface of the transverse cell. Hence, this out-of-plane deformation will serve to reduce the thermoelastic response in the case of the longitudinal cells, and increase the thermoelastic response in the case of the transverse cells. This corresponds with the 3D FE model which predicts a larger thermoelastic response from the transverse cells than from the longitudinal cells. In the case of the laminate (X3) however, these out-of-plane deformations are restricted by the underlying plies in the laminate. Hence the response from the longitudinal and transverse cells of a laminate will differ in a manner comparable to that predicted by the mosaic model.

Thus it is can be explained why the longitudinal responses X1L and X2L lie below the prediction C1, the transverse responses X1T, X2T and X3T agree with the prediction C2 and the response X3L is an outlier but follows the correct trend (i.e. X3L is greater than X3T). Also, this explanation allows for the UD specimens to fit the strain witness behaviour that has also been observed in other work using traditional laminated composites (e.g. [96, 78]).

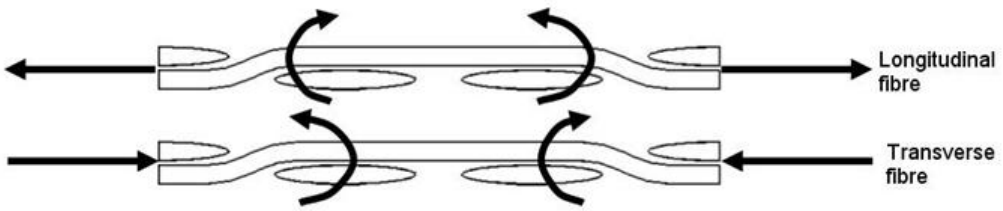

Figure 5.14: Schematic representation of tension / bend coupling in longitudinal and transverse yarns.

5.7 Summary

The use of motion compensation has enabled the thermoelastic response from a woven composite to be studied at the scale of the yarns. Thus it has been possible to isolate the thermoelastic response originating from the longitudinal yarns, transverse yarns and resin pockets in the thermoelastic data, permitting a comparison to be made with model predictions.

It has been demonstrated that the thermoelastic response is sensitive to the material properties, which in the case of FRP composites is dependent on the manufacturing process and the resulting material composition. A large range of material properties is quoted in the literature and care must be taken in selecting appropriate values when predicting the thermoelastic response. It has been shown that the values of the transverse material properties show the greatest variability and are most difficult to predict or measure accurately. However, it can generally be expected that under uniaxial loading conditions, the thermoelastic response from a UD E-glass / epoxy orientated parallel to the loading direction should be greater than or equal to the response from a material with a transverse orientation.

The mosaic model is shown to provide an unrealistic prediction of the ΔT field from a woven composite. The thermoelastic response is sensitive to the local variations in the 3D strain field. However, it provides a good basis for assessing local strain variations in relation to a global mean strain. As such, the patchwork approach can be used to inform on local strain concentrations from a material with a heterogeneous thermoelastic response. Thus it can be used to provide a background ΔT field for quantitative analysis of strain concentrations. The work in this chapter thereby demonstrates that a simple model of the material heterogeneity enables TSA to be applied to quantitative evaluation of materials with a heterogenous thermoelastic response.

Chapter 6

Fatigue damage accumulation in single and two-ply woven composites

6.1 Introduction

Most engineering structures are subjected to some form of time varying load which can lead to degradation of the material strength. The higher the stresses relative to the failure strength of the material, the more rapidly the material fatigues. The desire to improve structural performance often translates directly as a requirement to reduce weight with the consequence of increasing stresses in structures. Reduced weight has been one the driving factors in the development of composite materials, in particular FRP [1], as discussed in Chapter 2. The accumulation of fatigue damage is therefore a topic of great concern in many FRP structures. The work in this chapter investigates the use of TSA in the application to fatigue assessment in woven FRP composites. TSA is particularly well suited to this application because measurements can be obtained from a dynamically loaded component, in practically real time (less than 5 seconds per measurement). The measurement technique can therefore be applied directly to a component with minimal preparation time and data collected and analysed in situ, as the material is exposed to fatigue loading.

During a normal TSA test, the applied stress amplitude is kept low relative to the failure stress to avoid fatigue damage developing in the material. However, a minimum stress amplitude must be applied in the specimen to enable a viable measurement to be made. In a typical E-glass / epoxy composite for which, in the fibre direction, a stress change of 1 MPa results in a temperature change of 1.5 mK, the minimum stress threshold is in the range of 10 to 20 MPa, below which variations in the stress field cannot be resolved. On reviewing data obtained from the 2 x 2 twill woven composites used in Chapter 5 a marked change was observed in the thermoelastic response from individual specimens that had been subjected to repeated testing, despite the peak stresses during

the loading cycles having been well below the failure stress of the material. Therefore it was likely that fatigue damage was evolving during the low stress cyclic loading applied to the specimen. This finding has motivated the research described in this chapter with a view to identifying the cause of the low stress amplitude, cyclic fatigue damage in textile composites. The work in this chapter therefore aims to investigate woven composite materials under low amplitude (less than 20% of the failure stress) cyclic loading conditions.

6.2 Methodology

The focus of the work is the onset of fatigue damage and the rate of damage accumulation. Changes in the meso-scale stress field (i.e. at the scale of the yarns) are used to identify and quantify the damage. The stress field was monitored using TSA, at set intervals during the fatigue process. Since TSA relies on dynamic loading, it was possible to obtain the measurements without interruption of the loading cycle. Specimens were fatigued under constant load amplitude to grow damage. Changes in the global material stiffness were monitored by means of the change in the displacement amplitude.

During cyclic loading the specimen may heat, particularly in areas of localised damage [110]. Therefore it is necessary to eliminate any effects of local surface temperature increase, by normalising the temperature change with the mean surface temperature to give data in the form $\Delta T/T$, which can be considered as a non-dimensional stress metric. This normalisation is conducted on a pixel-by-pixel basis over the entire field. An added advantage of the normalisation is that variations in laboratory temperature are eliminated and direct comparisons can be made between different data sets.

To monitor the damage progression data was obtained periodically during the fatigue process. Local changes of the material response in all fatigue tests were measured relative to an initial $\Delta T/T$ data set obtained from the undamaged material. To inspect the stress field at the scale of the yarn, the G1 high resolution optics were employed. The rigid body motion of the specimens was corrected for using the motion compensation algorithm procedure described in section 4.4.

The specimens were further inspected using an optical microscope before and after fatigue testing to identify, for example, the formation of matrix cracks. Accumulation of fatigue damage identified in the TSA data could thus be correlated to the location and extent of visible damage in the material. Differences in the accumulation and distribution of fatigue damage between different materials could be related to differences in the textile structure and material composition.

6.3 Material selection and specimen configuration

Two E-glass textiles with a 2 x 2 twill woven roving were selected for this investigation. These were WRE581T (the same 2 x 2 twill textile as used in Chapter 5)

Table 6.1: Textile dimensions

Textile	Warp yarn spacing (mm)	Weft yarn spacing (mm)	Warp yarn crimp (%)	Textile thickness (mm)	Fibre volume fraction (%)
WRE581T	2.00	2.17	5	0.559	50
RE400T	1.65	1.52	4	0.405	40

and RE400T, both purchased through Gurit, with areal densities of 581 and 400 g m^{-2} respectively. The WRE581T textile used 600 tex yarns in both the warp and weft directions, with 5 ends per cm for the warp yarns and 4.6 ends per cm for the weft yarns. The RE400T textile used 336.6 tex yarns with 6.1 ends per cm in the warp direction, and 273.6 tex fibres with 6.6 ends per cm in the weft direction. The E-glass fibres in the WRE581T textile had a diameter of 19 μm while those in the RE400T had a diameter of only 9 μm. The resulting textile dimensions are listed in Table 6.1. The fibre crimp was measured as the ratio of the out-of-plane deformation to the length of the textile unit-cell.

Two textiles were chosen so that the effect of small differences in the weave on the fatigue behaviour could be investigated. The effect of stacking the textiles was also studied. For this, single and two ply composites were manufactured, one using the WRE581T textile stacked periodically (i.e. the undulations in the warp yarns in adjacent plies were in phase), the other using the RE400T textile stacked symmetrically (i.e. the undulations in the warp yarns in adjacent plies were out of phase).

The epoxy resin used to form the composite material was Prime 20LV from Gurit, cured using their fast hardener. The composites were manufactured as a flat panel by means of liquid resin infusion, with consolidation at 1 atmosphere of pressure. The specimens were cut from the panel, had end tabs bonded and were then post cured for 16 hours at 50° C.

The specimen dimensions were based around ASTM D 3039. They were nominally 25 mm wide and the gauge length was increased from the standard 150 mm to 250 mm to enable access with the G1 high resolution lens. To eliminate the possibility of slippage that sometimes occurs during long term cyclic loading with standard grips, the specimens were pin loaded via 12 mm diameter holes drilled at each end of the specimen. The specimens were fitted with the standard 50 mm long end tabs and additional 1.5 mm thick aluminium end tabs (40 mm long) were added to serve as a bearing material for the loading pin, eliminating any possible damage growth from the pin-loaded hole.

6.4 Experimental arrangements

The fatigue loading conditions were determined from the failure stress of each material. Table 6.2 shows the average failure stress obtained from five quasi-static tensile tests. The specimens were fatigued under constant load amplitude (tension - tension) sinusoidal loading at 10 Hz, using an Instron 8872 servo-hydraulic test machine. The load

amplitude was set to cycle from nearly zero, giving a minimum stress of between 2 and 6 MPa, to a peak stress of 10, 15 and 20 % of the failure stress for each material. The tests were run for 12 hours (440000 cycles) at 10 % of the failure stress and for 5 hours (180000 cycles) at 15 and 20 % of the failure stress. TSA measurements were taken every 600 cycles for the first 4000 cycles and then every 6000 cycles. Each specimen was tested once only. Separate, identical specimens were used for setup and tuning of the servo-hydraulic test machine prior to each test. The displacement amplitude of the actuator was recorded at the start and the end of every test to provide an indication of a change in the global stiffness of the material.

Table 6.2: Average failure stress for each material

Material	WRE581T (1 ply)	WRE581T (2 ply)	RE400T (1 ply)	RE400T (2 ply)
Failure Stress (MPa)	416.2	481.5	333.1	340.8
Standard Deviation (%)	0.36	4.59	4.29	6.79

IR measurements were obtained with both the 27 mm standard lens and the G1 high resolution lens. For tests using the 27 mm lens, the detector was positioned with a stand-off distance of approximately 350 mm at an angle of 5 to 10° to avoid the Narcissus effect. This yielded a viewing area of approximately 80 x 100 mm. The G1 lens required a much closer stand-off distance (approximately 8 mm) and a perpendicular orientation of the detector due to the very short focal depth (approximately 0.5 mm) of the G1 optics. The G1 lens covered a viewing area of 8 x 10 mm, roughly one unit cell in the weave pattern.

Post-fatigue examinations were conducted using a macro-scope with x 10 magnification and a microscope up to x 50 magnification. For the microscope examinations, the area studied using TSA was cut out of the specimen, and the cross-section was polished with 4000 grit sandpaper on a polishing wheel.

6.5 Macro-scale response

The non-dimensional thermoelastic response from all four materials in the undamaged state for the 10% loading case is shown in Figure 6.1. Similarities can be seen in the response from the two single ply specimens and the WRE581T two ply specimen. The lowest response (blue regions) comes from the warp yarns while the weft yarns are bounded above and below by narrow bands of the highest response (red regions). This corresponds to strain concentrations either side of weft yarns measured using shearography in [46]. The RE400T two ply specimen however shows a markedly different pattern. This can be attributed to the difference in the stacking sequence, in-phase periodic for the WRE581T and symmetric for the RE400T. The stacking sequence influences the stress field because it changes how the two plies interact. This may be expected to

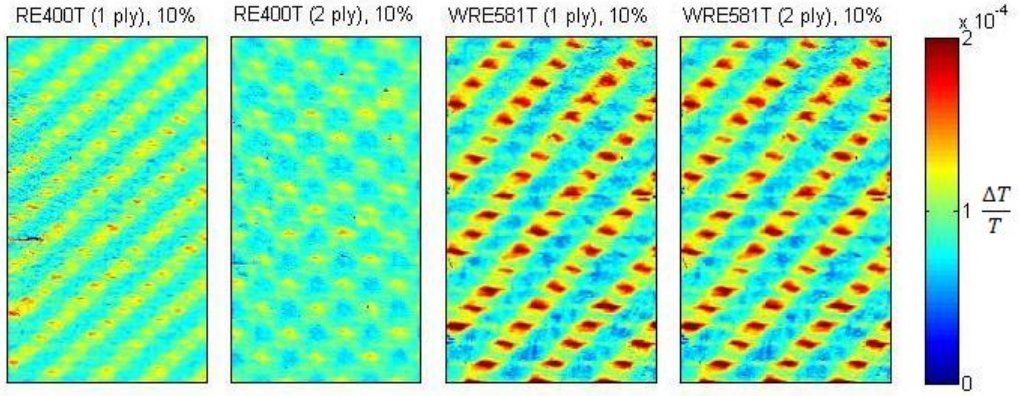

Figure 6.1: Measured non-dimensional stress field from virgin material

have an effect on the magnitude of the stress concentrations and hence on the fatigue behaviour of the material. The difference in the magnitude of the response between the different materials is due to the differences in the applied peak stress: 41.6 and 48.1 MPa for the WRE581T single and two ply specimens compared with 33.3 and 34.1 MPa for the RE400T single and two ply specimens.

An estimate of the global change in stiffness was obtained from the change in the displacement amplitude. The overall change for each specimen is listed in Table 6.3. At 10% load, the change was negligible in all specimens. At 15 and 20% load, the single ply specimens showed a reduction in stiffness of up to 15%. The RE400T two ply specimen showed no change at all, while a significant reduction of the WRE581T two ply specimen was found only in the 20% loading case. Although the actuator displacement amplitude during a dynamic test does not provide an accurate Young's modulus, these values show that a reduction in stiffness does accompany the accumulation of damage.

Table 6.3: Change in Young's modulus

(a) RE400T (GPa)

	1 ply			2 ply		
	10%	15%	20%	10%	15%	20%
Initial	41.23	38.46	40.16	42.42	44.66	41.85
Final	40.12	34.97	35.07	42.93	44.93	41.04
Percentage reduction	2.69	9.07	12.67	-1.20	-0.6	1.94

(b) WRE581T (GPa)

	1 ply			2 ply		
	10%	15%	20%	10%	15%	20%
Initial	46.04	44.64	42.89	48.68	48.03	48.43
Final	44.01	37.82	36.57	-	45.84	44.03
Percentage reduction	4.41	15.28	14.74	-	4.56	9.09

The global average thermoelastic response was obtained by taking the average of the thermoelastic data from an area, roughly equivalent to that shown in Figure 6.1, which represents a box of 45 mm in length by 25 mm wide. The data was then normalised

against the virgin data for each test case. The normalised global average thermoelastic response is shown in Figure 6.2, from the virgin material through to the end of the test. (Note that the specimens were not tested to failure.) The two ply RE400T specimen, which shows the lowest level of stress concentrations in the virgin data, also shows the least change in the net thermoelastic response as a result of the fatigue cycling. The single ply RE400T specimen and the two ply WRE581T specimen display a comparable decrease in the net thermoelastic response. The greatest change is observed in the single ply WRE581T specimen.

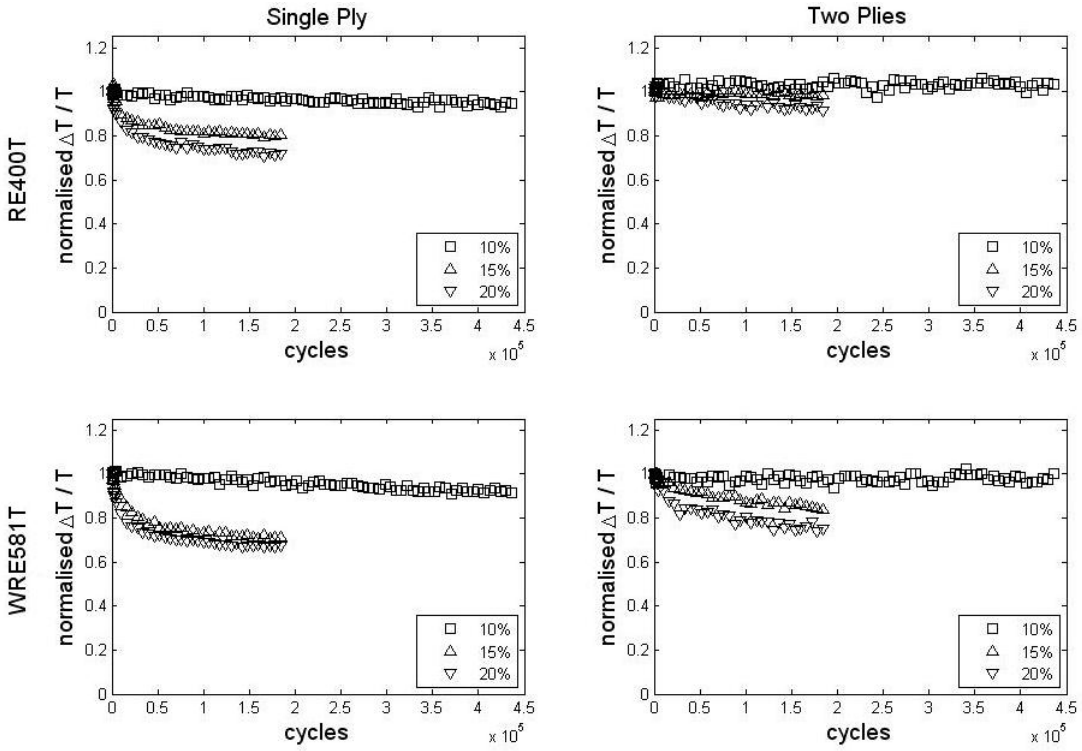

Figure 6.2: Global averaged thermoelastic response

Both single ply specimens show a gradual linear decrease in the net thermoelastic response for the 10% loading case. For the two ply specimens the 10% loading case shows no net decrease. For the 15% and 20% loading cases, both single ply specimens show an initial rapid decrease in the net thermoelastic response, followed by a transition to a stable value approximately 20% and 30% lower than the initial data for the RE400T and WRE581T respectively. In contrast, both of the two ply specimens exhibit an approximately linear decrease in the net thermoelastic response for the same two loading cases. This suggests that the interaction between the two plies leads to improved resistance to the accumulation of fatigue damage. Moreover the reduction for the symmetrically stacked laminate shows improved resistance in comparison to the in-phase laminate. The greater resilience of the RE400T compared with the WRE581T and of the two ply specimens compared with the single ply specimens coincides well with the average Young's modulus data.

The net decrease in the material response also serves as an indicator relating to the redistribution of stresses in the material. As damage progresses, stresses previously carried by one part of the material are redistributed to other parts of the material. It might therefore be expected that the net global response should remain constant, while the variation in the thermoelastic response across the specimens increases. Figure 6.2 shows quite clearly that the global response decreases. To estimate the change in the variation in the response the standard deviation in the global response is used. Figure 6.3 shows the standard deviation in the response, which also decreases proportionally to the average, i.e. the variation in the thermoelastic response remains constant relative to the global average. On closer inspection, it is revealed that the thermoelastic response from the warp yarns remains constant throughout the accumulation of fatigue damage, as shown in Figure 6.4. The decrease in the global thermoelastic response originates solely in the weft yarns. This implies, firstly, that the damage is occurring in the weft yarns and secondly, that the weft yarns contribute negligibly to the load carrying capacity of the textile in the warp direction.

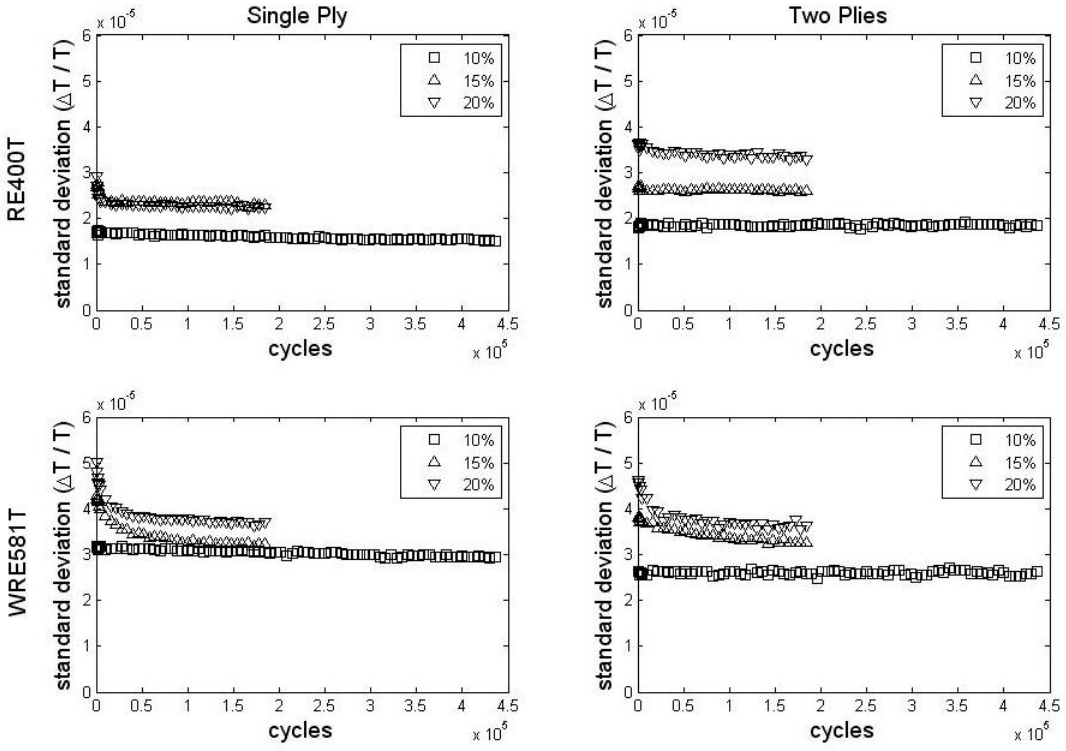

Figure 6.3: Standard deviation of globally averaged thermoelastic response

Figures 6.5(a) and 6.5(b) show macroscope images from the fatigued specimens of the WRE581T and RE400T single ply specimens. The specimens were lit from the side, hence revealing subsurface discontinuities in the material. It is clear in both images that there are transverse cracks running along the weft yarns. The weave pattern has been overlaid approximately for clarity. Figure 6.5(a) shows that cracks in the WRE581T material form as a single crack through the centre of the yarn, in some cases accompanied

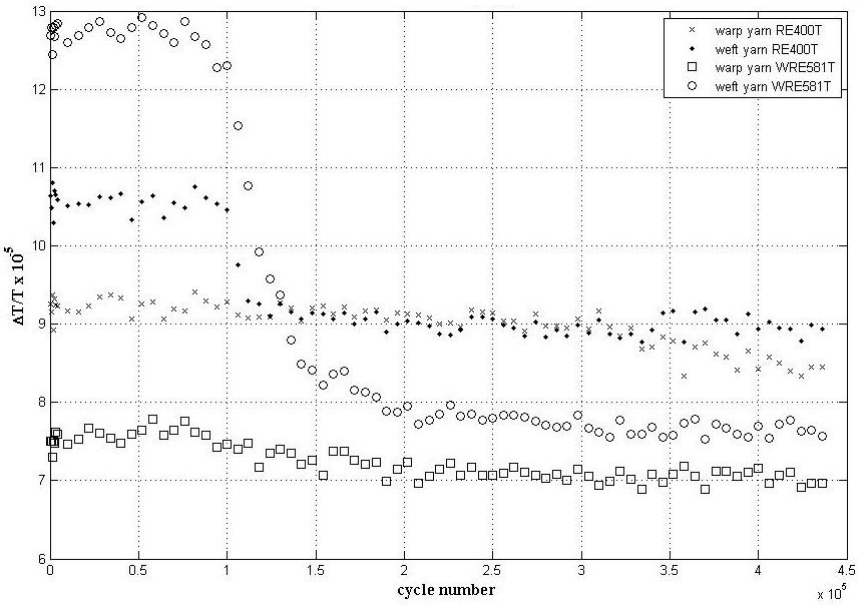

Figure 6.4: Non-dimensional thermoelastic response from a typical warp and weft yarn in both the RE400T and WRE581T single ply composites, loaded at 10% of the failure load.

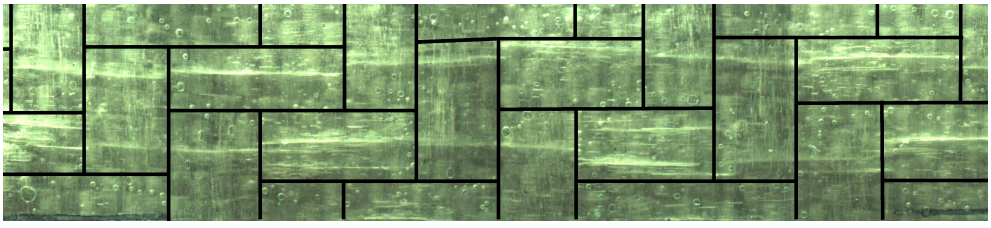

(a) WRE581T single ply

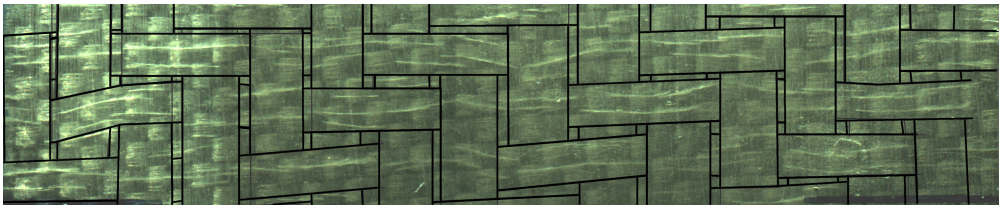

(b) RE400T single ply

Figure 6.5: Macroscope images after 184000 cycles

by smaller parallel cracks along the yarn edges. The cracks grow until they reach a warp yarn where they stop. The cracks can be seen to continue on the opposite face, interrupted by the crossing warp yarn. In the RE400T material the weft yarns are not as well aligned. The cracks appear more often as two parallel cracks, as shown in Figure 6.5(b). The spacing between the cracks indicates that they occur within the weft yarns, just either side of the yarn centre line. This demonstrates that the damage is evolving locally in the weft yarns and that it is therefore necessary to examine the behaviour at the yarn level to fully understand the damage accumulation mechanism.

6.6 Meso-scale study

It is observed in Figure 6.1 that the thermoelastic response from the weft yarns is approximately 30% greater than that from the warp yarns, while the strongest response originates from the boundary between two weft yarns. The response from the warp and weft cells of the WRE581T single ply material in the undamaged state and for the 10% load case was compared to predictions based on the FEA and mosaic models in section 5.4. A strain of 0.09% in the longitudinal (warp) direction was applied in the models to match the 10% loading case. The non-dimensional thermoelastic response is shown in Table 6.4. The higher response from the warp yarn and the lower response from the weft yarn compared to the predictions can be explained by the relatively low loading frequency of 10 Hz. This was used to avoid viscoelastic heating during the prolonged fatigue cycling. As stated in section 5.4, this lies well below the minimum threshold of 30 Hz needed to achieve quasi-adiabatic conditions. It does however show that the FE model, using material properties calculated from the constituent materials, is able to produce reasonable predictions of the thermoelastic response. Heat transfer would need to be included to draw more concrete conclusions.

Table 6.4: Comparison of thermoelastic response with model predictions

	Experiment	FEA (yarn)	FEA (resin)	Mosaic (Expt.)
Warp	7.5×10^{-5}	5.1×10^{-5}	1.7×10^{-5}	29.2×10^{-5}
Weft	12.8×10^{-5}	21.6×10^{-5}	20.7×10^{-5}	20.7×10^{-5}

As the material begins to fatigue the thermoelastic response from the weft yarns decreases. The weft yarns 'fail' locally (i.e. individual cells fail independently of each other) and this can happen very early in the fatigue process. In the case of the single ply WRE581T loaded at 20% of the failure stress, the earliest incidence of fatigue damage in a weft cell was observed after only 200 cycles. The thermoelastic response falls sharply at first, until a point is reached where no further decrease in the thermoelastic response occurs. This continues until all the weft cells have failed in this way.

To identify in more detail the changes in the thermoelastic response around the weft yarns, data was captured using high resolution optics. Figure 6.6 shows data from one weft cell in the single ply WRE581T material, subjected to the 10% loading case, at

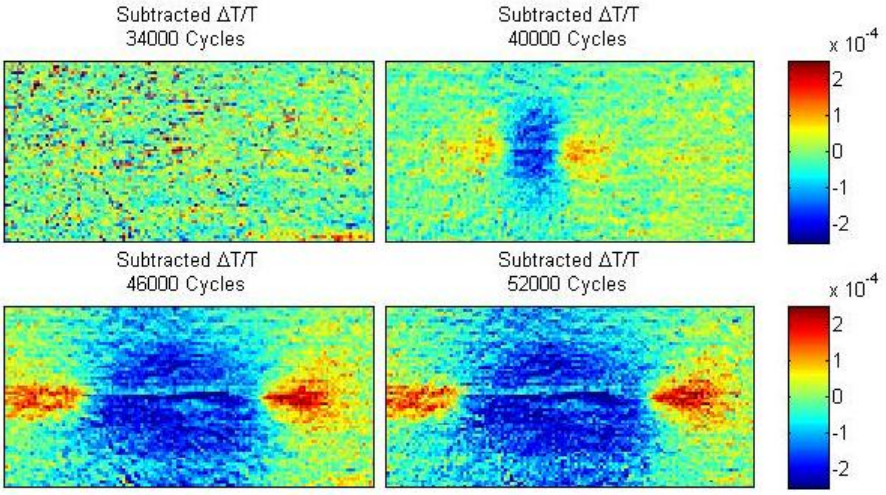

Figure 6.6: Subtracted thermoelastic image of single ply, WRE581T specimen loaded at 10% of the failure stress

four different stages in the fatigue process. The data from the virgin material has been subtracted from the corresponding fatigued material data to show the change in the $\Delta T/T$ field. In the first image it is clear that no damage has occurred in the yarn after 34000 cycles. Damage initiates at approximately 40000 cycles in the centre of the yarn. This is identified by the decrease in the signal (blue) at the centre of the cell, and the two small regions of increased response (red) either side. By 46000 cycles the damage has reached the warp yarns on either side and the damage evolution is arrested. The thermoelastic response from the whole region of the weft yarn decreases by approximately 2×10^{-4} K (approximately 30% of the original value). No further decrease in the signal occurs; neither does the effected area grow. The two 'stress concentrations' either side of the failed area of the cell remain, but do not develop further.

This decrease in the thermoelastic response can be linked to a decoupling of the weft yarn from the global strain field as a result of a transverse crack in the centre, or along the edges. The two small regions either side of the yarn centre resemble crack tip stresses found in metals [120] supporting the idea that the change in the thermoelastic response is due to changes in the stress field around a growing crack. At either end of the crack, the material is bounded by the warp yarns which are able to bridge the crack, explaining why the damage stops growing when it reaches this point. Corresponding data from the centre of a warp yarn shows no measurable change in the thermoelastic response. This data thereby adds detail and confirms the findings from the global TSA data and the macroscope images, however, it does not provide any additional information regarding the mechanics that lead to the damage, or the source of the thermoelastic response. Also, the subtractive method for establishing the presence or severity of damage as shown above assumes *a priori* knowledge of a virgin, undamaged state. It is desirable to establish a means of identifying damage without the virgin data set for comparison.

6.7 Damage identification

Firstly the cross-section parallel to the warp yarns was studied using a microscope, up to a magnification of ×50; micrographs are shown in Figure 6.7. In the WRE581T material, the cracks can be seen to penetrate the full thickness of the weft yarn. Upon reaching the warp yarns, the cracks change direction to follow the boundary between the warp and the weft yarn, resulting in a delamination between the warp and weft yarns. This coincides with findings by Osada et al. [14]. An example is shown in Figure 6.7a, taken from the WRE581T single ply specimen after 180000 cycles at 20% of the failure stress. The crack is highlighted by a thin black line. The cracks in the RE400T material were much finer, and through yarn cracks could not be identified in any of the specimens. Only a shallow penetration of 40 to 110 μm could reliably be measured, as shown in Figure 6.7b. The difference in the size of the cracks between the WRE581T and the RE400T materials might be due to the difference in the fibre diameter between the two materials. The images imply that fatigue is more acute in the heavier textile, with greater yarn crimp and larger fibre diameter.

Figure 6.8 shows the phase data for the same region shown in Figure 6.6, but including also the adjacent yarns. The pattern of the weave has been superimposed on the data in black. It is immediately striking that there is a phase difference between the warp and the weft yarns in the undamaged state, measured as 8°. The response from the weft yarns is initially 180° out of phase with the load while that of the warp yarns is 188° out of phase. This difference in the phase angle could be due to a through yarn stress gradient, resulting from the yarn crimp which imposes a bending stress on the yarns additional to the net tensile stress carried. The crimp also induces a through thickness compressive stress which decays to zero at the outer surface of the yarn. The same is true for the transverse yarns, except that the direction of the yarn bending is opposite to that in the warp yarns. The full three-dimensional stress field therefore needs to be considered to explain this phase shift in the undamaged state.

As the damage initiates, the phase angle in the weft yarn increases to 190° in the

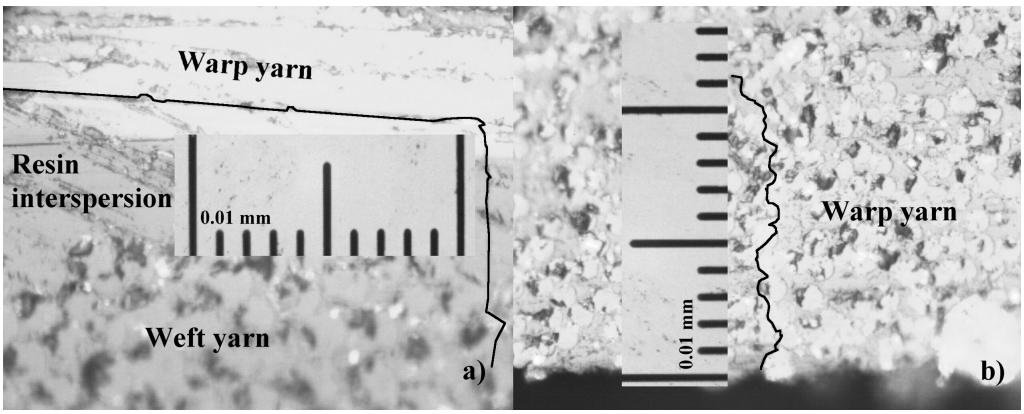

Figure 6.7: x 50 magnification images of the cracks in the weft yarns with 10 μm graticule a) WRE581T warp / weft interface crack propagation, b) RE400T weft surface crack

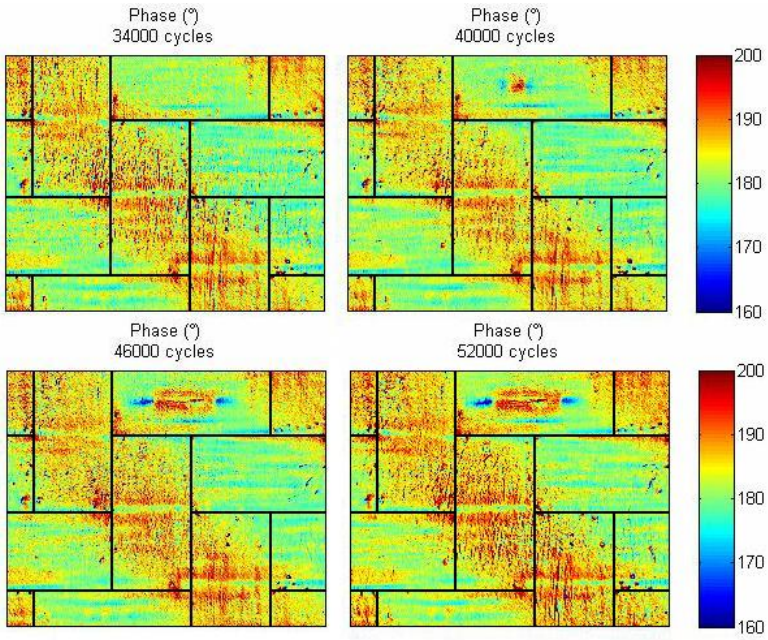

Figure 6.8: Phase data from a single ply, WRE581T specimen loaded at 10% of the failure stress

centre, while the two small stress concentrations either side display a decrease of approximately 10° in the phase angle. A line plot through the centre of the weft yarn shows the profile of the phase along the length of the weft yarn, see Figure 6.9. (The weft yarn lies between 2 and 6 mm along the x-axis.) Once the damage has fully developed, there is a 20° phase shift between the central region and the ends of the crack. This pattern propagates in exactly the same way as the thermoelastic response shown in Figure 6.6, thereby providing a signature pattern in the phase data that allows fatigue damage to be identified, without the requirement for a data set of the undamaged material.

6.8 Discussion

A change in the Young's modulus, i.e. residual stiffness, is often used as a measure of fatigue damage [121]. However, this change can be gradual, and it is not readily applicable to full field assessments. Neither does it provide information on the nature of the damage accumulation. The current work demonstrates how TSA can be used to identify damage in a heterogeneous material, such as a woven FRP composite. The strength of the technique lies in the ability to obtain data-rich measurements directly from the dynamically loaded component without interruption to the fatigue process. The straight forward temperature measurement can indicate viscoelastic heating often associated with damage. Averaging over many measurements and load cycles enables very small temperature anomalies to be identified, of the order of a few mK. For the low stress cycling used in this work, however, a simple map of the temperature evolution (shown in Figures 6.10a) and b)) shows that viscoelastic heating is not occurring at the

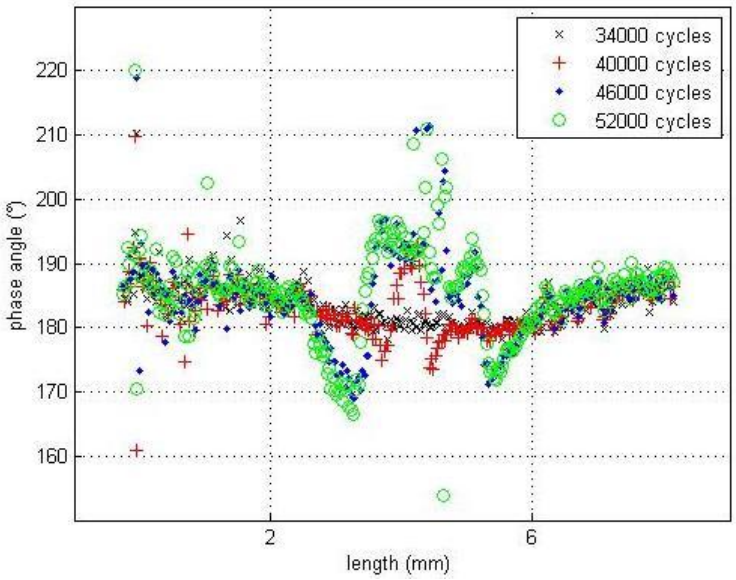

Figure 6.9: Line plot along the centreline of the weft cell highlighted in Figure 6.8 for increasing damage states

damage site.

Figures 6.11a) and b) show the thermoelastic ΔT field in which the damage is not apparent. The damage becomes clear when a direct comparison with the virgin data can be made, as shown in Figures 6.12a) and b). Here the non-dimensional metric ($\Delta T/T$) is subtracted from the undamaged data set to enable the damage site to be located precisely, and clearly indicates that the damage mechanism is the formation of matrix cracks in the weft yarns. The work in this chapter shows that the damage mechanism is the same for two materials with different damage resilience and different fibres, but similar weave geometries.

Since in an industrial situation, the undamaged $\Delta T/T$ field may not be known, the identification of a signature pattern in the phase data as shown in Figures 6.13a) and b) is an important outcome. A phase difference between the warp and weft yarns that may be due to either heat transfer between the two, or a mechanical effect resulting in asynchronous loading of the two sets of yarns does not impair the ability to detect damage. A change in the phase angle at the damage site produces an easily identifiable signature pattern, similar to that found in the subtracted $\Delta T/T$ data. Thus the phase data can be used to identify damage in the absence of *a priori* knowledge of the virgin thermoelastic field.

6.9 Summary

The chapter highlights the potential for fatigue damage to accumulate rapidly in woven composite materials, even at low stress levels. The damage accumulation is most pronounced in single ply 'laminates' such as may be used as the face sheet material in sandwich structures. It is shown that small differences in the textile, for example the use

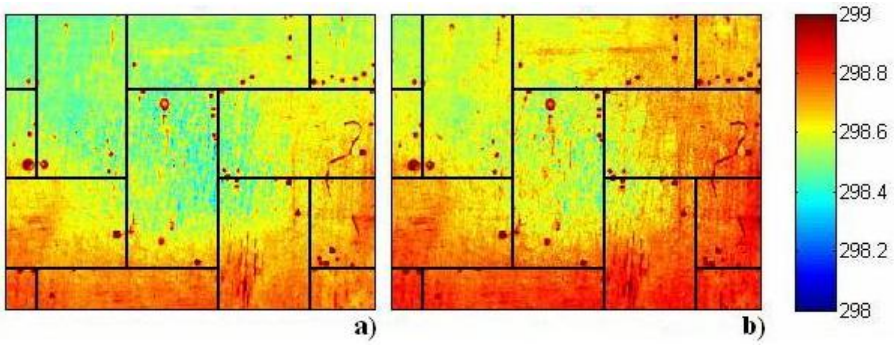

Figure 6.10: Mean surface temperature of WRE581T single ply material, under 10% loading after a) 40000 cycles and b) 46000 cycles

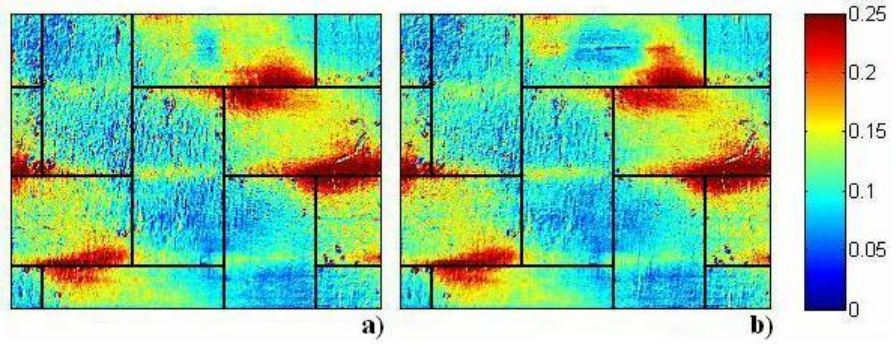

Figure 6.11: ΔT field of WRE581T single ply material, under 10% loading after a) 40000 cycles and b) 46000 cycles

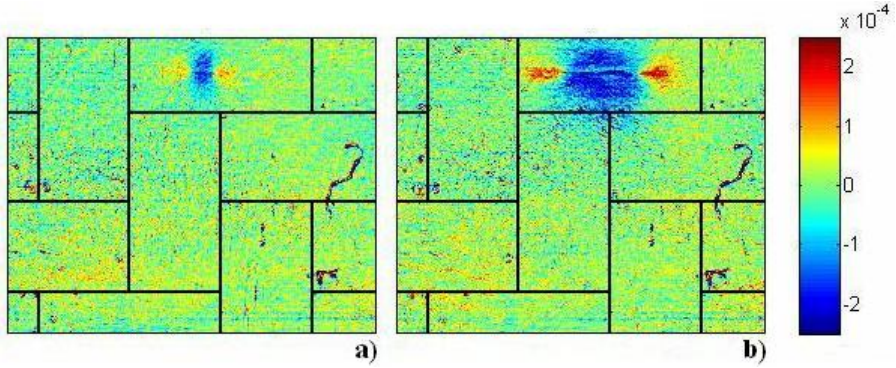

Figure 6.12: Subtracted $\Delta T/T$ field of WRE581T single ply material, under 10% loading after a) 40000 cycles and b) 46000 cycles

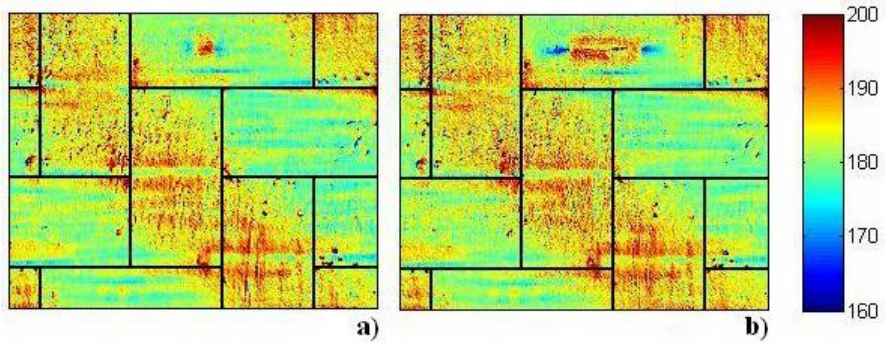

Figure 6.13: Phase plot of WRE581T single ply material, under 10% loading after a) 40000 cycles and b) 46000 cycles

of a different yarn, can result in greatly improved resistance to damage initiation. Also, the interaction between plies within a laminate can substantially reduce the susceptibility to the development of this type of fatigue. This has implications for applications in which heavier weight textiles and reduced ply numbers are used to reduce manufacturing costs, or where sandwich structures with very thin face sheets are used to reduce weight. Further studies are required to identify if the textile weight, the yarn crimp or the fibre diameter is the most critical parameter influencing the susceptibility to this type of damage accumulation. While the development of matrix cracks does not lead directly to failure at the load levels used in the tests, it should be noted that the presence of cracks at the surface may lead to greater susceptibility towards environmental degradation, such as the ingress of water. Also, it has not been possible to verify if the fatigue damage developed at these low loading amplitudes leads to a reduction in the ultimate failure strength of the material.

The potential to identify the growth of small scale damage by means of TSA has been clearly demonstrated. By considering the thermoelastic response in a non-dimensional form, data obtained under different conditions (i.e. collected at different ambient temperatures) can be reliably compared. TSA thereby provides a robust tool for evaluating damage development in structural FRP composite components.

The interpretation of a signature pattern for a particular type of defect can be of great use in practical engineering applications. The use of the phase data to identify damage enables the technique to be applied without *a priori* knowledge of the material thermoelastic response in a virgin state. The phase data also shows potential to provide new insight into the meso-scale mechanics of woven materials. The deeper implications of small phase shifts in the undamaged state between the warp and weft yarns require further investigation. It is proposed that the phase change is due to heat transfer resulting from stress gradients in the through thickness direction.

The study has demonstrated the successful identification of micro-cracking in woven composite materials using TSA. An improved understanding of the thermoelastic response from this type of material has been achieved enabling greater confidence in the interpretation of TSA data from woven composite materials. Fatigue in woven compos-

ites at low loading levels has been observed together with the signature pattern enabling the damage to be identified. Therefore the study represents significant progress in the application of TSA in the study of the behaviour of woven composite materials.

The next logical step in the development of TSA as a damage assessment tool is to consider how the technique might be applied in an industrial context. The feasibility of applying TSA in the absence of a servo-hydraulic test machine is therefore the subject of the next chapter.

Chapter 7

Thermoelastic Response of Composite Structures under Transient Loads

7.1 Introduction

In Chapter 6 it has been shown that TSA can be used to assess woven composite materials for damage at small scales. Other work has also been conducted considering damage detection in conventional laminates [23]. The potential to use TSA for general damage assessment in composite materials has thereby been proven. Yet, although TSA has been established for over two decades, it has not found widespread application in industry. One reason for this is that the requirement for a cyclic load has limited it to the laboratory environment with specialised equipment [24]. The aim of the work described in this chapter is to investigate the application of TSA to a component subjected to a single transient load. The motivation behind this investigation has been to develop a new application for TSA as a structural / damage assessment tool, in an environment where no facility for introducing cyclic loads into a structure exists. The target application is routine maintenance checks for assessing the safety and residual life of composite structures.

An important question is whether stress concentrations at a damage site can be detected. As stated in Chapter 6, in a typical E-glass / epoxy composite, a change in stress of 1 MPa in the fibre direction produces a change in temperature of approximately 1.5 mK. The thermal resolution of the Cedip Silver 480M detector is 4.2 mK with an electronic noise of 15.75 mK (as stated in Chapter 4). The smallest stress change that can be measured without further processing of the IR data would hence be of the order of 10 MPa. Eliminating the electronic noise would enable the minimum resolvable stress change to be reduced to approximately 3 MPa. This can be regarded as the best resolution achievable from a single excitation using the Silver 480M detector. In this first stage of work only a simple averaging technique has been considered to improve the

thermal resolution.

The second challenge is to design a method of introducing a dynamic load into the component of sufficient magnitude to produce a measurable temperature change, without the use of laboratory based test machines. In the current work, two methods of imparting a transient load are used. The first uses a servo-hydraulic test machine to apply a uniaxial tension step load to a strip of material. The second approach addresses the aim of applying a load without a test machine and is based on a single controlled impact on a cantilever beam.

Finally, the ability to identify changes in the thermoelastic response as a result of damage evolution is verified. Two types of damage were investigated. The first considered the progression of damage around a hole; the second considered delamination damage between two subsurface plies.

The work in this chapter aims to develop a test procedure with which consistent and comparable data can be collected without the use of a servo-hydraulic test machine, thereby verifying the feasibility of applying TSA to damage detection in the field.

7.2 Transient load methodology and validation strategy

The two methods of imparting a transient load into a material are the step load method, in which a uniaxial tension specimen is subjected to a single load step using a servo-hydraulic test machine, and the impact method, in which a cantilever beam is subjected to a single impact by a pendulum. The validation strategy is shown in Figure 7.1 and is divided into three parts. In box 1, the step load method is validated. This test provides a loading case that enables direct comparison of the transient method with measurements obtained using a cyclic load (hitherto called the 'standard' method) and calculations based on measured material properties. As shown in Chapter 5, it is important to assess the accuracy of calculated values of ΔT. The validation of the step load method is therefore also a validation of the material properties used to obtain the calculated data, which are used to validate the impact method (box 2 in Figure 7.1).

A cantilever beam specimen was used because it provides a simple loading case for which the stress field can be calculated using straight forward analytical methods. A test rig has been designed for this purpose and is based on the application of an impact load to a cantilever beam; the rig is shown schematically in Figure 7.2. The impact is imparted into the specimen using a pendulum that is released from a known height, thereby providing a repeatable load. The test rig incorporates a mechanism that captures the impactor after the first rebound and prevents repeated loads from being applied. In the current work the magnitude of the applied load is determined by measuring the deflection at the end of the cantilever beam optically from above. However, it would be possible to incorporate a force transducer in the impactor and it is envisaged that this is how the technique would be applied in the field.

The above validation will demonstrate the reliability and accuracy of the transient

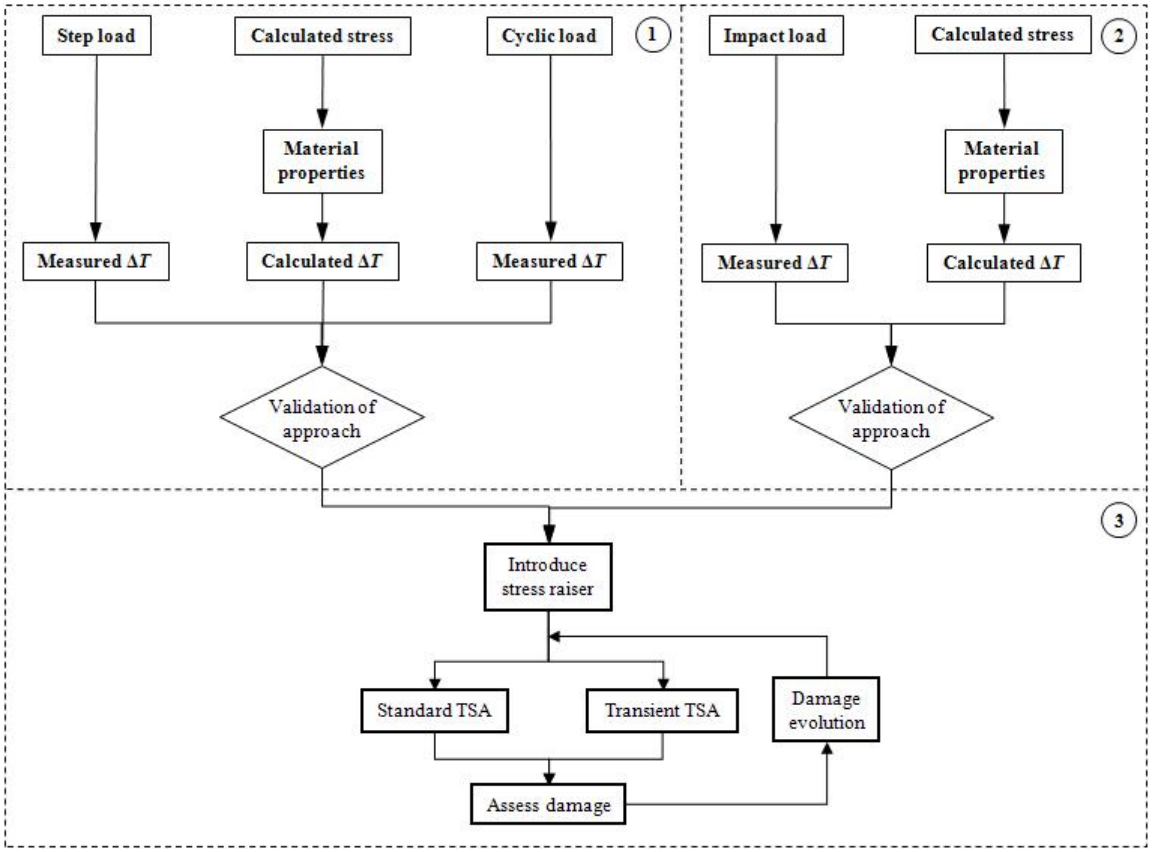

Figure 7.1: Flow chart of the validation strategy for the transient loading methodology

load methodology. This will inform if a transient load is suitable for TSA and what conditions are required to apply the methodology for damage assessment. In the third part of the validation (box 3 in Figure 7.1) the application of the transient load methodologies to two types of stress raiser is evaluated. This is described in greater detail in section 7.5.

The first step is to characterise each material to be tested. This includes determining the mechanical properties in a standard quasi-static tensile test and performing a stress calibration using a uniaxial tensile strip and the standard TSA approach. Thermography data is then obtained from a specimen subjected to a single transient load. Using the known material properties and load conditions the stress field is calculated. The stress calibration is used to convert the thermographic data to stress data and so obtain a measured stress field. The measured and calculated stress fields can then be compared to validate the approach.

In the second part of the methodology a stress raiser is introduced into the specimen. The standard and transient TSA approaches are then used to measure the stress field and stress concentrations around the stress raiser. The specimen is then subjected to cyclic fatigue loading to initiate and propagate damage at the site of the stress raiser. At each stage the stress field is measured and the data from the standard and tranisient approaches are compared. Thus the feasibility of using a transient load to measure

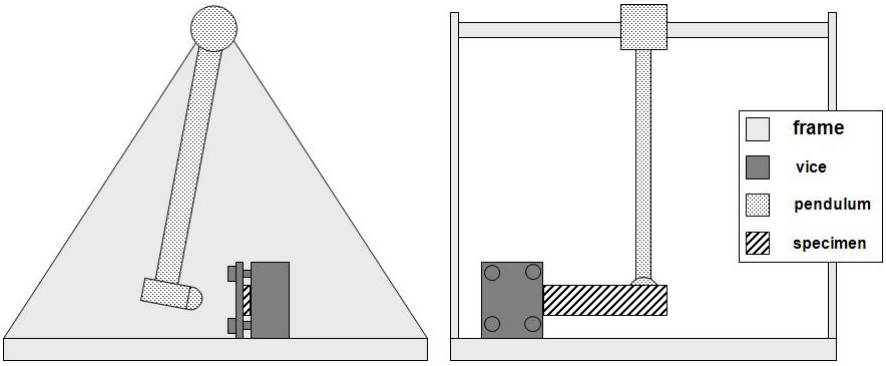

Figure 7.2: Schematic of the impact test jig

the effects of damage can be demonstrated. The comparison with the standard TSA approach at each stage serves as a benchmark against which to evaluate the success of the new technique.

To obtain the thermoelastic data from the infrared detector it is necessary to collect thermal images from test specimens as they are subjected to the transient loading. The temperature was recorded from approximately one second before the application of the load and for approximately one second after at a frame rate of 383 Hz.

In the step load test the stress field in the specimen and therefore the temperature change field is uniform. Temperature measurements were obtained from a selected area of uniform temperature to give an average surface temperature (T) as shown in Figure 7.3a. The measurement area was 15.5 x 26 mm (30 x 50 pixels) in size. In the impact test the stress varies along the length of the specimen, so transverse lines 20 mm long (40 pixels) were plotted at 10 mm intervals along the length of the specimen, shown in Figure 7.3b. The average value of temperature from each line plot was used to give T at positions x1 to x8 along the length of the cantilever beam.

A typical plot of the surface temperature during a step load test is shown in Figure 7.4. ΔT (the thermoelastic temperature change) was determined as the difference between the initial and final temperatures (T_1 and T_2), taken to be average values from 50 frames of data just either side of the change in temperature. (Note that a positive, i.e. tensile change in stress results in a negative change in temperature.) In the impact test (a typical plot is shown in Figure 7.5) T_1 was also taken as the average of 50 frames of data, but in this case T_2 was taken as the maximum value of the temperature spike. (The measurement was taken on the compressive side of the beam and hence the impact results in a positive temperature change.) The noise in the measurement of ΔT is therefore expected to be larger than for the step method since there is no time averaging of T_2 and a reduced spatial averaging of only 40 sampling points.

This simple combination of temporal and spatial averaging was used to filter the detector output. For example, if the noise were of a Gaussian distribution, 50 sample points would reduce the noise by a factor of 7, as Gaussian 'white' noise decreases as the root of the sample size, to give approximately 2.5 mK or one half of the detector

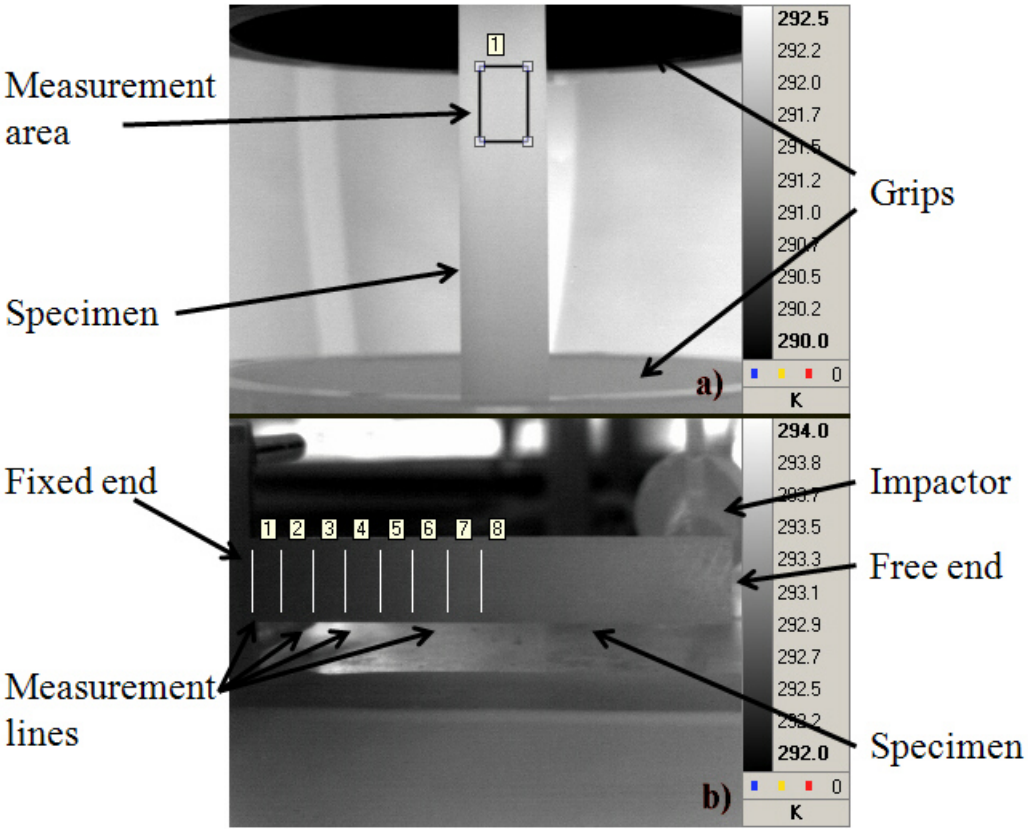

Figure 7.3: Thermal images of a) a step load test and b) an impact test, showing the positions (area 1 and lines 1 to 8) at which temperature measurements were taken

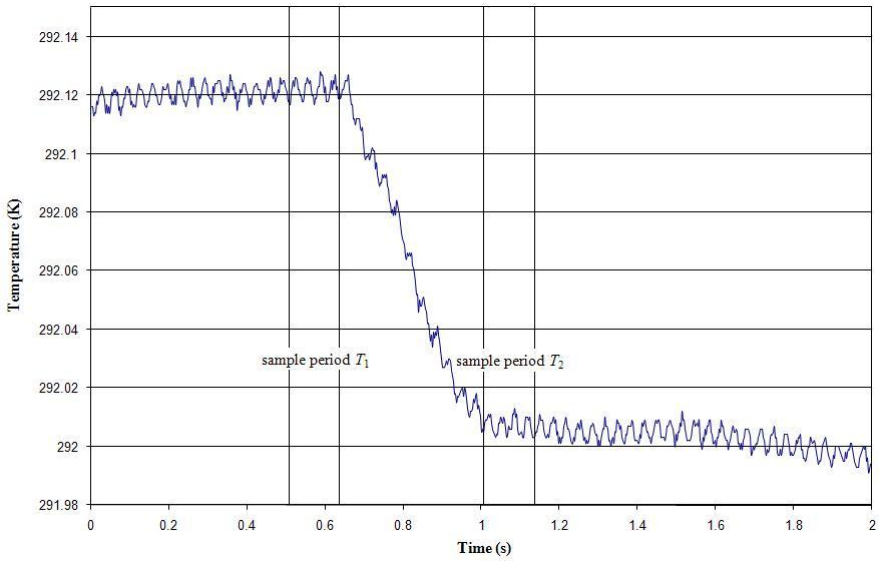

Figure 7.4: Change in temperature during a step increase in load in a uni-axial tensile specimen

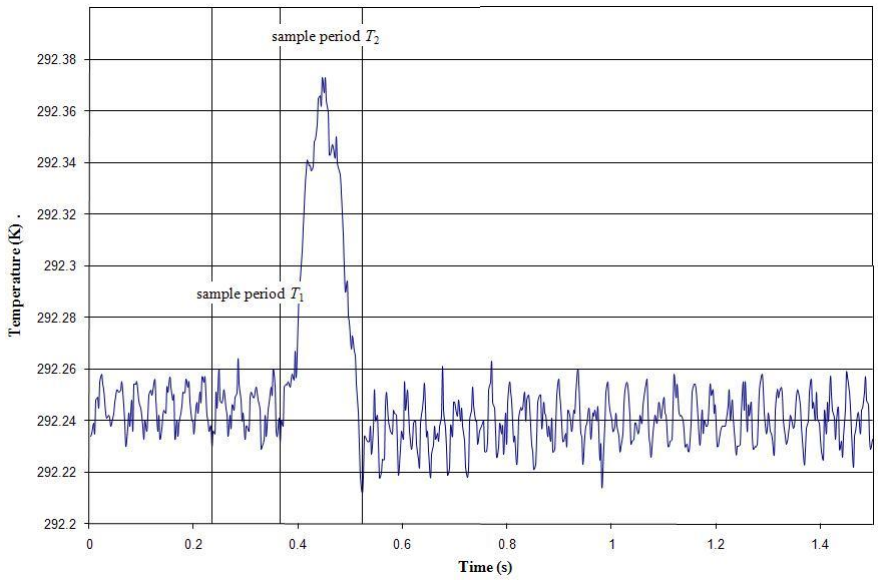

Figure 7.5: Change in temperature during a cantilever impact test

sensitivity.

It can be seen in Figure 7.4 that the response to the step load contains noise with a distinct frequency. The sampling period of 50 frames for T_1 was selected to span a complete number of oscillations, thereby eliminating error associated with averaging over incomplete cycles. The noise is further reduced by the spatial averaging of T, sampled over approximately 1500 points for the step load test and approximately 40 points for the cantilever test. In line with the discussion in the introduction this would give a thermal resolution approximately equal to the detector sensitivity, equivalent to a stress resolution of 3 to 4 MPa. Due to drift in the surface temperature over time, the sample period needs to be kept suitably short. At a detector frame rate of 383 Hz, 50 frames span a period of 0.19 seconds and it can be seen from Figures 7.4 and 7.5 that the average temperature is nearly unchanged over this time period.

7.3 Test specimens

Four materials have been used in this work, two pre-preg laminates and two resin infused woven rovings. The fibre configuration, stacking sequence and manufacturing process are given in Table 7.1. Glass-epoxy composites were used as they have a low thermal diffusivity, which means that heat transfer is minimised, hence providing a good basis for assessing the trasient loading aproach.

The unidirectional pre-preg autoclave consolidated material was chosen for two of the specimens (UD and LAM) as autoclaved pre-preg provides the most consistent material properties and best fibre alignment (as discussed in Chapter 2). The pre-preg material (manufactured by Primco) was cured in an autoclave at 125 °C and 3 bar pressure. The (UD) specimen also has the advantage that the opportunity for heat transfer is reduced further as both the in-plane and through thickness stresses are uniform. The only heat

transfer that might take place in this specimen is between the fibres and the resin at the micro-scale, which will not be visible because of the scale of the measurement. The second configuration (LAM) is a $[0, 25, -25, 0]_S$ laminate. The configuration was developed in reference [86], as the $\pm 25°$ plies were found to encourage delamination under bending loads. Therefore this configuration will be studied without delamination for the validation (see boxes 1 and 2 of Figure 7.1) of the study and with delamination for the damage assessment (see box 3 of Figure 7.1). For both the UD and LAM materials the stress state in the surface ply can be calculated using CLT thereby enabling the calculation of ΔT in the surface ply of the specimens and comparison to the experimentally derived values in the validation part of methodology (see boxes 1 and 2 of Figure 7.1).

The third material type is a plain weave textile composite (WR) that was manufactured by resin infusion with the same $[0, 25, -25, 0]_S$ stacking sequence. The resin was Prime 20 LV with a fast hardener manufactured by Gurit. The consolidation was by liquid resin infusion at room temperature (approximately 20 °C) and atmospheric pressure. The aim was to produce a woven composite with the same favourable delamination behaviour as the pre-preg material for the damage assessment study. The fourth material is a 2 x 2 twill woven composite (TW) with a coarser weave than the plain weave material, manufactured with the same resin and identical procedure to the WR. This was included to investigate if the influence of the weave pattern on the stress field could be detected using the transient TSA methodology. Local variations in the stress field in the woven materials prevent a simple calculated solution for the stresses from being formulated. Therefore it was decided to use these materials only in the damage assessment (see box 3 of Figure 7.1).

Material properties for calculating the thermoelastic response based on the known stress in the surface ply were measured using samples of the UD material. The Young's moduli (E_1 and E_2) were obtained from quasi-static tensile tests according to ASTM standard D 3039. The coefficients of thermal expansion (α_1 and α_2) were measured using a strain gauge technique described in reference [119] over the range from 20 to 40 °C. The density (ρ) was measured using microscope images of the material cross-section from several regions cut from a UD specimen and the specific heat capacity (C_p) was measured using digital scanning calorimetry (DSC). The material properties are summarised in Table 7.2.

Table 7.1: List of materials and manufacturing processes used in this chapter

Specimens	Resin	Reinforcement	Lay-up	Process
UD	(Epoxy)	UD fibre	8 (7) plies, 0^o	pre-preg$^{(*)}$
LAM	(Epoxy)	UD fibre	$[0, 25, -25, 0]_S$	pre-preg$^{(*)}$
WR	Prime 20 LV with fast hardener	plain woven roving $\sim$ 300 gm^{-2}	$[0, 25, -25, 0]_S$	VARTM$^{(**)}$
TW	Prime 20 LV with fast hardener	2 x 2 twill woven roving $\sim$ 500 gm^{-2}	6 plies, 0^o	VARTM$^{(**)}$
*	Autoclave consolidated pre-impregnated glass fibre matt			
**	Vacuum Assisted Resin Transfer Moulding			

Table 7.2: Material properties of the E-glass / epoxy pre-preg

	Property	Value		
E_1	(GPa)	34	.	2
E_2	(GPa)	10	.	0
ρ	(kg m^{-3})	1880		
C_p	(J kg^{-1} K^{-1})	843		
α_1	(K^{-1})	9	x	10^{-6}
α_2	(K^{-1})	31	x	10^{-6}

To achieve a matt surface finish, the surface was lightly abraded by hand using a medium grade 3M Scotch-Brite scouring cloth in the same way as in Chapters 5 and 6.

7.4 Transient load validation

7.4.1 Procedure 1

Procedure 1 involved the step load test and the standard TSA test (see box 1 in Figure 7.1). To enable direct comparison between measured and calculated TSA data, the data was converted into a non-dimensional form by taking equation (3.3) (ignoring the shear term) and dividing through by the specimen static temperature (T_1 in the step and impact methods). The calculated non-dimensional temperature change is then given by:

$$\left|\frac{\Delta T}{T}\right| = \frac{1}{\rho C_p}\left(\alpha_1 \Delta\sigma_1 + \alpha_2 \Delta\sigma_2\right) \tag{7.1}$$

Tests were conducted using the UD and the LAM specimens. Using the material properties in Table 7.2, the stress state in the surface ply was calculated for six different applied loads corresponding to the stress range in the standard test and the magnitude of the stress change in the transient tests. These varied from 20 to 80 MPa in increments of approximately 12 MPa. To further ensure comparable loading conditions the mean stress was held constant in all the tests. Tests using the standard TSA method were conducted at loading frequencies of 20 Hz (typical test parameter) and 2.5 Hz (comparable to the loading rate of the step load test). Temperature data were collected from the same area of the specimen in each test and the corresponding non-dimensional temperature change was then obtained using equation (7.1). For the step load method a set of five measurements were obtained at each stress change increment.

Figures 7.6 and 7.7 show $\Delta T/T$ data for the UD and LAM specimens respectively for the two standard TSA cases, the step load case and the calculated value of $\Delta T/T$ in the surface ply. For both specimens the standard TSA test at 20 Hz shows good correlation with the calculated values, with a standard deviation in each data point of 1 to 3%. The calculations over predict the measured temperature change from the 20 Hz standard test by approximately 6% for the UD and 4% for the LAM material. The better correlation of the LAM material with calculations may be attributed to small differences in the surface preparation, and a corresponding discrepancy with the emissivity value used in

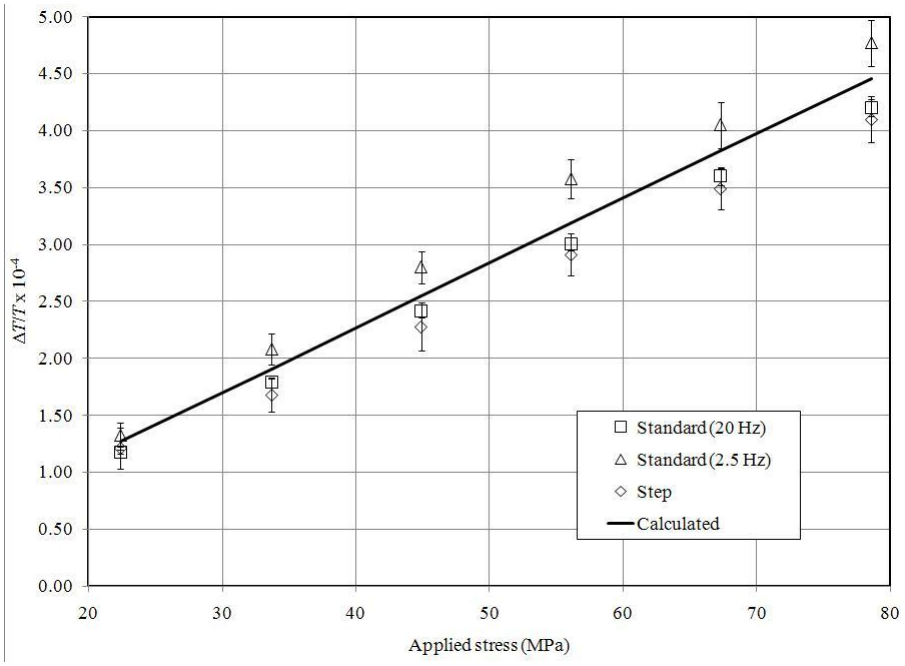

Figure 7.6: Comparison of the non-dimensional thermoelastic response from the UD specimen at different loading amplitudes obtained using the standard and step loading methods

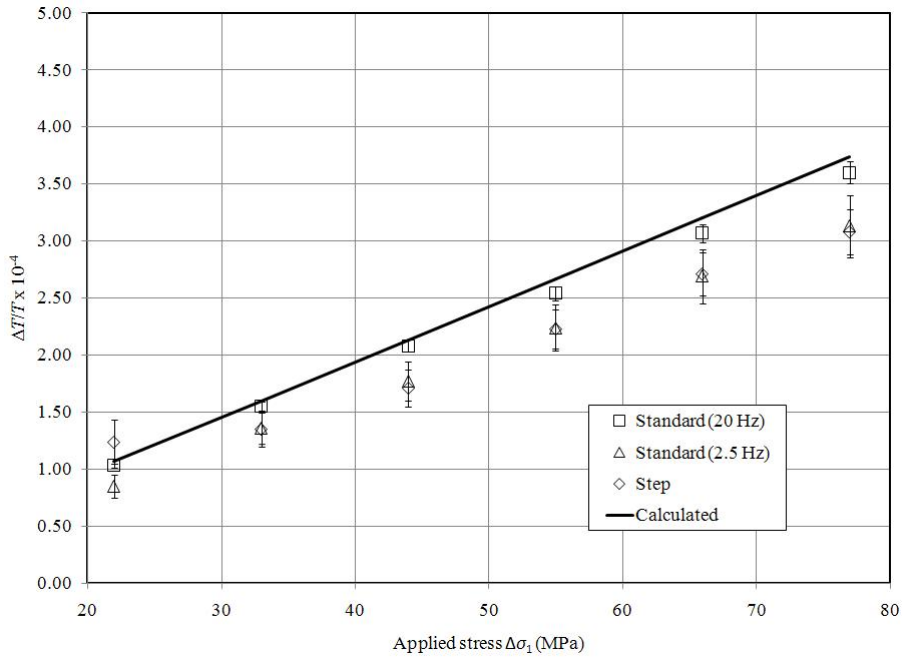

Figure 7.7: Comparison of the non-dimensional thermoelastic response from the LAM specimen at different loading amplitudes obtained using the standard and step loading methods

the thermal calibration of the IR data. As done previously in Chapters 5 and 6, a value of 0.92 was used for all measurements on the basis of a comparison between two regions of a specimen, one uncoated and one coated with a thin layer of RS matt black paint with a known emissivity of 0.92. Alternatively the small discrepancy could be attributed to errors in the mechanical or thermal material properties (i.e. the density, specific heat capacity and CTE) used in the calculations.

When the loading frequency is reduced to 2.5 Hz, Figures 7.6 and 7.7 show the correlation between the measured data and the calculated data is not as good as that collected at 20 Hz. The experimental data from the UD material is found to lie between 5 and 12% above the calculated values while the experimental data from the LAM material lies between 15 and 20% below. The standard deviation within each data point is 5 to 8% for the UD material and 8 to 12% for the LAM material as indicated by the error bars. The only explanation for the larger experimental value from the UD material is an anomaly in the testing. While all tests were conducted in load control, the position amplitude readout at 2.5 Hz was noted on several occasions to be 1% higher than at 20 Hz. The same discrepancy was not noted during the LAM tests. The larger variability in the 2.5 Hz standard TSA measurement compared with the test at 20 Hz can be explained by a decrease in the number of loading cycles included in the TSA measurement; the sampling frequency was kept constant at 383 Hz for all tests, and the sampling duration was approximately 5 seconds for both standard tests.

The step load test, for which only the equivalent of half a loading cycle is available to obtain the measurement, shows a further increase in the standard deviation. At the lowest applied stress change of 22 MPa, the standard deviation is approximately 15% for both materials. This decreases to less than 10% for a stress change of 40 MPa, which is comparable to the 2.5 Hz standard test. The tests therefore indicate a lower threshold in transient loading and indicate that a larger applied stress is necessary to obtain a reliable measurement.

The consistently lower values of experimental data compared with the calculations can, in the case of the LAM material, be partially explained by heat transfer between the 0° ply at the surface and the 25° ply below. The stress gradient between the two plies leads to a corresponding temperature gradient (0.010 K mm^{-1} to 0.035 K mm^{-1}). At the reduced loading frequency non-adiabatic conditions result in a reduced thermoelastic response at the surface. Some heat dissipation to the surroundings will also occur, but this is considered to be negligible at the applied loading rate.

The data clearly indicate that accurate measurements can be obtained using the step load method. The sampling period and the ability to filter the IR data limit the precision of the technique. The minimum required stress change is however slightly higher than predicted. For the technique to be feasible in the field, the method of imparting a load into a component must allow a fast transient which is capable of producing a sufficiently large stress change. In the case of E-glass / epoxy, the minimum stress amplitude needs to be in the range of 40 to 50 MPa, which still lies well below the failure limit of the

material.

7.4.2 Procedure 2

Procedure 2 involved the use of a cantilever beam and comparison with calculations, as shown in Figure 7.1. The stress field in the cantilever beam was calculated using simple cantilever beam theory and the measured maximum deflection. In the case of the UD material, the force (P) at the free end of the beam in a static case can be related to the deflection (δz) by:

$$P = \frac{3\delta z E_1 I}{l^3} \tag{7.2}$$

where I is the second moment of area, E_1 is the Young's modulus in the longitudinal direction and l is the distance from the fixed end to the point at which the force acts. Using the measured deflection, equation 7.2 was used to provide a first an estimate of the force at the free end of the beam at the maximum deflection. This could then be used to calculate the stress in the surface ply at any distance (x) from the fixed end using:

$$\sigma_x = \frac{P(l-x)z_0}{I} \tag{7.3}$$

where z_0 is half the thickness of the beam. In this case $\Delta\sigma_1 = \sigma_x$ because the beam is initially unloaded. For the UD material $\sigma_2 = 0$. For the LAM material, $E_1 I$ in equation 7.2 is replaced by the laminate bending stiffness, and instead of equation 7.3, the bending moment at each distance x was taken and CLT was used to calculate σ_1 and σ_2.

As with procedure 1, the impact test was repeated five times for each material, but only for one pendulum release height. The pendulum release height was selected to produce a surface ply stress of approximately 80 to 100 MPa at the clamped end to ensure a measureable temperature change in line with the results from procedure 1. The results are shown in Figure 7.8 for the UD material and Figure 7.9 for the LAM material. Notably the experimental data lies below the calculated data by approximately 10% at the fixed end. The experimental data from both the UD and the LAM specimens show a slightly steeper stress gradient at the fixed end than the calculations. At approximately 20 to 30 mm from the fixed end this then becomes nearly parallel to the line of calculated values.

The uncertainty regarding the emissivity and properties of the material is not sufficient to explain the discrepancy shown in Figures 7.8 and 7.9. However, two further effects may explain the lower experimental values. Firstly, bending theory assumes an infinitely stiff clamped end, so flexibility in the clamped end would result in a lower stress, or a longer effective beam length. Secondly, the thin beams have a large through-thickness stress gradient. Although it has been shown that temperature dissipation between plies in specimens loaded in uniaxial tension can be neglected in E-glass /

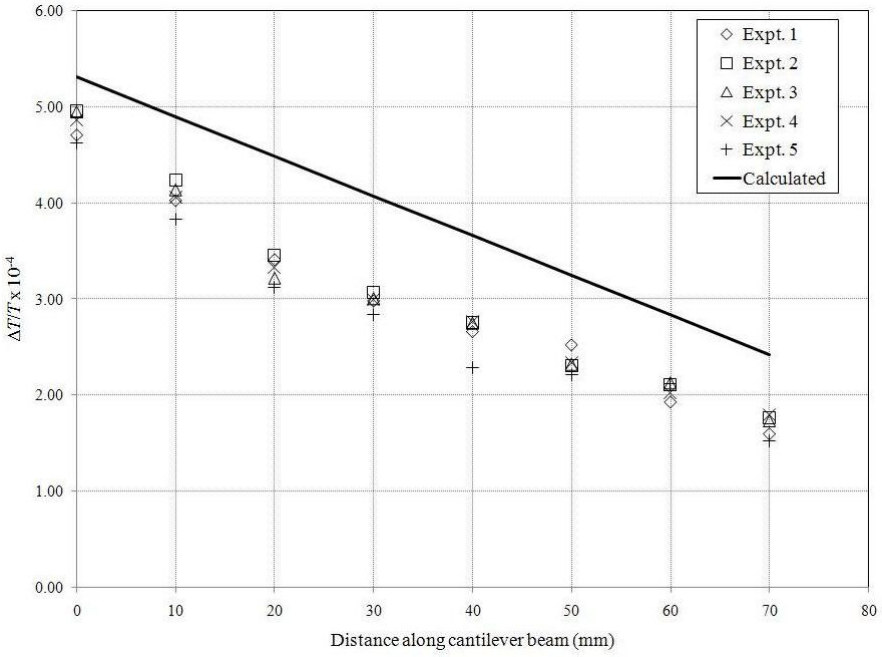

Figure 7.8: Stress distribution in cantilever beam UD, deflection 17.5 mm

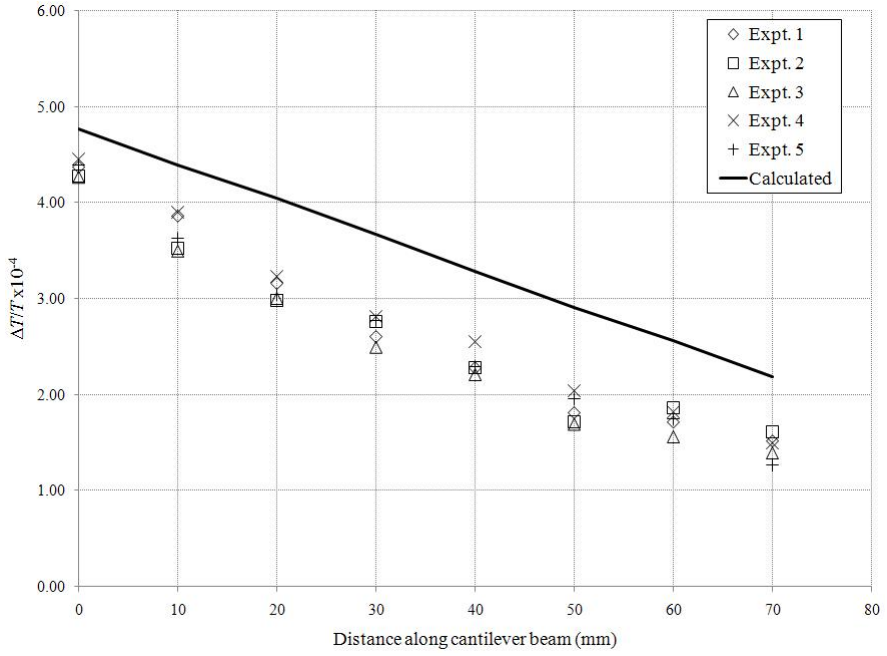

Figure 7.9: Stress distribution in cantilever beam LAM, deflection 18.2 mm

epoxy specimens even at low loading rates [89], large stress gradients exist not only between plies, but also within each ply; the stress in the outer surface of the outer ply of the LAM specimen is 25% greater than the stress at its inner surface. The average surface ply stress is therefore 13% lower than the surface stress, accounting for a large portion of the discrepancy with the calculations in which the surface stress was used. Furthermore, the stress gradient between the plies is much greater in the bending case than in the uniaxial tension case, and hence some non-adiabatic behaviour between the sub-surface plies may influence the surface temperature change as well. Taking this into account, the calculated and measured stress data correlate very well.

The results from the two validation tests indicate that the modified TSA procedure is a valid approach that can be applied to obtain quantitative measurements. The precision is lower than for a standard test conducted at a higher frequency, and hence the minimum stress change required to obtain a reliable measurement is greater. Also, non-adiabatic effects are an important consideration, particularly if the rate of loading is low, as in the examples shown in this work.

7.5 Application to damage assessment

The spatial averaging used in the previous section to improve the effective thermal resolution is not practical for the purpose of damage assessment for which full-field data is desired. In the following tests, the method of obtaining ΔT was as described in section 7.2, except that the temperature measurement was taken on a pixel by pixel basis to provide an image of the $\Delta T/T$ field.

Damage assessment was conducted on three material types, LAM, WR and TW. Two types of specimen were used: two tensile strips as described in section 7.3 made from the LAM and TW materials, and two plate specimens, nominally 250 x 100 mm, made from the LAM and WR materials.

The tensile specimens were loaded using the step method (LAM) and the impact method (TW). A stress concentration was introduced in the form of a 4 mm diameter hole in the centre of the strip. The specimens were then subjected to a tensile sinusoidal load at constant load amplitude (giving a far field stress of 230 MPa for specimen LAM and 180 MPa for specimen TW) for two sets of 18000 cycles at 2 Hz (specimen LAM failed after 26500 cycles) and a TSA measurement was taken after each set. TSA measurements of both specimens were taken using a stress change of approximately 70 MPa in the far field at 20 Hz.

Figure 7.10 shows non-dimensional standard TSA data from LAM with no damage (step 1), after zero fatigue cycles but with the stress raiser (step 2), after 18000 fatigue cycles (step 3) through to failure (step 4). At step 4, only a narrow band along the right hand edge of the specimen was still intact, allowing the final TSA measurement to be taken. All TSA data was obtained at the same load amplitude. The corresponding TSA data obtained using the step method is shown in Figure 10b. Note that the standard

data gives only a magnitude and hence the compressive regions above and below the hole show up as positive values. In the step data, which is a simple difference between T_1 and T_2, these regions show a negative temperature change.

Up to step 3, the standard and step method data is very similar. However, at step 4 a very large difference between the standard and step methods is plainly visible. This is due to frictional heating in the damaged regions which accumulates a net increase in the absolute specimen temperature due to the cyclic load. Although this should be accounted for in the non-dimensional data in which ΔT is normalised against the absolute surface temperature, in the example shown in Figure 7.10(a), the heating is so great that the surface temperature exceeds the detector calibration range. By decreasing the detector exposure time, the range can be increased, however, at the expense of a loss in sensitivity. Furthermore, the magnitude of the localised heating may not be known *a priori*.

Using the step load method, the effect of local heating is eliminated because the heat generation is transient and does not have the opportunity to 'accumulate' in the specimen and cause large temperature evolutions. As a consequence, localised heating is minimised. Therefore the remaining load bearing section of the specimen is easily identified in step 4 of Figure 7.10(b) along its right hand edge. This result demonstrates that the application of a transient load for TSA based damage assessments can provide advantages compared with the standard method.

The TW specimen enables a qualitative evaluation the resolution of the TSA transient loading methodology, as the interlacing of the fibres in the textile results in stress concentrations at a small scale. Fatigue of the textile composite leads to a change in the distribution and magnitude of these stress concentrations, as shown in Chapter 6. The aim here is therefore to verify if such fine details in the stress field can be resolved using the modified TSA method.

Damage was introduced and progressed in the same way as for the LAM specimen except that the specimen did not reach ultimate failure. The data in Figure 7.11 shows that the stress concentration around the hole can be identified using the impact method. The deterioration in the weave structure is however not picked up by the impact method to the same extent as by the standard method. A slight decrease in the magnitude of the signal, in particular towards the free end, can be identified. This data shows that further refinement of the technique will be necessary in order to enable small scale features in the stress field, such as the influence of the weave, to be identified using the impact method.

Next the two plate specimens were tested. The aim of this test was to investigate a more realistic damage case. Delamination damage was introduced into the specimen using the bending rig shown in Figure 7.12. The rig was developed in [86] based on a design by Drew and White [122]. The curved edge of the clamp introduces a stress concentration in the centre of the plate resulting in a delamination between the $\pm 25^\circ$ plies. Because a glass fibre epoxy composite was used, it was possible to identify the

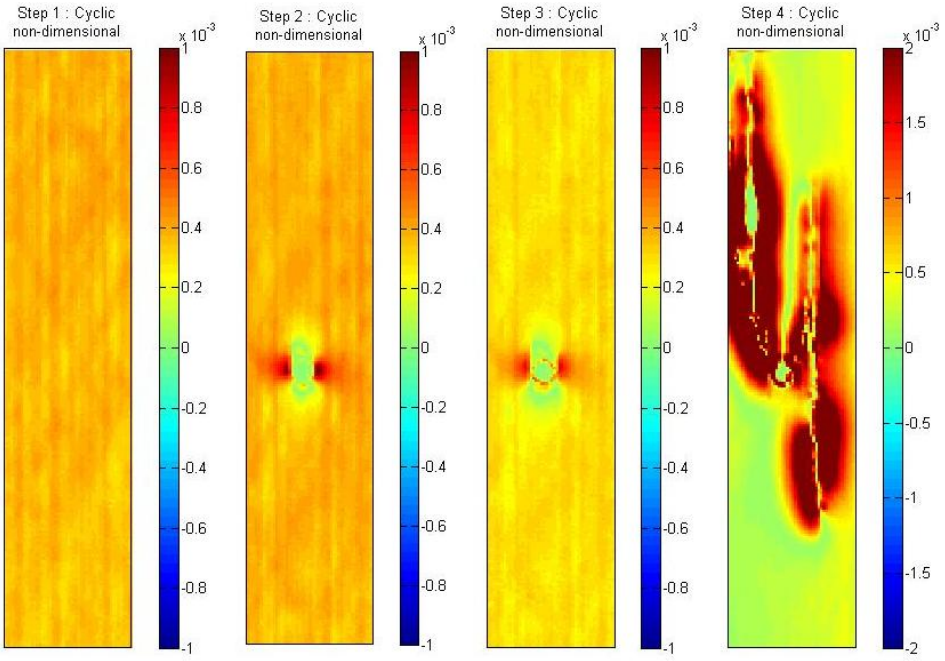

(a)

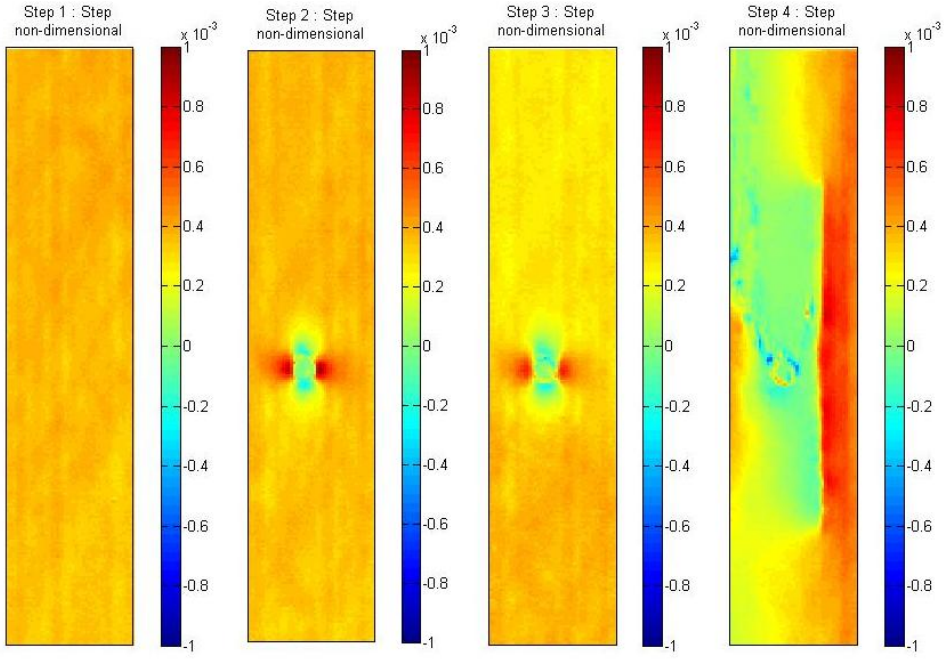

(b)

Figure 7.10: Progression of damage around a hole in the LAM material using a) the standard method and b) the step method ($\Delta T/T$)

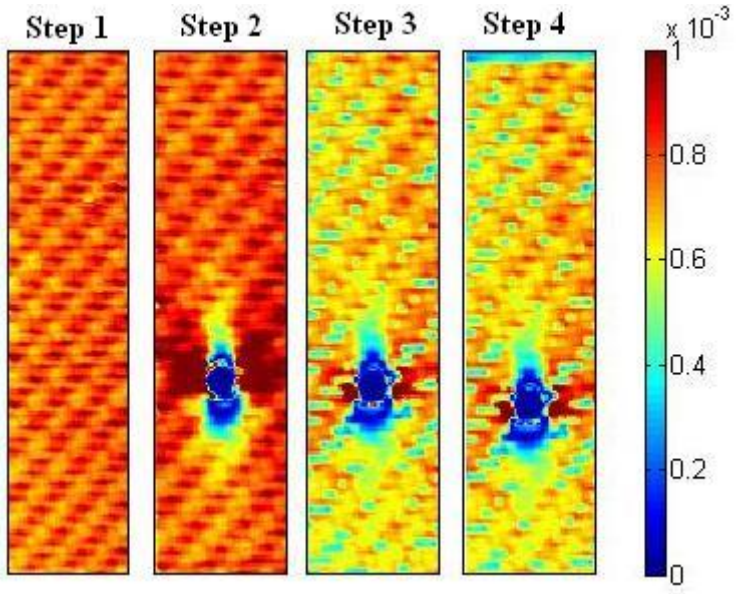

(a) standard method

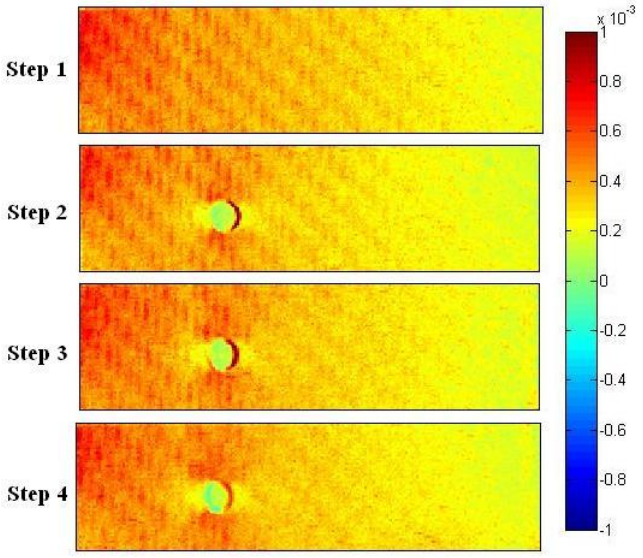

(b) impact method

Figure 7.11: Progression of damage around a hole and within the weave structure in the TW material

damage in the two specimens by visual inspection. The damage is shown in Figures 7.13a) and b) for the LAM and WR specimens respectively. In the LAM material a significant delamination was obtained after 26500 cycles. The displacement amplitude of the actuator, shown in Figure 7.12, was 35 mm at a distance of 75 mm from the clamped end. In the WR material, damage was limited to the surface ply as a result of the contact with the clamp, but no delamination was observed, even after 36500 cycles under the same loading conditions as the LAM material. The damage in the plate specimens was then examined using TSA: firstly by testing in tension using the standard and step methods and then using the impact method. For the impact tests, the plates were cut into 25 mm wide strips such that the damaged region was 20 mm away from the clamped end of the cantilever specimen.

Figures 7.14 and 7.15 show the TSA data obtained from the tensile tests using the standard (Figures 7.14a) and 7.15a)) and step (Figures 7.14b) and 7.15b)) methods. The surface damage can be identified in both materials, more clearly in the WR material which had more significant surface damage. The extent of the delamination in the LAM material cannot be identified in the data from either the standard or the step methods. This implies that a delamination does not influence the stress field in a laminate under in-plane tensile loading and can therefore not be detected by this method. The test does however show that localised fibre breakage in the surface ply (as in the LAM material) can be identified using the step method, although this damage is more clearly visible using the standard method. In both the LAM and the WR materials, the surface damage appears as an area of reduced thermoelastic response. This indicates that the load is being diverted away from the surface ply and into the plies below. Unlike the TW specimen the weave pattern in the WR specimen is not apparent in the data because of the small scale of the weave and the resolution of the detector settings.

The impact test was then conducted to investigate if the delamination damage could be identified in bending. The data from the LAM and WR materials is shown in Figure 7.16a) and b) respectively. The data is taken from the compressive side of the specimen where localised buckling might reveal the delamination. However, it is clear from Figure 7.16 that this is not the case. The data shows only the surface damage. It is however promising that the resolution is comparable to that obtained using the standard and step methods. Also, the asymmetry in the clamping conditions of the LAM specimen can clearly be identified in Figure 7.16a).

The above investigations of damage progression in a variety of composite materials demonstrate that the modified TSA method has potential to provide information on the stress field in a component in situations where a cyclic load is impractical. This can be due to limited access to loading machines, as might be expected outside of the laboratory environment, but also due to the presence of defects that cause localised heating under cyclic loading. The technique also enables greater flexibility in the types of loading scenario to which a component can be subjected, allowing the extent to which damage in the component influences the stress field in a particular loading case, to be

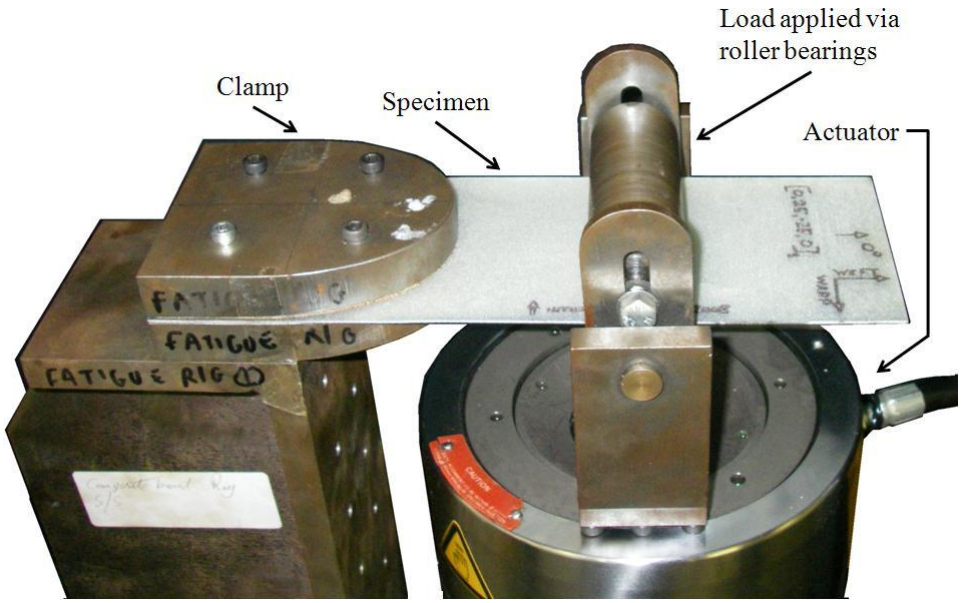

Figure 7.12: Fatigue loading rig used to introduce damage to the plate specimens

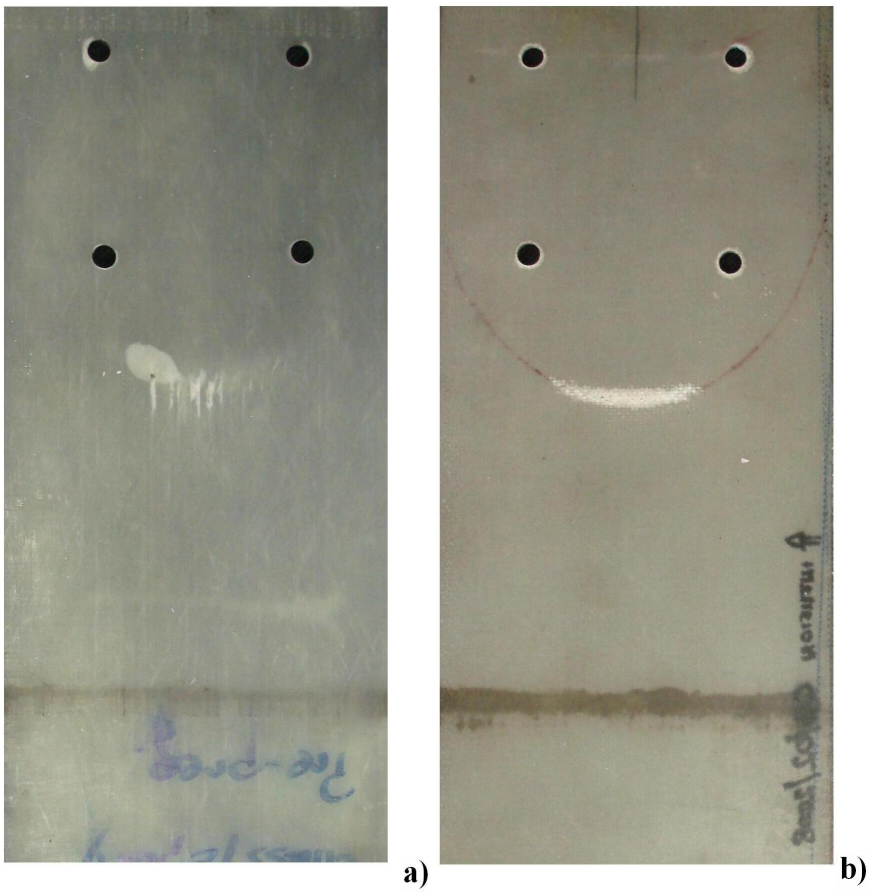

Figure 7.13: Damage location in a) LAM and b) WR plate specimens

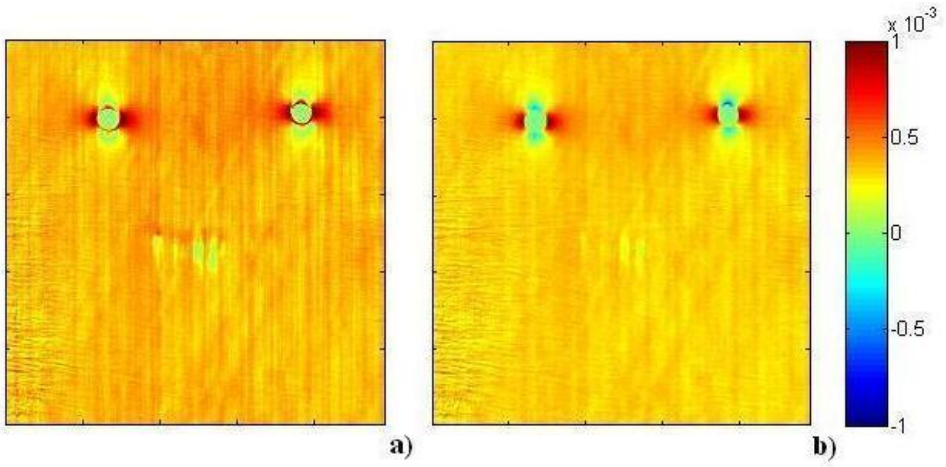

Figure 7.14: Non-dimensional TSA data from damaged LAM plate obtained using a) the standard and b) the step load methods

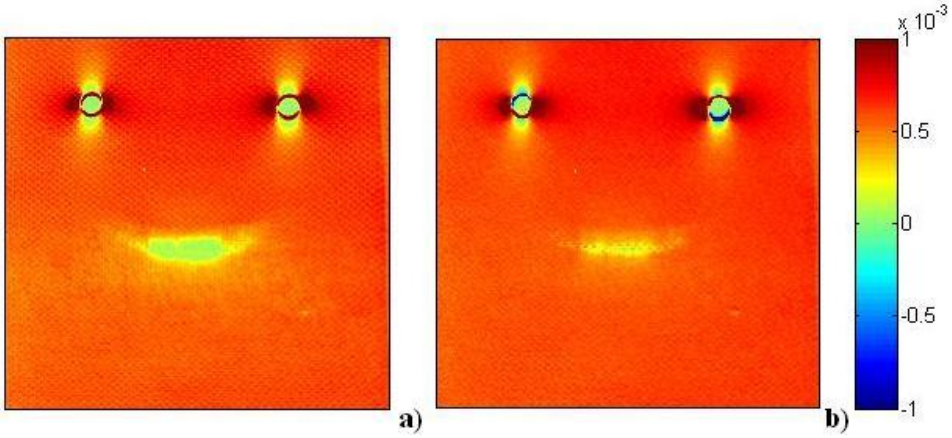

Figure 7.15: Non-dimensional TSA data from damaged WR plate obtained using a) the standard and b) the step load methods

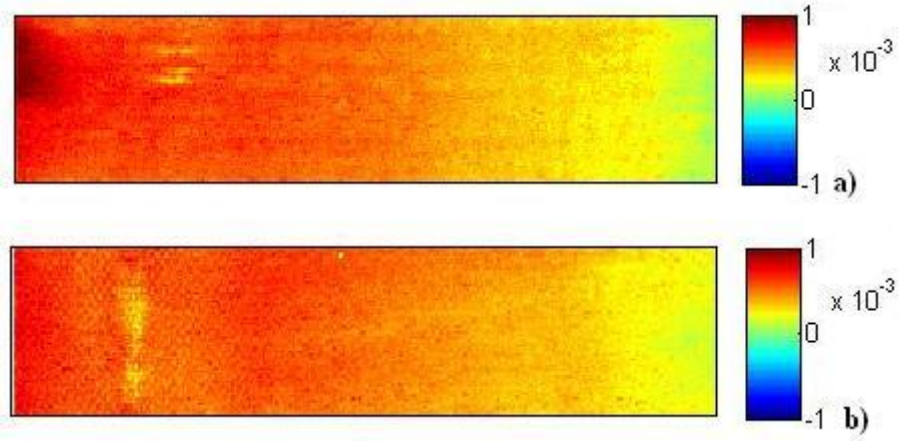

Figure 7.16: Non-dimensional TSA data obtained using the impact method from damaged a) LAM and b) WR materials

assessed. Further work is required to improve the thermal / stress resolution of the modified technique. Although the general stress field is well captured, finer details in the stress field may not be resolved by the modified method.

7.6 Summary

The results show that quantitative data can be obtained using a single transient load with a comparable accuracy to the standard TSA method. However, the precision of the measurement is lower, and hence the small scale effects such as those described in Chapter 6 may not be identifiable using the current methodology. The rate and magnitude of the stress change must exceed a minimum threshold which will vary depending on the material. In the case of E-glass / epoxy composites, relatively low loading rates and magnitudes are sufficient.

With regard to the identification of damage, the technique relies on a stress redistribution in the surface ply. This is no different from the standard method. However, the greater simplicity of the modified technique provides improved flexibility for introducing load into the specimen. The greatest difficulty will always be to generate a realistic loading scenario, and a sufficient load amplitude. Development of the filtering of the thermal data to improve the effective thermal resolution of the technique is required to enable small scale stress concentrations to be identified; these challenges will be the object of future work. The present study has confirmed the feasibility of applying TSA as a damage assessment technique for in-service components. The work represents an important initial step in taking the TSA technique away from the laboratory and opens a new application range of significant industrial relevance.

Chapter 8

Conclusions

In this work, the application of TSA to woven composite materials and its use as an NDE tool have been studied. The motivation for the work was the need to establish TSA as a tool for the assessment of woven composite structures, and to use it to identify the presence and severity of damage. The main body of the work can be divided into four parts:

1. the introduction of a new TSA system,
2. the investigation of the thermoelastic response from a woven composite material,
3. the study of fatigue damage development in a woven composite material,
4. the application of TSA by means of a single transient excitation.

The main findings from each of these areas are sumarised below.

8.1 Introduction of a new TSA system

A commercially available IR system with TSA functionality has been tested in this work. It differs from previous systems in that it is radiometrically calibrated, features relatively high frame rates and incorporates a motion compensation routine. In this work it was demonstrated that:

- The piecewise linear approximation of the detector calibration leads to errors in the measurement of ΔT near the calibration sampling points. This can be circumvented by avoiding taking measurements at these temperatures. Alternatively, it can be overcome by fitting a smooth curve through the calibration sampling points and applying the calibration separately.
- When applying TSA at high spatial resolutions, motion due to the straining of the material results in spurious measurements. The presence of a contrast (i.e. variation in emissivity) on the surface of the specimen enables the motion to be compensated, and hence accurate data to be obtained.

8.2 The thermoelastic response from a woven composite material

The thermoelastic response from woven composite materials was considered in terms of a simple mosaic model. A detailed investigation of the material properties and their effect on the thermoelastic response at different fibre orientations was conducted. It was demonstrated that:

- The thermoelastic response from an FRP material is strongly dependent on the material composition and hence on the manufacturing method. Careful determination of material properties for the specific material used is essential since literature values cannot be generally applied.
- The presence of a surface resin layer influences the thermoelastic response from an FRP material. However, the non-uniform nature of this layer means that it cannot reliably be used as a strain witness. The manufacturing process, and the type of surface ply influence the thickness and regularity of the surface resin layer.
- Comparison between the 2D mosaic model and a 3D FE model show that the complex 3D strain field manifests itself strongly in the thermoelstic response. The mosaic model is therefore not able to correctly predict the thermoelastic response from a woven material. It does however provide a basis from which to assess deviations from the global average strain field.

8.3 Fatigue damage development in woven composite materials

The development of fatigue damage in woven composite materials subjected to tension - tension fatigue cycling was studied. The global mean peak stress of the loading cycle was kept below 20% of the failure stress of the material. Two methods of analysing the TSA data were employed. The first was a comparative method in which two images, taken before and after the specimen had been subjected to fatigue cycling, were inspected for differences. The second method used the phase data to identify the presence of damage directly. Optical microscope images of the specimen cross-section where used to coroborate the TSA findings. It was demonstrated that:

- Damage in single ply woven composites can initiate and grow at stress levels as low as 10% of the global failure stress. However, the damage does not propagate to the point of ultimate failure at these load levels.
- Damage initiates as matrix cracks in the transverse yarns. These grow in-plane and through the thickness until they reach the longitudinal yarns. At the warp / weft yarn interface in the middle of the textile, the cracks turn through 90° and delamination occurs.

- A signature pattern in the TSA data can be used to identify the presence of cracks in the transverse fibres either by means of a differential measurement or directly from the phase data.

8.4 TSA by means of a transient excitation

To facilitate the application of TSA outside of laboratory conditions, the use of a simplified means of introducing the load into a component was investigated. This took the form of a single step load in a standard tensile specimen and a single impact load applied to a cantilever beam specimen. It was demonstrated that:

- A minimum applied stress change in the range of 40 to 50 MPa is required to enable a useful TSA reading to be obtained from a single transient excitation.
- The identification of damage is limited to damage that directly influences the surface stress field, since with the application of only a single transient load, heat generation at the damage site and the subsequent disturbance of the mean surface temperature, cannot be measured.
- The feasibility of applying TSA to assess damage outside of laboratory conditions was confirmed.

The work described in this thesis has thereby demonstrated, on the example of woven composite materials, that TSA can be applied to the study of hetergenous materials. The richness of the IR signal allows the data to be analysed in a variety of ways, enabling the identification of a range of damage mechanisms. The use of a simplified loading methodology for out-of-laboratory application of the technique has been shown to be feasible. The study thereby represents a significant step towards improving the understanding of the TSA technique and increasing its range of application.

Chapter 9

Recommendations for Further Research

The outcomes of the work described in this thesis open the path for further research in the development of TSA. Four areas of further work have been identified as having imediate relevance to the further development of TSA. These are described briefly below.

The use of TSA at high spatial resolutions implies short heat dissipation lengths. In the study of the meso- and micro-scale thermoelastic response, heat transfer is therefore an important consideration. In the current work, this issue was circumvented by applying the cyclic loads at 'high' frequencies. The use of a low conductivity material helped to reduce the minimum required frequency. In the current study, the limits of the servo-hydraulic testing machine were reached in order to approximate adiabatic conditions. However, when using materials with higher conductivity, such as carbon fibre composites, it may not be possible to apply a sufficiently high loading frequency to achieve adiabatic conditions. To better understand the effects of thermal conductivity at small scales, it is necessary to investigate the heat transfer in woven composite materials specifically, using numerical techniques such as FEA. This will be necessary to permit quantitative analysis of data obtained at lower loading frequencies.

In Chapter 7 the use of a single transient excitation for TSA measurement was described. One of the challenges identified was the treatment of noise in the IR signal. To further improve the resolution of the modified technique, improved filtering techniques are required. Spatial averaging, as used in the validation procedures is not desirable since one of the main advantages of TSA is that it provides full field data capture at high spatial resolutions. The investigation of suitable signal filtering techniques is therefore recommended to enable the technique to be applied with greater precision.

The method of imparting a transient load into a structure was very rudimentary, and applicable only to a simple component such as the cantilever beam used in the example. Further refinement of the method for imparting a controlled transient load into a structure is necessary to make the technique more attractive as an NDE tool for industry. Two suggestions include the use of an instrumented hammer, or sonic

excitation. The advantage of the latter technique is that it can be combined with acoustic thermography, which has also been developed for the detection of subsurface damage [123]. While the acoustic thermography technique could be used to identify the location of damage, TSA could be used to evaluate the effect of the damage on the strain field in the component.

In a recent discussion with members from industry, the need for tangible research outputs, such as the development of a user friendly software application was identified. To attain acceptance by industry, it is necessary for any technique to be presented as a tool which incorporates all the details of the methodology and requires the user merely to choose from a set of options depending on the specific application. Hence it is suggested that a user interface, capable of both the standard TSA processing and the modified methodology, is developed.

It is the author's opinion that IR thermography, of which TSA is a subset, has great potential as a tool for evaluating the condition of a wide variety of engineering structures. This potential is currently not fully exploited in an industrial context. The development of TSA as an NDE tool needs to be combined in a package that incorporates other IR inspection techniques as well. These might include acoustic thermography mentioned above and pulsed phase thermography (PPT). In combination, these techniques would enable a much greater wealth of information to be obtained regarding the serviceability of damaged structures. The final recommendation is therefore to consider TSA in the context of IR thermography, and how it might be integrated into a comprehensive IR damage assessment tool.

Appendix A

List of Publications

Journal Publications

- **On the thermoelastic response of woven composite materials**
  R. K. Fruehmann, J. M. Dulieu-Barton, S. Quinn
  Journal of Strain Analysis, **43**, 435-450, 2008

- **Thermoelastic stress analysis using transient loading**
  R. K. Fruehmann, J. M. Dulieu-Barton, S. Quinn
  Experimental Mechanics, accepted for publication

- **Cyclic fatigue progression in single and two ply woven composite materials**
  R. K. Fruehmann, J. M. Dulieu-Barton, S. Quinn
  Composite Science and Technology, submitted for revision

Conference Publications

- **Thermoelastic stress analysis of inhomegenous composite materials**
  R. K. Fruehmann, J. M. Dulieu-Barton, S. Quinn
  13^{th} *International Conference on Experimental Mechanics*, 2007

- **Material properties for quantitative thermoelastic stress analysis of composite structures**
  R. K. Fruehmann, S. Sambasivam, J. M. Dulieu-Barton, S. Quinn
  6^{th} *BSSM International Conference on Advances in Experimental Mechanics*, 2008

- **Material heterogeneity or stress concentration: the thermoelastic response from woven composite materials subjected to cyclic fatigue**
  R. K. Fruehmann, J. M. Dulieu-Barton, S. Quinn
  17^{th} *International Conference on Composite Materials*, 2009

Publications as Contributing Author

- **Thermoelastic assessment of plastic deformation**
  S. Quinn, J. M. Dulieu-Barton, J. Eaton-Evans, R. K. Fruehmann, P. J. Tatum
  Journal of Strain Analysis, **43**, 451-468, 2008

- **In-service TSA of composite structures using transient loading**
  S. Quinn, J. M. Dulieu-Barton, R. K. Fruehmann
  SEM XI International Congress and Exposition on Experimental and Applied Mechanics, 2008

- **Development of thermoelastic stress analysis as a non-destructive evaluation tool**
  S. Quinn, R. K. Fruehmann, J. M. Dulieu-Barton
  17^{th} *International Conference on Composite Materials*, 2009

References

[1] W. G. Roeseler, B. Sahr, and M. U. Kismarton, "Composite stuctures: the first 100 years," in *Proceedings of the 16th International Conference on Composite Materials (on CD)*, 2007.

[2] J. Renton, D. Olcott, B. Roeseler, R. Batzer, B. Baron, and A. Velicki, "Future of flight vehicle structures (2002 - 2023)," *Journal of Aircraft*, vol. 41, pp. 986–998, 2004.

[3] Chair: D. Phipps, "Airbus research and technology requirements: open forum discussion," in *17th International Conference on Composite Materials*, 2009.

[4] A. P. Mouritz, E. Gellert, P. Burchill, and K. Challis, "Review of advanced composite structures for naval ships and submarines," *Composite Structures*, vol. 53, pp. 21–41, 2001.

[5] P. Brøndsted, H. Lilholt, and A. Lystrup, "Composite materials for wind power turbine blades," *Annual Review of Materials Research*, vol. 35, pp. 505–538, 2005.

[6] G. Wood, L. Petrescue, and A. Johnston, "Design and certification of a vacuum-assisted resin transfer moulded composite seaplane float," in *RTO-MP-069(II)*, Nation Treaty Organisation (NATO) Research and Technology Organisation (RTO) Applied Vehicle Technology (AVT), 2003. presented at the NATO RTO AVT Panel Specialists' Meeting, Loen, Norway, 7-11 May 2001.

[7] H. G. S. J. Thuis, "The development of composite landing gear components for aerospace applications," Tech. Rep. NLR-TP-2004-141, Nationaal Lucht- en Ruimtevaartlaboratorium (NLR), 2004.

[8] Q. Yang and B. Cox, "Spatially averaged local strains in textile composites via the binary model formulation," *Transactions of the ASME, Journal of Engineering Materials and Technology*, vol. 125, pp. 418–425, 2003.

[9] U. Meier, "Composite materials in bridge repair," *Applied Composite Materials*, vol. 7, pp. 75–94, 2000.

[10] T. J. Turton, J. Dalzel-Job, and F. Livingstone, "Oil platforms, destroyers and frigates - case studies of QinetiQ's marine composite patch repairs," *Composites - Part A: Applied Science and Manufacturing*, vol. 36, pp. 1066–1072, 2005.

[11] Y. Nagao, Y. Iwahori, Y. Hirano, and Y. Aoki, "Low cost wing structure manufacturing technology program in jaxa," in *Proceedings of the 16th International Conference on Composite Materials (on CD)*, 2007.

[12] O. Rozant, P. E. Bourban, and J. A. E. Månson, "Drapability of dry textile fabrics for stampable thermoplastic preforms," *Composites - Part A: Applied Science and Manufacturing*, vol. 31, pp. 1167–1177, 2000.

[13] S.-P. Ng, P.-C. Tse, and K.-J. Lau, "Numerical and experimental determination of in-plane elastic properties of 2/2 twill weave fabric composites," *Composites - Part B: Engineering*, vol. 29B, pp. 735–744, 1998.

[14] T. Osada, A. Nakai, and H. Hamada, "Initial fracture behavior of satin woven fabric composites," *Composite Structures*, vol. 61, pp. 333–339, 2003.

[15] N. Harwood and W. M. Cummings, eds., *Thermoelastic Stress Analysis*. IOP Publishing Ltd, 1991.

[16] W. Thomson, "Dynamical therory of heat with numerical results deduced from mr joule's equivalent of a thermal unit and m regnault's observation on steam," *Transactions of the Royal Society of Edinburgh*, vol. 20, pp. 261–283, 1853.

[17] M. H. Belgen, "Structural stress measurement with an infrared radiometer," *ISA transactions*, vol. 6, pp. 49–53, 1967.

[18] P. Stanley and W. K. Chan, "Quantitative stress analysis by means of the thermoelastic effect," *Journal of Strain Analysis*, vol. 20, pp. 129–137, 1985.

[19] A. K. Mackenzie, "Effects of surface coatings on infra-red measurements of thermoelastic responses," vol. 1084, pp. 59–71, 1989.

[20] R. H. Owens, "Application of the thermoelastic effect to typical aerospace composite materials," *SPIE: Stress Analysis by Thermoelastic Techniques*, vol. 731, pp. 74–85, 1987.

[21] T. Ishikawa and T. W. Chou, "Stiffness and strength behaviour of woven fabric composites," *Journal of Materials Science*, vol. 17, pp. 3211–3220, 1982.

[22] D. Ivanov, S. Ivanov, S. Lomov, and I. Verpoest, "Strain mapping analysis of textile composites," *Optics and Lasers in Engineering*, vol. 47, pp. 360–370, 2009.

[23] T. R. Emery and J. M. Dulieu-Barton, "Thermoelastic stress analysis of damage mechanisms in composite materials," *Composites - Part A: Applied Science and Manufacturing*, in press.

[24] U. Galietti, D. Modugno, and L. Spagnolo, "A novel signal processing method for tsa applications," *Measurement Science and Technology*, vol. 16, pp. 2251–2260, 2005.

[25] P. Tan, L. Tong, and G. P. Steven, "Modelling for predicting the mechanical properties of textile composites - a review," *Composites - Part A: Applied Science and Manufacturing*, vol. 28, pp. 903–922, 1997.

[26] V. K. Ganesh, S. Ramakrishna, S. H. Teoha, and N. K. Naik, "Microstructural design of textile composites," *Materials & Design*, vol. 18, pp. 175–181, 1997.

[27] P. Vandeurzen, J. Ivens, and I. Verpoest, "A three-dimensional micromechanical analysis of woven-fabric compoites: I. geometric analysis," *Composites Science and Technology*, vol. 56, pp. 1303–1315, 1996.

[28] W. Ruijter, J. Crookston, and A. Long, "Effects of variable fibre density on mechanical properties of a plain weave glass reinforced polyester," in *JAXA Proceedings of the 16th International Conference on Composite Materials (on CD)*, 2007.

[29] P. Xue, X. Peng, and J. Cao, "A non-orthogonal constitutive model for characterizing woven composites," *Composites - Part A: Applied Science and Manufacturing*, vol. 34, pp. 183–193, 2003.

[30] P. Badel, E. Vidal-Sall, E. Maire, and P. Boisse, "Simulation and tomography analysis of textile composite reinforcement deformation at the mesoscopic scale," *Composites Science and Technology*, vol. 68, pp. 2433–2440, 2008.

[31] R. A. Saunders, C. Lekakou, and M. G. Bader, "Compression in the processing of polymer composites 1. a mechanical and microstructural study for different glass fabrics and resins," *Composites Science and Technology*, vol. 59, pp. 983–993, 1999.

[32] I. Verpoest and S. V. Lomov, "Virtual textile composites software wisetex: integration with micro-mechanical, permeability and structural analysis," *Composites Science and Technology*, vol. 65, pp. 2563–2574, 2005.

[33] M. M. Schwarz, *Composite materials handbook*. McGraw-Hill Inc, 1984.

[34] Gurit, "Company website - http://www.gurit.com." Internet, October 2009.

[35] F. Robitaille and R. Gauvin, "Compaction of textile reinforcements for composites manufacturing. iii: reorganisation of the fibre network," *Polymer Composites*, vol. 20, pp. 48–61, 1999.

[36] C. Lekakou and M. G. Bader, "Mathematical modelling of macro- and micro-infiltration in resin transfer moulding (rtm)," *Composites - Part A: Applied Science and Manufacturing*, vol. 29A, pp. 29–37, 1998.

[37] SP Systems, *ST 94 - Single Sprint material data sheet*. Gurit, Downloaded 22.08.2009.

[38] A. Tabiei and I. Ivanov, "Materially and geometrically non-linear woven composite micro-mechanical model with failure for finite element simulations," *International Journal of Non-Linear Mechanics*, vol. 39, pp. 175–188, 2004.

[39] A. M. Harte and N. A. Fleck, "On the mechanics of braided composites in tension," *European Journal of Mechanics - A/Solids*, vol. 19, pp. 259–275, 2000.

[40] P. Vandeurzen, J. Ivens, and I. Verpoest, "A three-dimensional micromechanical analysis of woven-fabric composites: Ii. elastic analysis," *Composites Science and Technology*, vol. 56, pp. 1317–1327, 1996.

[41] N. K. Naik and V. K. Ganesh, "Thermo-mechanical behaviour of plain weave fabric composites: experimental investigations," *Journal of Materials Science*, vol. 32, pp. 267–277, 1997.

[42] V. Tamuzs, K. Dzelzitis, and K. Reifsnider, "Prediction of the cyclic durability of woven composite laminates," *Composites Science and Technology*, vol. 68, pp. 2717–2721, 2008.

[43] S. Y. Lei and R. J. Young, "Deformation of pbo/epoxy plain weave fabric laminae followed using raman spectroscopy," *Composites: Part A*, vol. 32, pp. 499–509, 2001.

[44] A. Godara and D. Raabe, "Influence of fiber orientation on global mechanical behavior and mesoscale strain localisation in a short glass-fibre-reinforced epoxy polymer composite during tensile deformation investigated using digital image correlation," *Composites Science and Technology*, vol. 67, pp. 2417–2427, 2007.

[45] R. L. Karkkainen and B. V. Sankar, "A direct micromechanics method for analysis of failure initiation of plain weave textile composites," *Composites Science and Technology*, vol. 66, pp. 137–150, 2006.

[46] J. R. Lee, *Application of laser interferometric techniques to the experimental analysis of materials and structures - special case of composites.* PhD thesis, École Nationale Supérieure des Mines de Saint-Étienne and Université Jean Monnet, 2004.

[47] J.-R. Lee, J. Molimard, A. Vautrin, and Y. Surrel, "Digital phase-shifting grating shearography for experimental analysis of fabric composites under tension," *Composites - Part A: Applied Science and Manufacturing*, vol. 35, pp. 849–859, 2004.

[48] N. V. Carvalho, S. T. Pinho, and P. Robinson, "Compressive failure of 2d woven composites," in *Proceedings of the 17th International Conference on Composite Materials (on CD)*, 2009.

[49] L. V. Smith and S. R. Swanson, "Micro-mechanics parameters controlling the strength of braided composites," *Compoistes Science and Technology*, vol. 54, pp. 177–184, 1995.

[50] G. Washer and F. Blum Jr., "Raman spectroscopy for nondestructive testing of carbon fibre," *Research Letters in Materials Science*, vol. 2008, p. 3 pages, 2008.

[51] I. M. Robinson, M. Zakikhani, R. J. Day, R. J. Young, and C. Galiotis, "Strain dependence of the raman spectra for different types of carbon fibres," *Journal of Materials Science Letters*, vol. 6, pp. 1212–1214, 1987.

[52] W. Steinchen and L. Yang, *Digital shearography: theory and application of digital speckle pattern shearing interferometry*. SPIE Press, 2003.

[53] E. M. Weissmann and D. Post, "Moire interferometry near the theoretical limit," *Applied Optics*, vol. 21, pp. 1621–1623, 1982.

[54] R. D. Hale and D. O'Hare Adams, "Influence of in-plane fiber misalignment on moir interferometry results," *Journal of Composite Materials*, vol. 31, pp. 2444–2459, 1997.

[55] R. D. Hale, "An experimental investigation into strain distribution in 2d and 3d textile composites," *Composite Science and Technology*, vol. 63, pp. 2171–2185, 2003.

[56] G. Anzelotti, G. Nicoletto, and E. Riva, "Mesomechanic strain analysis of twill-weave composite lamina under unidirectional in-plane tension," *Composites: Part A*, vol. 39, pp. 1294–1301, 2008.

[57] A. Willems, S. V. Lomov, I. Verpoest, and D. Vandepitte, "Picture frame shear tests on woven textile composite reinforcements with controlled pretension," in *AIP Conference Proceedings: 10th ESAFORM Conference on Material Forming*, vol. 907, pp. 999–1004, 2007.

[58] D. A. Crump and J. M. Dulieu-Barton, "Full field strain analysis of aircraft sandwich structures," in *SEM XI International Congress on Experimental and Applied Mechanics*, 2008.

[59] G. Nicoletto, T. Marin, G. Anzelotti, and R. Roncella, "Application of high magnification digital image correlation technique to micromechanical strain analysis," *Strain*, vol. DOI: 10.1111/j.1475-1305.2008.00489.x, 2008.

[60] D. Lecompte, A. Smits, S. Bossuyt, H. Sol, J. Vantomme, D. Van Hemelrijck, and A. M. Habraken, "Quality assessment of speckle patterns for digital image correlation," *Optics and Lasers in Engineering*, vol. 44, pp. 1132–1145, 2006.

[61] M. Whelan, E. Hack, T. Siebert, R. Burguete, E. A. Patterson, and Q. Saleem, "On the calibration of optical full-field strain measurement systems," *Advances in Experimental Mechanics IV*, pp. 397–402, 2005.

[62] X. Tang and J. Whitcomb, "General techniques for exploiting periodicity and symmetries in micromechanics analysis of textile composites," *Journal of Composite Materials*, vol. 37, pp. 1167–1189, 2003.

[63] N. K. Naik and V. K. Ganesh, "An analytical method for plain weave fabric composites," *Composites*, vol. 26, pp. 281–289, 1995.

[64] R. M. Jones, *Mechanics of composite materials, 2nd ed.* Taylor & Francis, 1999.

[65] W. G. Jiang, S. R. Hallett, and M. R. Wisnom, *Development of domain superposition technique for the modelling of woven fabric composites, in: Computational Methods in Applied Sciences*. Springer, 2008.

[66] V. R. Aitharaju and R. C. Averill, "Three-dimensional properties of woven-fabric composites," *Composites Science and Technology*, vol. 59, pp. 1901–1911, 1999.

[67] L. G. Zhao, N. A. Warrior, and A. C. Long, "Finite element modelling of damage progression in non-crimp fabric reinforced composites," *Composites Science and Technology*, vol. 66, pp. 36–50, 2006.

[68] K. Woo and J. D. Whitcomob, "A post-processor approach for stress analysis of woven textile composites," *Composite Science and Technology*, vol. 60, pp. 693 – 704, 2000.

[69] K. B. Breiling and D. O. Adams, "Effects of layer nesting on compression-loaded 2-d woven textile composites," *Journal of Composite Materials*, vol. 30, pp. 1710 – 1728, 1996.

[70] S. V. Lomov and I. Verpoest, "Wisetex - virtual textile reinforcement software." downloaded from the internet on the 07/04/2008, http://www.mtm.kuleuven.ac.be/Research/C2/poly/index.htm, August 2004.

[71] J. J. Crookston, W. Ruijter, A. C. Long, and I. A. Jones, "Modelling mechanical performance including damage development for textile composites using grid-based finite element method with adaptive mesh refinement," in *8th International Conference on Textile Composites (TEXCOMP-8)*, 2006.

[72] S. V. Lomov, N. Huysmans, Y. Lou, R. S. Parnas, A. Prodromou, I. Verpoest, and F. R. Phelan, "Textile composites: modelling strategies," *Composites - Part A: Applied Science and Manufacturing*, vol. 32, pp. 1379 – 1394, 2001.

[73] E. L. Dereniak and G. D. Boreman, *Infrared Detectors and Systems*. John Wiley & Sons, Inc, 1996.

[74] M. A. Bramson, *Infrared Radiation: A handbook for applications.* Plenum Press, 1968.

[75] J. A. Jamieson, R. H. McFee, G. N. Plass, R. H. Grube, and R. G. Richards, *Infrared physics and engineering.* McGraw-Hill, 1963.

[76] R. D. Hudson and J. W. Hudson, *Infrared detectors.* Dowden, Hutchinson & Ross, Inc., 1975.

[77] A. Vaško, *Infrared Radiation.* Iliffe Books Ltd, 1968.

[78] G. Pitarresi, M. S. Found, and E. A. Patterson, "An investigation of the influence of macroscopic heterogeneity on the thermoelastic response of fibre reinforced plastics," *Composites Science and Technology*, vol. 65, pp. 269–280, 2005.

[79] P. Y. B. Jar, X. E. Gros, A. Masuki, T. Shinmura, and K. Takahashi, "Thermoelastic infrared stress analysis of rubber-toughened thermoplastics," *Journal of Materials Science Letters*, vol. 19, pp. 1143–1146, 2000.

[80] H. Inoue, Y. Hirokawa, and K. Kishimoto, "Stress separation in thermoelastic stress analysis using non-linearity and thermoelastic effect," *JSME International Journal*, vol. 47, pp. 305–311, 2004.

[81] I. Oda, A. Willett, M. Yamamoto, T. Matsumoto, and Y. Sosogi, "Non-contact evaluation of stresses and deformation behaviour in pre-cracked dissimilar welded joints," *Engineering Fracture Mechanics*, vol. 71, pp. 1453–1475, 2004.

[82] A. K. Wong and T. G. Ryall, "Performance of the fast system for stress analysis," *Experimental Mechanics*, vol. 35, pp. 148–152, 1995.

[83] T. G. Ryall and A. K. Wong, "Fast: A leading edge experimental stress analysis system," in *Proceedings of the first Australasian congress on applied mechanics: ACAM-96*, pp. 653–658, 1996.

[84] G. Pitarresi, L. D'Acquisto, F. L. Nigro, and A. M. Siddiolo, "Thermoelastic stress analysis by means of a standard thermocamera and a 2d-fft based lock-in technique," in *Experimental analysis of nano and engineering materials and structures, proceedings of the 13th international conference on experimental mechanics, Alexandroupolis, Greece, July 1-6, 2007* (E. E. Gdoutos, ed.), Springer, 2007.

[85] J. M. Dulieu-Smith, "Alternative calibration techniques for quantitative thermoelastic stress analysis," *Strain*, vol. 31, pp. 9–16, 1995.

[86] T. R. Emery, *Identification of damage in composite materials using thermoelastic stress analysis.* PhD thesis, University of Southampton, 2007.

[87] J. M. Dulieu-Barton, J. S. Earl, and R. A. Shenoi, "Determination of the stress distribution in foam-cored sandwich construchtion composite tee joints," *Journal of Strain Analysis*, vol. 36, no. 6, pp. 545–560, 2001.

[88] J. M. Dulieu-Smith, S. Quinn, R. A. Shenoi, P. J. C. L. Read, and S. S. J. Moy, "Thermoelastic stress analysis of a grp tee joint," *Applied Composite Materials*, vol. 4, pp. 283–303, 1997.

[89] P. R. Cunningham, J. M. Dulieu-Barton, and R. A. Shenoi, "Damage location and identification using infra-red thermography and thermoelastic stress analysis," *Proceedings of SPIE*, vol. 4704, pp. 93–103, 2002.

[90] E. A. Patterson, E. Hack, P. Brailly, R. L. Burguete, Q. Saleem, T. Siebert, R. A. Tomlinson, and M. P. Whelan, "Callibration and evaluation of optical systems for full-field strain measurement," *Optics and Lasers in Engineering*, vol. 45, pp. 550–564, 2006.

[91] R. Burguete, E. Hack, M. Kujawinska, E. Patterson, Q. Saleem, T. Siebert, and M. Whelan, "Standards project for optical techniques of strain measurement: Final report," in *SEM Annual Conference and Exposition on Experimental and Applied Mechanics 2006, Jun 4-7 2006*, 2006.

[92] P. Stanley and W. K. Chan, "Stress studies in composite cylinders based on measurements of infra-red emissions due to cyclic loading," in *International Symposium on Mechanics of Polymer Composites, Prague*, 1986.

[93] P. Stanley and W. K. Chan, "The application of thermoelastic stress analysis techniques to composite materials," *Journal of Strain Analysis*, vol. 23, pp. 137–143, 1988.

[94] R. T. Potter, "Stress analysis in laminated fibre composites by thermoelastic emission," *Proceedings of the SPIE*, vol. 731, pp. 110–120, 1987.

[95] J. M. Dulieu-Barton and P. Stanley, "Development and applications of thermoelastic stress analysis," *Journal of Strain Analysis*, vol. 33, pp. 93–104, 1998.

[96] T. R. Emery, J. M. Dulieu-Barton, J. S. Earl, and P. R. Cunningham, "A generalised approach to the calibration of orthotropic materials for thermoelastic stress analysis," *Composites Science and Technology*, vol. 68, pp. 743–752, 2008.

[97] T. S. Phan, J. M. Dulieu-Barton, and P. Temarel, "Thermoelastic stress analysis of structures under natural vibrations," *Experimental Mechanics*, vol. 46, pp. 463–472, 2006.

[98] A. K. Wong, "A non-adiabatic thermoelastic theory for composite laminates," *Journal of Physics and Chemistry of Solids*, vol. 52, pp. 483–494, 1991.

[99] C. E. Bakis and K. L. Reifsnider, "The adiabatic thermoelastic effect in laminated fibre composites," *Journal of Composite Materials*, vol. 25, pp. 809–830, 1991.

[100] S. Barone and E. A. Patterson, "Polymer coating as a strain witness in thermoelasticity," *Journal of Strain Analysis*, vol. 33, pp. 223–232, 1998.

[101] A. Sambasivam, S. Quinn, and J. M. Dulieu-Barton, "Identification of the source of the thermoelastic response from orthotropic laminated composites," in *Proceedings of the 17th International Conference on Composite Materials (on CD)*, 2009.

[102] D. Zhang, N. F. Enke, and B. I. Sandor, "Thermographic stress analysis of composite materials," *Experimental Mechanics*, vol. 30, pp. 68–73, 1990.

[103] R. El-Hajjar and T. Haj-Ali, "A quantitative thermoelastic stress analysis method for pultruded composites," *Composite Science and Technology*, vol. 63, pp. 967–978, 2003.

[104] S. W. Boyd, J. M. Dulieu-Barton, and L. Rumsey, "Stress analysis of finger joints in pultruded grp materials," *International Journal of Adhesion and Adhesives*, vol. 26, pp. 498–510, 2006.

[105] S. W. Boyd, J. M. Dulieu-Barton, O. T. Thomsen, and A. Gheradi, "Stress analysis of bonded joints in pultruded grp components," in *Sixteenth International Conference on Composite Materials (ICCM 16)*, Japanese Society for Composite Materials, 2007.

[106] T. J. Mackin and T. E. Purcell, "The use of thermoelasticity to evaluate stress redistribution and notch sensitivity in ceramic matrix composites," *Experimental Techniques*, vol. 20, pp. 15–20, 1996.

[107] T. J. Mackin and M. C. Roberts, "Evalutaion of damage evolution in ceramic-matrix composites using thermoelastic stress analysis," *Journal of the American Ceramics Society*, vol. 83, pp. 337–343, 2000.

[108] T. J. Mackin, T. L. Halverson, and N. R. Sottos, "The effect of interfacial properties on damage evolution in model composites," *Polymer Composites*, vol. 26, pp. 241–246, 2005.

[109] T. Zweschper, G. Riegert, A. Dillenz, and G. Busse, "Frequency-modulated elastic wave thermography," *Proceedings of SPIE*, vol. 5073, pp. 286–391, 2003.

[110] J. M. Dulieu-Barton, T. R. Emery, S. Quinn, and P. R. Cunningham, "A temperature correction methodology for quantitative thermoelastic stress analysis and damage assessment," *Measurement Science and Technology*, vol. 17, pp. 1627–1637, 2006.

[111] R. J. H. Paynter and A. G. Dutton, "The use of a second harmonic correlation to detect damage in composite structures using thermoelastic stress measurements," *Strain*, vol. 39, pp. 73–78, 2003.

[112] D. V. Hemelrijck, L. Shillemans, A. H. Cardon, and A. K. Wong, "The effects of motion on thermoelastic stress analysis," *Composite Structures*, vol. 18, pp. 221–238, 1991.

[113] R. L. Karkkainen, B. V. Sankar, and J. T. Tzeng, "Strength prediction of multilayer plain weave textile composites using the direct micromechanics method," *Composites - Part B: Engineering*, vol. 38, pp. 924 – 932, 2007.

[114] I. M. Daniel and O. Ishai, *Engineering Mechanics of Composite Materials*. Oxford University Press, 1994.

[115] Z. H. Karadeniz and D. Kumlutas, "A numerical study on the coefficients of thermal expansion of fiber reinforced composite materials," *Composite Structures*, vol. 78, pp. 1–10, 2007.

[116] SP Systems, *Prime 20LV Epoxy Infusion System Product Data Sheet*. Gurit, Downloaded on 20.11.2006.

[117] R. Crutchlow, "Personal communication," October 2007.

[118] Automation-Creations-Inc, "Online material datasheet - http://www.matweb-.com." Internet, October 2007.

[119] F. Lanza di Scalea, "Measurement of thermal expansion coefficients of composites using strain gages," *Experimental Mechanics*, vol. 38, pp. 233–241, 1998.

[120] J. M. Dulieu-Barton, M. C. Fulton, and P. Stanley, "The analysis of thermoelastic isopachic data from crack tip stress fields," *Fatigue and Fracture of Engineering Materials and Structures*, vol. 23, pp. 301–313, 2000.

[121] R. M. Mayer, *Design of composite structures against fatigue: Applications to wind turbine blades*. Mechanical Engineering Publications Ltd, 1996.

[122] R. C. Drew and R. G. White, "An investigation into damage propagation and its effect upon dynamic properties of cfrp composite materials," in *Proceedings of the Fourth International Conference on Composite Structures*, 1987.

[123] T. J. Barden, D. P. Almond, S. G. Pickering, M. Morbidini, and P. Cawley, "Detection of impact damage in cfrp composites by thermosonics," *Nondestructive Testing and Evaluation*, vol. 22, pp. 71–82, 2007.